

Hexagonal III-Phosphide alloys for solid state lighting

Citation for published version (APA):

Gagliano, L. (2017). *Hexagonal III-Phosphide alloys for solid state lighting*. [Phd Thesis 1 (Research TU/e / Graduation TU/e), Applied Physics and Science Education]. Technische Universiteit Eindhoven.

Document status and date:

Published: 27/11/2017

Document Version:

Publisher's PDF, also known as Version of Record (includes final page, issue and volume numbers)

Please check the document version of this publication:

- A submitted manuscript is the version of the article upon submission and before peer-review. There can be important differences between the submitted version and the official published version of record. People interested in the research are advised to contact the author for the final version of the publication, or visit the DOI to the publisher's website.
- The final author version and the galley proof are versions of the publication after peer review.
- The final published version features the final layout of the paper including the volume, issue and page numbers.

[Link to publication](#)

General rights

Copyright and moral rights for the publications made accessible in the public portal are retained by the authors and/or other copyright owners and it is a condition of accessing publications that users recognise and abide by the legal requirements associated with these rights.

- Users may download and print one copy of any publication from the public portal for the purpose of private study or research.
- You may not further distribute the material or use it for any profit-making activity or commercial gain
- You may freely distribute the URL identifying the publication in the public portal.

If the publication is distributed under the terms of Article 25fa of the Dutch Copyright Act, indicated by the "Taverne" license above, please follow below link for the End User Agreement:

www.tue.nl/taverne

Take down policy

If you believe that this document breaches copyright please contact us at:

openaccess@tue.nl

providing details and we will investigate your claim.

Hexagonal III-Phosphide Alloys for Solid State Lighting

PROEFSCHRIFT

ter verkrijging van de graad van doctor aan de Technische Universiteit
Eindhoven, op gezag van de rector magnificus prof.dr.ir. F.P.T. Baaijens, voor
een commissie aangewezen door het College voor Promoties, in het openbaar te
verdedigen op maandag 27 november 2017 om 16:00 uur

door

Luca Gagliano

geboren te Milano, Italië

Dit proefschrift is goedgekeurd door de promotoren en de samenstelling van de promotiecommissie is als volgt:

voorzitter: prof.dr.ir. G.M.W. Kroesen
1e promotor: prof.dr. E.P.A.M. Bakkers
copromotor: dr. J.E.M. Haverkort
leden: prof.dr. L. Miglio (Università Milano-Bicocca)
prof.dr. M.A. Loi (Universiteit Groningen)
prof.dr. A. Meijerink (Universiteit Utrecht)
prof.dr.ir. W.M.M. Kessels
dr. M. Creatore

Het onderzoek of ontwerp dat in dit proefschrift wordt beschreven is uitgevoerd in overeenstemming met de TU/e Gedragscode Wetenschapsbeoefening.

A catalogue record is available from the Eindhoven University of Technology Library.

ISBN: 978-90-386-4374-8

The work described in this dissertation has been performed in the Photonics and Semiconductor Nanophysics (PSN) group, Applied Physics department at Eindhoven University of Technology, The Netherlands.

Contents

1	Introduction	9
1.1	Semiconductors: limits and new solutions	9
1.2	Nanowires	10
1.3	Applications of nanowires	12
1.3.1	Light emitting diodes	12
1.3.2	Photovoltaics	16
1.3.3	Solar hydrogen production	18
1.4	Nanowire growth - MOVPE	20
1.4.1	VLS epitaxy	20
1.4.2	VS/catalyst-free epitaxy	20
1.5	Scope of this thesis	22
2	Theoretical concepts: from wurtzite growth to band structure	25
2.1	Formation of wurtzite in nanowires	25
2.2	Band structure of wurtzite III-Phosphides	29
2.2.1	Density functional theory calculations	29
2.2.2	Selection rules	30
2.2.3	GaP	32
2.2.4	InP	33
2.2.5	AlP	33
2.2.6	Alloy band structure	36
3	Experimental methods, techniques and fabrication	37
3.1	Substrate preparation	37
3.1.1	Nanoimprint lithography	37
3.1.2	Electron beam lithography	39
3.1.3	Silicon nitride mask	39
3.1.4	Pre-deposition cleaning	40
3.2	MOVPE	40
3.2.1	Showerhead reactor	41

3.2.2	Horizontal flow reactor	41
3.2.3	Cleaning and memory effect	42
3.3	Scanning electron microscopy (SEM)	42
3.4	Transmission electron microscopy (TEM)	43
3.4.1	TEM modes	43
3.4.2	Cross-sectional analysis	45
3.4.3	Nanomanipulation	46
3.5	Photoluminescence	47
3.5.1	Experimental setup	50
3.5.2	Photoluminescence excitation spectroscopy	50
4	Pseudo-direct to direct compositional crossover in wurtzite GaP/InGaP core-shell nanowires	53
4.1	Core-shell nanowire growth	54
4.1.1	Wurtzite GaP core growth	54
4.1.2	Catalyst Etching	55
4.1.3	Wurtzite InGaP Shell Growth	56
4.2	TEM analysis and strain simulations	59
4.3	Low temperature photoluminescence	63
4.3.1	Steady-state PL	63
4.3.2	Time-resolved photoluminescence	65
4.3.3	Temperature dependent photoluminescence	68
4.4	WZ InGaP band structure	70
4.5	Conclusions	73
5	Infrared to green emitting pure wurtzite AlInP nanowires	75
5.1	AlInP nanowires growth	75
5.2	Optical Properties	85
5.2.1	Power dependence of the photoluminescence	87
5.2.2	Time-resolved photoluminescence	91
5.2.3	Temperature-dependent photoluminescence	92
5.3	Band structure of WZ AlInP	97
5.4	Conclusions	99
6	Understanding the origin of bending in wurtzite GaP/InGaP core-shell nanowires	103
6.1	Single nanowire case study	104
6.2	Systematic study of the shell asymmetry	111
6.3	Conclusions	112

7	Growth of atomically sharp homointerfaces in GaP nanowires	115
7.1	Growth of WZ/ZB homostructures	116
7.2	Zincblende growth control	117
7.3	Wurtzite growth control	120
7.4	Nucleation model of ZB and WZ	122
7.5	Conclusions	122
8	Wurtzite GaP nanowires for thermal transport study	125
8.1	Thin wurtzite GaP nanowires	126
8.1.1	Quasi-ballistic phonon transport	127
8.2	Telescopic GaP nanowires	132
8.3	Conclusions	135
9	Wurtzite III-phosphide nanowires for solid state lighting	139
9.1	Market Analysis	140
9.2	Our proposed invention	143
9.3	Business Model	144
9.3.1	Value proposition	145
9.3.2	Key partnerships	146
9.3.3	Customer segments	146
9.3.4	Key activities and resources	147
9.3.5	Cost structure	147
9.3.6	Channels and revenue streams	147
9.4	Activity roadmap	148
9.4.1	Scientific developments	148
9.4.2	Technological nodes	149
9.4.3	Substrate development	149
9.4.4	Electrical top contact	150
9.4.5	Estimated time of development	150
9.5	Conclusions	151
	Bibliography	153
	Summary	166
	Curriculum Vitae	168
	List of Publications	170

Chapter 1

Introduction

1.1 Semiconductors: limits and new solutions

Semiconductors are a material class with numerous technological applications such as electronics, solid state lighting (SSL) and solar energy harvesting. Their electronic band structure features an energy band gap, spanning a large interval of energies from less than 0.2eV up to 4eV. Techniques such as alloying, doping and heterostructuring allow to tune their properties, making semiconductors an extremely valuable tool for solving practical challenges. One of the most relevant fields in semiconductor technology is electronics, where the commonly used parameter to describe its advancement is the number of transistors per surface area. The famous empirical observation formulated in 1965 by Gordon Moore states that the number of transistors in a chip doubles every two years. However, as the size of transistors approaches the nanometer, the granular nature of matter becomes an important factor, limiting the minimum size of such devices. The counterpart of Moore's law for solid state lighting is Haitz's law, which states that every decade the cost per lumen of light emitting diodes (LEDs) (1 candela · 1 steradian) falls by a factor of 10, and the amount of light generated per LED package increases by a factor of 20, for a given wavelength. Also light emitting diodes however suffer from intrinsic restrictions which limit their efficiency, particularly in the green-amber region, a phenomenon called "green gap", illustrated in Fig.1.1.

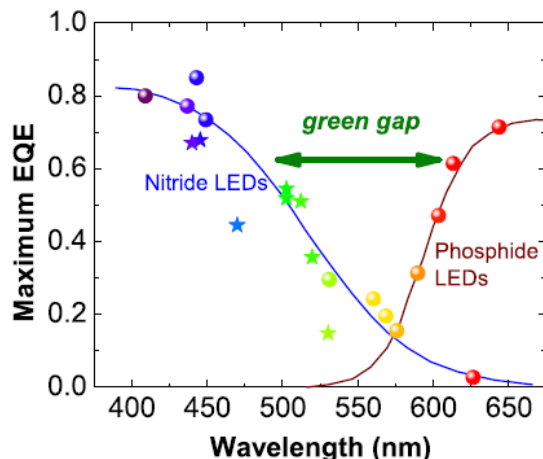


Figure 1.1: Maximum external quantum efficiency (EQE) of various commercial Nitride and Phosphide LEDs, illustrating the "green gap" concept. The efficiency of Nitride LEDs, based on InGaN alloys, decreases in the green range due to Auger effects, lower miscibility between GaN and InN and increased strain between GaN and the InGaN quantum wells. The efficiency of Phosphide LEDs decreases due to the direct to indirect transition of AlGaInP alloys. Adapted from Ref. ¹.

Semiconductor research is therefore now focusing on finding new solutions and even new physical principles on which to build future generations of devices, progressively moving to nanostructuring in order to exploit the effects arising at nanoscale size.

One of the focal points of fundamental as well as applied research is to render available new degrees of freedom, in order to enhance and tailor the material properties for specific applications. Size, photonic effects, surface to volume ratio, crystal symmetry and relative electronic properties are among these degrees of freedom. A type of nanostructure that has recently emerged as a promising tool to control these and other properties are nanowires.

1.2 Nanowires

Nanowires are high aspect ratio nanostructures which can exhibit unique effects ranging from strain relaxation to quantum confinement phenomena. One important property is the possibility to tune the crystal structure of a semiconductor nanowire by controlling the parameters during epitaxial growth, up to the point where the crystal phase can be changed during the epitaxy^{2;3}, as illustrated in

Fig.1.2. This process is normally impossible in planar technology, while it is allowed in nanowires due to their unique geometry: when the surface to volume ratio is high enough, the surface properties of a crystal dominate the volume properties, thus favoring new crystal symmetries⁴. For instance, Gallium Phosphide (GaP) is found as Zincblende (ZB) in bulk, but can be grown as Wurtzite (WZ) in nanowires. This allows to explore the properties of new semiconductors and test them for possible technological applications: GaP exhibits an indirect band gap in Zincblende structure and a direct one in Wurtzite, being therefore more suitable for optical applications^{5;6}. These concepts will be discussed in detail in Chapter 2.

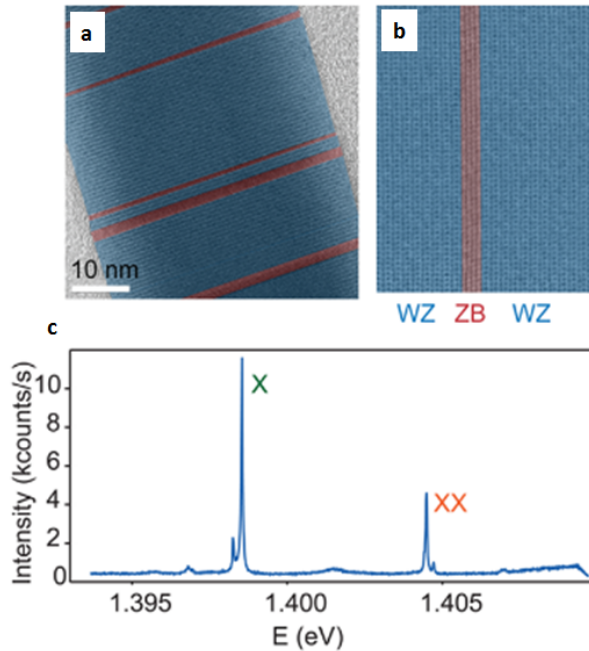


Figure 1.2: (a) Transmission electron microscopy of InP nanowires showing short segments of zinc blende (red) in a wurtzite (blue) nanowire. (b) High resolution-transmission electron microscopy image of a single zinc blende segment in the wurtzite lattice. (c) Microphotoluminescence spectra of a crystal phase quantum dot: due to the different electronic band structure of the two crystal symmetries, carriers are trapped at the ZB/WZ interface and recombine with characteristic energies. Adapted from Ref.².

The high surface to volume ratio is also a very attractive property for surface chemistry: catalytic reactions that happens at the surface of a semiconductor,

such as water reduction into hydrogen, will be enhanced by the larger reactive surface offered, leading to higher overall efficiency⁷. Nanowires also allow for effective three-dimensional strain relaxation, causing a wide range of heterostructures to be grown with higher crystal quality than planar structures, with a low incidence of defects such as misfit dislocations. These defects are almost always detrimental as they tend to be non-radiative recombination centers, thus degrading the optical properties of the semiconductor⁸. Due to their geometry, nanowires interact with electromagnetic radiation in a non-trivial way, leading to peculiar photonic effects. One of the most important phenomena is the "antenna effect", which allows nanowires to absorb more light than their volume suggests, with clear applications where strong absorption is needed, such as photovoltaics^{9;10}. Nanowires can also have a strong light outcoupling, meaning the adiabatic conversion of the photonic mode into vacuum, therefore avoiding internal reflection. This phenomenon, together with strong waveguiding effects along the nanowire axis, provides with a new degree of freedom in the management of light emission and directionality¹¹.

1.3 Applications of nanowires

Thanks to their unique properties, nanowires are promising for several fields of application. For the materials developed in this work, three fields are of major interest: solid state lighting, photovoltaics and solar water reduction into hydrogen.

1.3.1 Light emitting diodes

Light emitting diodes (LEDs) are nowadays capable of providing performance that surpasses older conventional solutions both in efficiency and in color rendering index (CRI)¹². Outdoor and indoor lighting, automotive and monitor backlighting systems often adopt LEDs because of their superior properties. However, LEDs are far from being perfect and still face high production costs and low efficiency in the green-amber region^{12;13;14}. The current approach to obtain reasonably efficient LEDs in the green/amber region is to rely on phosphor conversion of blue light. However, this introduces some inefficiency and a broadened emission, while a sharp monochromatic emission is highly desirable, especially for display applications. The ideal solution would be to use direct green LEDs, where the emitting material possesses a band gap of about 2.35eV. Unfortunately a suitable material is still not available, as InGaN alloys face Indium segregation issues¹³, while AlInGaP alloys suffer from a direct to indirect crossover with Al concentration over 50%¹⁵. New solutions and new materials are therefore needed in order to produce such LEDs and "bridge the green gap". Such innovation

would also affect the efficiency and cost-effectiveness of white LED lamps with high CRI, allowing better and more advanced color mixing at lower cost¹⁶.

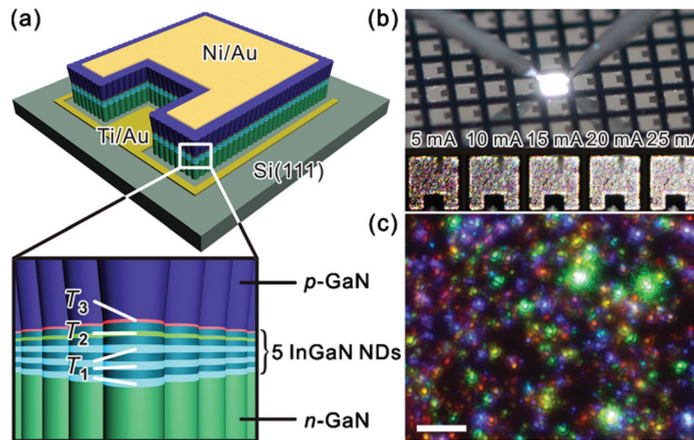


Figure 1.3: (a) Schematic of a GaN/InGaN nanowire LED grown on silicon (111). A Ti/Au pad constituted the bottom contact, while a Ni/Au pad forms the top contact. The nanodisks are formed along the axis of the nanowire. As these nanodisks can have different composition and therefore different bandgap, the overall spectrum of the LED can be in principle be tuned, leading to white emission instead of monochromatic. (b) Photographs of the GaN/InGaN nanowire LED emitting white light. (c) Micro-photograph of the nanowire array emitting during the electroluminescence experiment¹⁷. Different nanowires (single dots in the image) emit with a different wavelength. The effect is due to different incorporation of different nanowires, due to differences (e.g. radius) between nanowires.

GaN-based nanorods and nanowires are considered the current state-of-the-art in NanoLEDs, as they offer several advantages over planar structures^{18;19;20}. An example of GaN NanoLED is shown in Fig.1.3. The nanowire geometry allows to grow higher quality crystals with a lower dislocation density than in planar structures, as these defects bend towards the side surfaces and there they disappear, by forming, for example, a surface step²¹. The entire active area is also more protected from episodes of thermal stress due to the different thermal expansion with the substrate, like sapphire or silicon. Nanorods can also guarantee a higher light extraction efficiency respect to planar systems, enhancing the external quantum efficiency of the NanoLED. Finally, core-shell nanowires where quantum wells are grown on the whole cylindrical surface offer a wider junction area than planar LEDs. Typical operating currents are relatively high, causing LEDs to be inefficient (a phenomenon called "droop"): a reduction of the current density by extending the active area would mitigate this problem²², as

shown in Fig.1.4, where the efficiency advantage in using nanowords is calculated and found to be in the order of 10-20% in terms of external quantum efficiency.

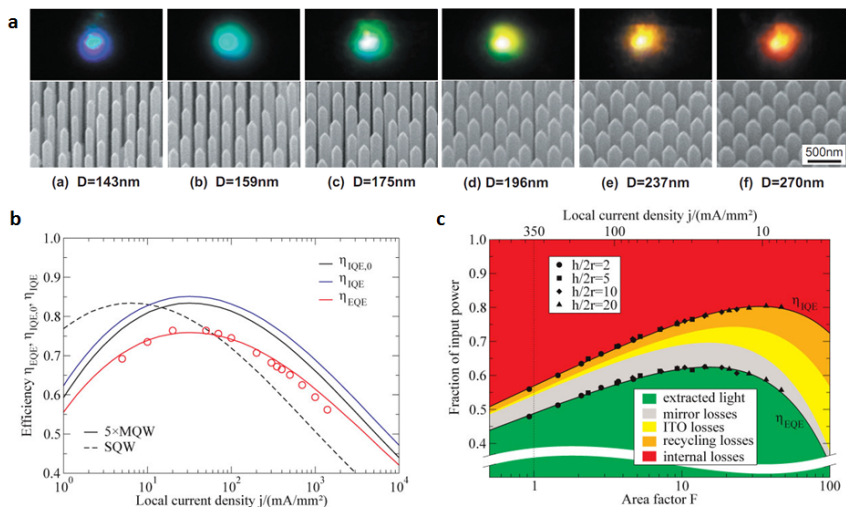


Figure 1.4: (a) SEM images of InGaN/GaN core-multishell nanowires with different diameters and micro-photographs of their photoluminescence. Adapted from Ref.²³. (b) External and internal quantum efficiency of single and multi quantum well LEDs as a function of current density. (c) Analysis of the losses in a core-shell nanowire LED as a function of the area factor F (ratio between nanoLED/planar LED junction area for device). Data points mark simulation results and are fitted with lines. Shaded areas represent the relative fractions of extracted light (green), internal losses (red) and the optical loss channels (grey, yellow, orange). Adapted from Ref.²².

Nanowires have the potential to boost the research on the "green gap" also by providing an additional degree of freedom on the control of the active material's electronic properties by controlling the crystal symmetry. For instance, Zincblende InGaN is considered a possible method of obtaining highly efficient green LEDs, as it possesses a lower band gap than Wurtzite InGaN, allowing therefore a device to emit at longer wavelength than normally possible because of the insurgence of the detrimental effects of the miscibility limit and lattice mismatch between GaN and InN^{24;25}. Innovative crystal symmetries can also be adopted in III-Phosphides, as it has been demonstrated that while GaP is an indirect semiconductor in Zincblende symmetry, it becomes a direct semiconductor in Wurtzite symmetry⁵. The low-temperature photoluminescence emission from WZ GaP and the alloys WZ AlGaP and WZ GaAsP is shown in Fig.1.5.

As we will see in Chapter 2, the resulting complex selection rules for the optical transitions make alloying necessary to obtain efficient light emission²⁶.

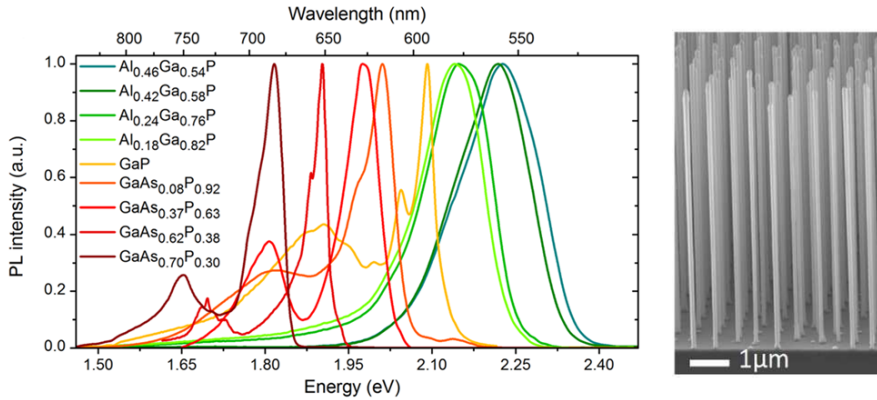


Figure 1.5: Left: Low-temperature (10K) photoluminescence spectra of WZ GaP and the ternary alloys WZ $\text{AlGa}_x\text{P}_{1-x}$ and WZ $\text{GaAs}_y\text{P}_{1-y}$, showing emission tunability. As we will see in Chapter 2, these alloys have a pseudo-direct bandgap, therefore alloying with Indium is necessary to obtain an efficient light-emitting material at room temperature. Right: SEM image of a WZ GaP nanowire array grown with Au-assisted vapour-liquid-solid growth⁵.

Due to their high aspect ratio, nanowires are also ideal candidates for lasing. Stimulated emission has been demonstrated in many regions of the light spectrum, for instance in materials such as ZnO²⁷, GaN/InGaN^{18;28}, InP²⁹, GaAs³⁰. Clearly, lasing indicates excellent optical quality, a prerequisite for the development of future nanoLEDs and nanolasers. In Fig.1.6 we report an example of WZ InP nanowires, lasing around 885nm (1.4eV).

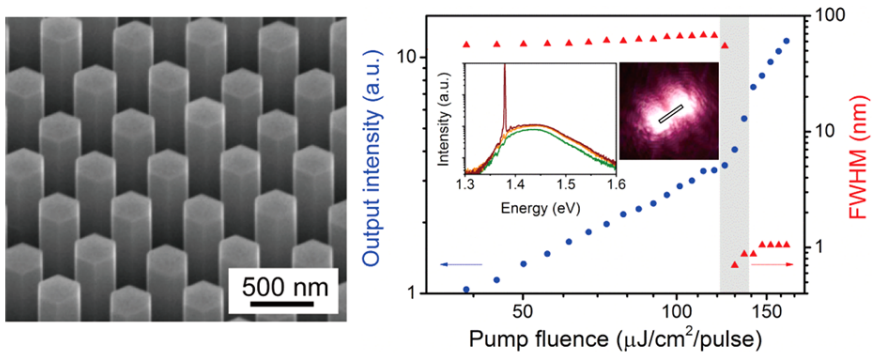


Figure 1.6: Left: SEM image of selective area, catalyst-free grown WZ InP nanowires. Right: photoluminescence intensity and full width at half maximum (FWHM) of a single WZ InP nanowire. Inset left: photoluminescence spectrum, showing the lasing mode. Inset right: false color image of a lasing WZ InP single nanowire, transferred on a SiOx surface²⁹. The removal from the native substrate enhances the refractive index contrast at the ends of the nanowire, increasing the internal reflection of light and lowering the lasing threshold.

1.3.2 Photovoltaics

Solar energy is considered one of the main future energy sources because of its abundance and environmental sustainability, constituting about 89,000 TW of power reaching our planet, compared to the global electricity consumption of "only" 15 TW. Solar cells have reached a very promising efficiency to cost ratio and are now finally considered as a realistic renewable source with which to satisfy the evergrowing energy demand^{31;32;33}. The current record for a single junction solar cell, namely a junction made of a single material, is 26.6% in Silicon and 28.8% in GaAs. The current record for a nanowire solar cell is 17.8%, using a top-down etched InP nanowire array³⁴, as shown in Fig.1.7. Multi-junction solar cells have led to a record of 46.0% under concentrated illumination³⁵. In this last type of cell, materials with different band gaps are used to cover the entire solar spectrum, leading to absorption of photons within a material with optimal band gap, reducing losses due to thermal relaxation. This approach maximizes the efficiency beyond the limits of a single material. In this type of devices, InGaP (1.86 eV), GaAs (1.4 eV), SiGe (1.12-0.65 eV) and others with comparable band gaps are used³⁶. Nanowires are ideal candidates for solar cells, as the antenna effect enables a nanowire array to absorb a much larger amount of light than a planar substrate^{37;33}. Nanowires also show an advantage on their planar counterparts due to a more efficient light coupling^{38;34}. Nanowires, by offering an increased strain relaxation, are also ideal candidates to integrate

lattice mismatched materials more easily and with less defectivity than in planar technology, potentially leading to higher quality multi-junction solar cells with even higher efficiencies.

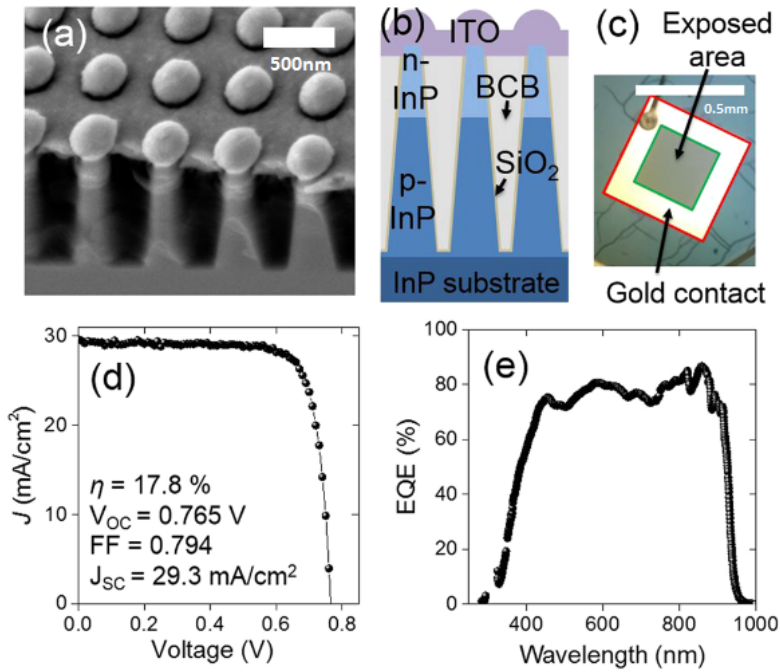


Figure 1.7: (a) SEM image of a cleaved nanowire solar cell device. (b) Schematic image of the InP solar cell, composed of an InP substrate with a Ti/Au back contact, p-n doped InP nanowires, obtained through reactive ion etching (RIE), mechanical planarization layer (BCB, polymer) and ITO front contact. (c) Microscope image of the solar cell device. The red square is the edge of the full solar cell, and the green square is the edge of the area that is exposed to light. (d) J-V curve of the best nanowire solar cell device, measured at 1 sun (AM1.5G) illumination. (e) External quantum efficiency (EQE) measurement of one of the cells obtained by measuring the efficiency of the solar cell while scanning wavelengths from a calibrated white light source. Adapted from Ref. ³⁴.

1.3.3 Solar hydrogen production

Energy vectors, meaning the form in which energy is distributed, are a vital research field, as 80% of the world energy consumption happens in the form of fuels. Solar fuels are a particularly promising system of storing renewable energy, which is otherwise very difficult to employ. Hydrogen is a suitable candidate as future renewable energy vector^{39:40}. Nowadays it is obtained from fossil fuels, a polluting practice which is not sustainable in the long term. A renewable production method is solar water splitting, for example using a semiconductor electrode to absorb light and use its energy to split water into hydrogen and oxygen, thus storing energy into chemical bonds.

The water splitting reaction happens at the surface of the electrode, therefore efficiency can be maximized by enhancing absorption and by extending the reactive surface. Nanowires, with their strong absorption and their high surface to volume ratio, are ideal candidates for this process⁷. The semiconductor chosen for a single junction photoelectrochemical (PEC) cell needs to have a band gap low enough to absorb a relevant part of the solar spectrum, but also high enough to produce a sufficient open circuit potential to let the reaction happen. A material having band gap in the ideal range 1.7-2.1eV can perform spontaneously hydrogen reduction when exposed to sunlight. A material that has been used in nanowire form for hydrogen conversion is WZ GaP⁷, as shown in Fig.1.8. Two semiconductor nanowire systems with an ideal bandgap have been obtained in the present work: wurtzite InGaP and wurtzite AlInP.

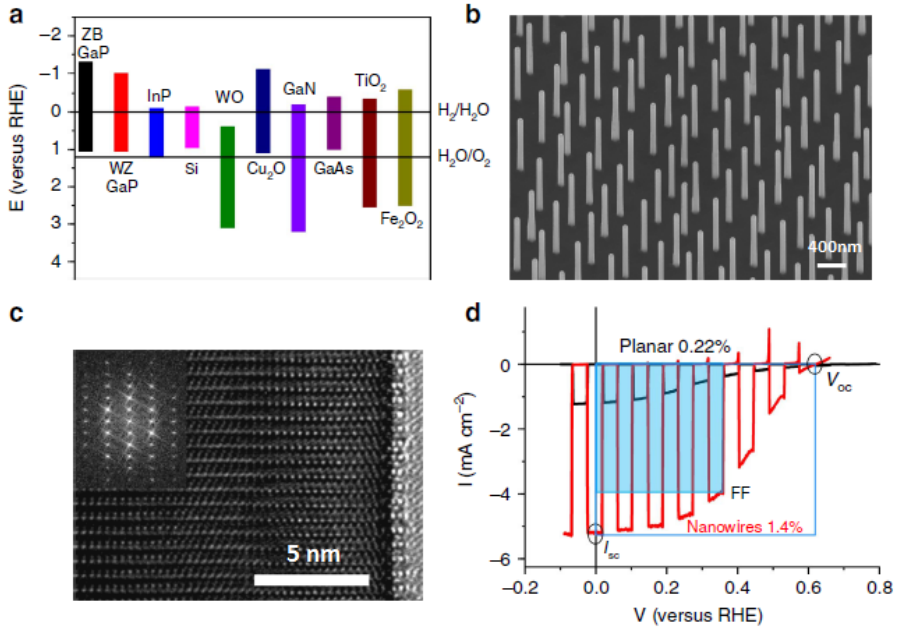


Figure 1.8: (a) Band gap and alignment of several semiconductors with respect to the reduction and oxidation potentials of water (b) SEM image of a typical array of GaP nanowires defined by nano imprint lithography. (c) High-resolution TEM image of a typical p-type GaP nanowire with WZ crystal structure. Inset: Fast Fourier Transform of the same area. (d) Linear sweep voltammograms for direct comparison of nanowire (red) and planar (black) samples with molybdenum sulphide catalyst. Also showing open circuit potential (VOC), short circuit current (ISC) and fill factor FF (filled square/empty square)⁷.

1.4 Nanowire growth - MOVPE

Different reactor systems can be used to grow nanowires. In this thesis, all nanowires were grown with Metalorganic Vapor Phase Epitaxy (MOVPE). The nanowires were grown with Au-catalyzed Vapor-Liquid-Solid (VLS) mechanism or Selective Area Epitaxy (SAE), while shells were grown using Vapor-Solid (VS) mechanism.

1.4.1 VLS epitaxy

In VLS technique the growth happens at the interface between solid, liquid and vapor phase^{41;42}. A catalyst is required, which can be a foreign metal (e.g. gold) or one of the elements of the growth itself (e.g. gallium-catalyzed growth of GaAs), in which case the growth is defined as "self-catalyzed". In this thesis, the catalysts used were Au droplets fabricated on a substrate using nanoimprint or electron beam lithography (EBL). In order to initiate the growth, the substrate is heated, allowing the Au droplet to enter the liquid state. Then the group III precursor, in this case Gallium, is introduced in the chamber, allowing the formation of a Au-Ga alloy. The growth starts when also the group V precursor, in this case Phosphine, is provided: GaP segregates at the bottom of the Au droplet, initiating a deposition which pushes upwards the droplet itself. The details of the growth will be treated in Chapter 2. With this mechanism, nanowires of arbitrary diameter and length can be grown, provided that the droplet and the growth are stable during the entire process. In Fig.1.9 we show a particular phenomenon which happens during VLS epitaxy: synergetic growth. The growth rate of a nanowire is not only influenced by the global growth conditions (e.g. temperature, precursor flows), but also by the surrounding nanowires and in particular by their catalysts. If the distance is short enough, the growth can therefore be synergetic, enhancing the growth rate, or competitive, slowing down the growth due to competition between nanowires for precursors⁴³.

1.4.2 VS/catalyst-free epitaxy

In VS growth the material is grown directly from the vapor phase without the assistance of a catalyst⁴⁴. This mechanism is used to grow nanowires through a Silicon Oxide or Silicon Nitride patterned mask as in the previously shown Fig.1.6. The main strength of this approach is the absence of a metallic catalyst in the process which might diffuse into the nanowire and constitute a deep non-radiative recombination center, degrading the optical properties. The catalyst can also be an issue during further processing, like shell growth or device fabrication. Au contaminations, for example can form deep centers in devices such as transistors and lasers, greatly affecting their performance. Additionally, this mechanism is

also used to grow shells around pre-existing nanowires as in Fig.1.10, in order to grow materials which might be particularly challenging to obtain otherwise.

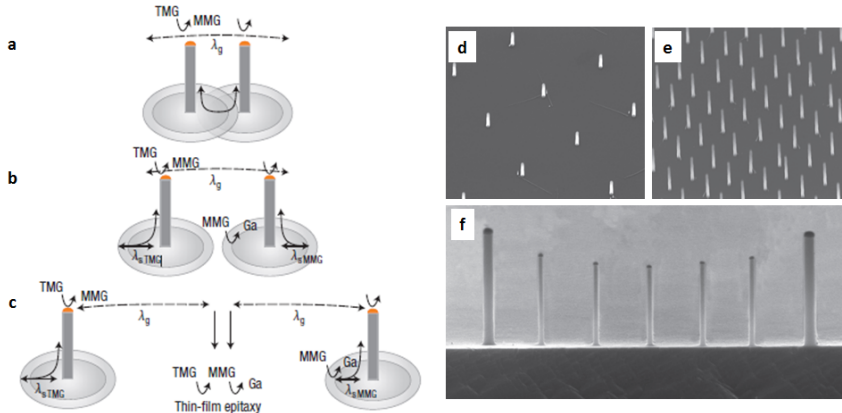


Figure 1.9: (a-c) Nanowire growth regimes: Trimethylgallium (TMG) is catalytically decomposed to Monomethylgallium (MMG) at a Au particle. Part of the MMG is desorbed and diffuses through the gas phase, eventually reaching a nanowire or depositing on the substrate, as a function of the distance between nanowires. (a) Competitive regime. (b) Synergetic regime (c) Independent regime. (d-e) Nanowire growth rate increase is observed by decreasing wire spacing L from 1,000 nm (d) to 400 nm (e) for a constant nanowire diameter d of 25 nm. (f) Nanowires grown from 25- and 100-nm catalysts with 300 nm spacing. Wires next to a thick wire are taller than the ones further, showing that the growth rate of one wire is dependent on the catalyst amount nearby (Au). Adapted from Ref. ⁴³.

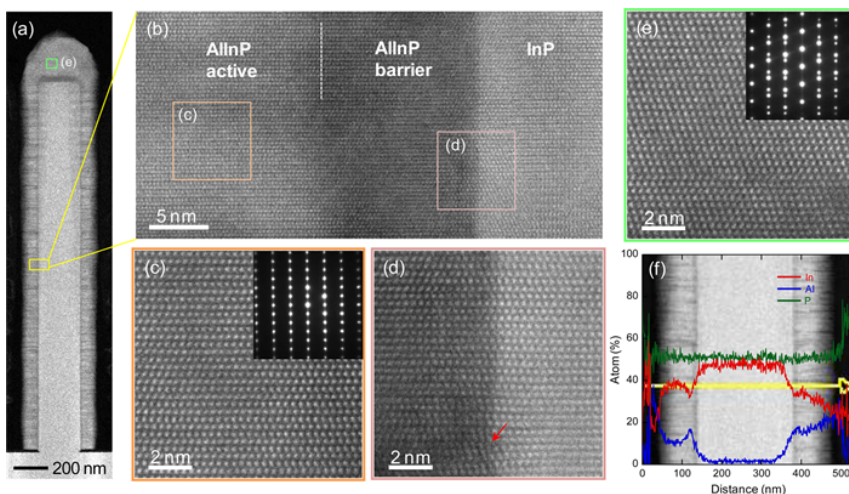


Figure 1.10: Cross-sectional TEM images of a wurtzite InP/AlInP core-multishell nanowire for $X_{TMAl} = 0.30$ in the $\langle -110 \rangle$ zone axis, showing misfit dislocations. The nanowire core was grown by selective area epitaxy. (b) High-resolution TEM image of the InP/AlInP core-shell nanowire. (c-d) Enlarged HR-STEM images of the orange and pink rectangles in panel b: (c) AlInP active layer, (d) Interface between AlInP and InP. (e) High-resolution TEM image of the AlInP shell on top of the InP nanowire. Insets in (c) and (e) show the selective area electron diffraction (SAED) patterns of each area. (f) Energy dispersive X-ray spectroscopy (EDS) line scan along the lateral direction with a HAADF-STEM image, showing the Al-rich AlInP barrier layers around the WZ InP core. Adapted from Ref.⁴⁴.

1.5 Scope of this thesis

In this thesis new hexagonal III-phosphide materials for efficient light emission are developed and their structural and optical properties studied in detail to provide fundamental understanding of their band structure. This thesis is composed of nine chapters, including this introductory one.

In Chapter 2 we discuss the formation of wurtzite in III-V nanowires, finding that supersaturation, surface energies and diameter of the nanowire play a key role. We also discuss the band structure of GaP, InP and AlP in both the cubic and hexagonal crystal structures, explaining the fundamental differences and the selection rules for their optical transitions.

In Chapter 3 we illustrate the methods used in this work, starting from the substrate preparation and catalyst array fabrication with nanoimprint and electron beam lithography. We introduce the nanowire growth technique, Metalorganic

Vapor Phase Epitaxy (MOVPE), followed by the structural and optical characterization techniques, such as TEM and micro-photoluminescence.

In Chapter 4 we develop the epitaxial growth of WZ $\text{In}_x\text{Ga}_{1-x}\text{P}$ by growing WZ GaP/ $\text{In}_x\text{Ga}_{1-x}\text{P}$ core-shell nanowires. We study for the first time its optical properties, finding strong evidence of a pseudo-direct ($\Gamma_8 - \Gamma_9$) to direct ($\Gamma_7 - \Gamma_9$) conduction band crossover as a function of composition, around $0.28 \leq x \leq 0.41$. We therefore determine that WZ $\text{In}_x\text{Ga}_{1-x}\text{P}$ can be used as an efficient light emitter up to 2.0eV, in the red emission range.

In Chapter 5 we develop the selective area epitaxy of WZ $\text{Al}_x\text{In}_{1-x}\text{P}$ and study its structural and optical properties, achieving direct green emission, a relevant result for solid state lighting applications. We also provide fundamental understanding of the band structure, finding that atomic ordering of Aluminum and Indium plays a key role in determining the selection rules of the band gap transition.

In Chapter 6 we study the asymmetry-induced bending of WZ GaP/ $\text{In}_x\text{Ga}_{1-x}\text{P}$, caused by thickness and composition asymmetry in the shell. We develop a diagnostic tool for evaluating the degree of asymmetry in the shell, using experimental data and finite elements method simulations.

In Chapter 7 we demonstrate a technique to control the crystal phase of GaP nanowires grown with VLS method. We show that by tuning the growth temperature and V/III ratio we can grow atomically sharp crystal phase homostructures, with a control almost at the monolayer level.

In Chapter 8 we develop the growth of thin WZ GaP nanowires with diameter down to 25nm, which show quasi-ballistic phonon transport properties at room temperature. We also develop the growth of telescopic nanowires, which are predicted to show heat rectifying behavior.

Finally, in Chapter 9 we illustrate a business plan, formulated using the results of this thesis on WZ $\text{Al}_x\text{In}_{1-x}\text{P}$, which can be realistically adopted as emitting material in future nanostructured light emitting diodes, offering advantages in terms of efficiency and cost reduction, compared to current products.

Chapter 2

Theoretical concepts: from wurtzite growth to band structure

In this chapter we illustrate the origin of the wurtzite crystal symmetry in nanowires from a theoretical point of view. The current understanding is based on catalyst-assisted VLS growth. We then discuss the band structure of Wurtzite III-Phosphide alloys and their optical selection rules.

2.1 Formation of wurtzite in nanowires

III-phosphide and III-arsenide materials are always found with zincblende structure in bulk. In fact, the difference in cohesive energy between zincblende and wurtzite is 24meV per III-V pair, making zincblende more stable. In nanowires however, a surprisingly strong tendency to form wurtzite has been noticed right from the early stages of their development⁴. WZ can be obtained both with VLS and catalyst-free growth, but at the current stage the understanding is complete only in the case of VLS growth. In VLS growth, wurtzite is observed when certain conditions are met, which can be derived analytically, starting from an experimental observation in WZ GaAs nanowires grown on a (111)B ZB GaAs substrate, as shown in Fig.2.1a. When the WZ nanowire growth is started, a ZB pedestal is first formed, and only after some time the crystal structure abruptly switches to WZ. Also, when the growth is terminated by closing only the Ga flow while still providing AsH₃, a ZB segment is formed. In this case, the growth is due to depletion of Ga in the catalyst alloy droplet, which reacts with the AsH₃

still present. This phenomenon happens systematically for every growth, leading us to the conclusion that WZ forms when a certain high enough supersaturation condition is met in the catalyst.

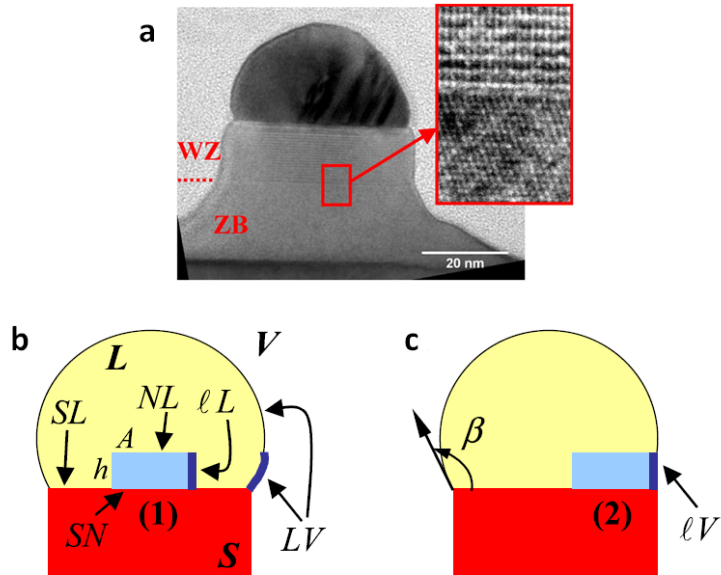


Figure 2.1: (a) Transmission electron microscopy image of a short GaAs nanowire with high resolution close-up of the transition zone between zinc blende and wurtzite phases. (b) Nucleus at the nanowire-liquid interface, with interfaces of interest. (c) Nucleus originating at the triple phase line. Transferring the nucleus to the triple phase line eliminates and creates interfacial areas, indicated by thick lines in (b) and (c). Adapted from Ref. ⁴.

This observation alone, however, does not explain exactly why wurtzite forms instead of zincblende. To understand, we start by taking into consideration a solid 2D nucleus of III-V material forming between the top surface of a nanowire and the catalyst, entirely surrounded by the latter, as shown in Fig.2.1b. Its formation requires a change of free enthalpy which can be written as

$$\Delta G = -Ah\Delta\mu + Ph\gamma_{lL} + A\gamma_{SN} \quad (2.1)$$

where $\Delta\mu > 0$ is the difference of chemical potential for III-V pairs between liquid and solid phases, per unit volume of nucleus; P is the perimeter of the nucleus, γ_{lL} is the energy per unit area of the lateral interface between nucleus

and liquid; γ_{SL} , γ_{SN} , γ_{NL} are, respectively, the energies per unit area of the substrate-liquid, substrate-nucleus and upper nucleus-liquid interfaces. A 2D nucleus, corresponding to a single monolayer, cannot be defined as ZB or WZ, as they are defined by the stacking of multiple monolayers (ABC vs. AB) as shown in Fig.2.2a. However, the nucleus orientational positioning is different in the two cases: in the ZB case, the GaAs₄ tetrahedra in the nucleus have the same orientation as the previous monolayer in the nanowire. In the WZ case, they are rotated by an odd multiple of $\pi/3$ as shown in Fig.2.2b. The consequence is an additional cost to form WZ ($\gamma_{SN}^{WZ} = \gamma_F$) instead of ZB ($\gamma_{SN}^{WZ} = 0$) due to second-nearest neighbor interaction. As γ_{LL} is the same for both ZB and WZ, the formation of ZB is always favored in case the nucleus is completely surrounded by the catalyst, therefore away from the triple phase line. However, the experimental observations show WZ formation, therefore the WZ monolayers cannot have nucleated within the droplet like in Fig.2.1b, but at the triple phase line as in Fig.2.1c.

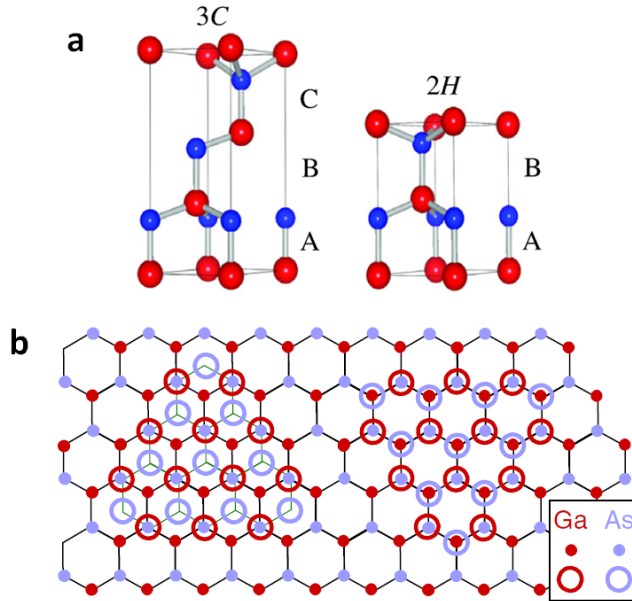


Figure 2.2: (a) Schematic representation of Zincblende (3C) and Wurtzite (2H) crystal structures, highlighting the ABC and AB stacking orders. (b) A given nucleus (empty large circles) in ZB (left) and WZ (right) positions on top of a (111)B monolayer (full small circles). Notice the rotation of the III-V tetrahedra between the ZB and WZ case. Adapted from Ref. ⁴.

Therefore, we now consider the case of nucleus formation at the triple phase line as shown in Fig.2.1c. In this case, an area s of the newly formed nucleus-vapor interface replaces an area τs of liquid catalyst-vapor interface, where τ is a geometrical parameter. If α is the fraction of the nucleus perimeter in contact with the vapor, its formation enthalpy becomes

$$\Delta G(\alpha) = -Ah\Delta\mu + Ph[(1 - \alpha)\gamma_{IL} + \alpha(\gamma_{IV} - \tau\gamma_{LV})] + A\gamma_{SN} \quad (2.2)$$

where γ_{IV} is the energy per unit area of the nucleus-vapor interface, γ_{LV} is the energy per unit area of the liquid-catalyst vapor interface and τ can be estimated as $\tau = \sin\beta$, where β is the contact angle between droplet and nanowire, as shown in Fig.2.1c. The formation enthalpy difference between positions (1) and (2) is

$$\Delta G(\alpha) - \Delta G(0) = \alpha Ph(\gamma_{IV} - \gamma_{IL} - \gamma_{LV} \sin\beta) \quad (2.3)$$

From TEM observations, the contact angle is often close to $\beta \approx \pi/2$: Young's equation for the interface energies at the contact angle yields $\gamma_{IV} \approx \gamma_{IL}$, through which the inequality condition for the formation of wurtzite is approximately reduced to

$$\gamma_{LV} \sin\beta > 0 \quad (2.4)$$

As γ_{LV} lies between the surface energies of pure liquid Au and Ga (1.14 and 0.72 J · m⁻²), the inequality is easily satisfied and the nucleus should always form at the triple phase line. In conclusion, this result means that the nucleation happens at the triple phase line due to the energetically favorable replacement of the liquid catalyst surface by the nucleus surface. Now we want to understand why WZ nucleates instead of ZB. To do this, we consider the atomic structure of the top facet of the nanowire and of the nucleus, and in particular its edge confining with the vapor phase, as illustrated in Fig.2.3. Nucleating a monolayer of ZB or WZ entails strong differences on the side facet orientations. The ZB nucleus will develop tilted sidewall facets, {111}A type at Ga edges (j=A), {111}B type at As edges (j=B). The WZ nucleus instead will develop {10 $\bar{1}$ 0} facets parallel to the nanowire axis (j=W). Therefore the effective energy per unit area $\tilde{\gamma}_j$ depends on the configuration j, as the lateral facets will be different and as they will form different angles Θ_j with the nanowire axis, therefore changing the contact angle β . We therefore conclude that the formation enthalpy of the monolayer nucleus is configuration dependent. Knowing the aforementioned three possible configurations (A,B,W) we can define the two conditions for WZ nucleation. First, $\tilde{\gamma}_W < \tilde{\gamma}_{A,B}$, which is material-related as it involves only interface energies. Second, the supersaturation is required to be larger than a critical

value $\Delta\mu > \Delta\mu_C$ in order to reach the inequality between nucleation free energies $\Delta G_{WZ}^* < \Delta G_{ZB}^*$, to ensure the formation of WZ exclusively and avoid stacking faults. Both the interface energies and the supersaturation are affected by the growth conditions, explaining why it is possible to obtain both zincblende and wurtzite nanowires, as well as mixed-phase ones.

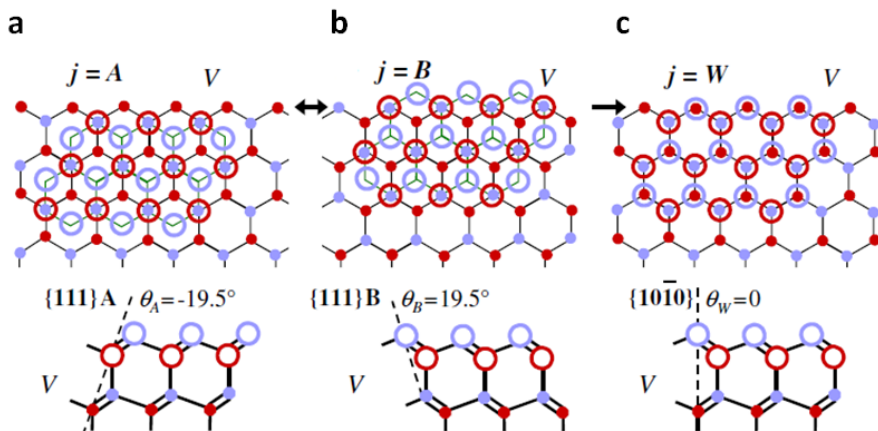


Figure 2.3: Top (top row) and side (bottom row) views of a given nucleus in ZB (a,b) and WZ (c) positions at Ga (a,c) or As (b) edges of the top facet. The side facet is located to the left of the scheme. Edges are indicated by arrows (top), the vapor side by V, and nonvertical dangling bonds by segments (bottom). Adapted from Ref. ⁴.

2.2 Band structure of wurtzite III-Phosphides

The band structure of the wurtzite III-phosphides GaP, InP and AlP has been theoretically predicted with density functional theory (DFT) calculations²⁶ and experimentally studied in the case of WZ InP⁴⁵ and WZ GaP⁴⁶. In this section the band structure of these compounds and the resulting optical properties will be discussed.

2.2.1 Density functional theory calculations

The many-body Schroedinger equation contains, in principle, all the information about a certain quantum system. However, when trying to simulate the band structure of a material, such problem is intractable both analytically and computationally with exact wavefunction-based approaches, due to its extreme

complexity, as an N -electron system is dependent on $3N$ variables (three spatial variables for each electron). The density functional theory (DFT), originated from the work of P. Hohenberg and W. Kohn, allows to find an approximate solution by reducing the intractable many-body problem to a tractable problem of non-interacting electrons moving in an effective potential⁴⁷. In this framework, the basic quantity used is the ground state electron density $n(\mathbf{r})$:

$$n(\mathbf{r}) = \sum_i |\Psi_i(\mathbf{r})|^2 \quad (2.5)$$

where $\Psi_i(\mathbf{r})$ are the electron ground state wavefunctions. $n(\mathbf{r})$ depends only on the 3 spacial variables, therefore greatly reducing the complexity of the entire problem. The total energy of the system can be thus calculated as a functional of the electron density. As the electrons in this theory are non-interacting, in order to obtain a more realistic result the local density approximation (LDA) is used, which derives from the homogeneous electron gas model. In LDA the energy depends only on the point where the functional is calculated and with this approximation the exchange-correlation energy from electron-electron interaction can be taken into account. A DFT calculation starts with the assumption of a certain electronic density, for which the Schroedinger equation is solved, yielding the single-particle wavefunctions. From these a new electronic density is calculated and the process continues iteratively until the calculation converges to a self-consistent solution. DFT calculations were performed to predict the band structure and the optical transitions of the hexagonal III-phosphides relevant for this work: WZ GaP, WZ InP, WZ AlP. Effective masses and transition energies in these compounds are listed at the end of the chapter, in Tables 2.2, 2.3 and 2.1.

2.2.2 Selection rules

A two-level transition process in quantum mechanics is described by the coupling of electron and photon, through time-dependent perturbation theory⁴⁷. Where $\hat{\mathbf{H}}'$ is the perturbed Hamiltonian, Fermi's golden rule quantifies the transition rate W_{fi}

$$W_{fi}(\hbar\omega) = \frac{2\pi}{\hbar} |H'_{fi}|^2 \delta(E_f - E_i - \hbar\omega) \quad (2.6)$$

where $\hbar\omega$ is the photon energy, E_i (E_f) is the energy of the initial (final) state. H'_{fi} is the matrix element

$$H'_{fi} = \langle \Psi_f | \hat{\mathbf{H}}' | \Psi_i \rangle \quad (2.7)$$

where Ψ_i (Ψ_f) are the wavefunctions of the unperturbed initial (final) state. In the *electric dipole approximation* the perturbation operator $\hat{\mathbf{H}}_{\mathbf{em}}$ is simplified as

$$\hat{\mathbf{H}}_{\mathbf{em}} \approx q\mathbf{r} \cdot \mathbf{E} \quad (2.8)$$

where q is the electron charge, \mathbf{r} is the electric dipole and \mathbf{E} is the electric field. From this functional form, we can know the symmetry of $\hat{\mathbf{H}}_{\mathbf{em}}$. We see from 2.6 that W_{fi} is non-zero only if H'_{fi} is non-zero. Therefore we have to evaluate 2.7, which we find to be dependent to the symmetry of the wavefunction and the dipole operator. Therefore, for H'_{fi} to be non-zero, meaning a transition to be allowed, it has to respect the following symmetry rule

$$\Gamma_f \otimes \Gamma_d \otimes \Gamma_i = \Gamma_{tot} \quad (2.9)$$

where Γ_i (Γ_f) is the symmetry of the initial (final) state, Γ_d is the symmetry of the electric dipole operator and Γ_{tot} is the total-symmetry group. The symmetry of the electric dipole is uneven, as it depends on the (x, y, z) dipole vector. Therefore, in order to yield Γ_{tot} , Γ_i and Γ_f need to have opposite parity (e.g. Γ_i even, Γ_f uneven). When this condition is verified, the transition is allowed, otherwise it is forbidden⁴⁷.

2.2.3 GaP

Gallium Phosphide (GaP) in bulk is always found in Zincblende (ZB) symmetry, where it is an indirect semiconductor with a conduction band minimum (CBM) close to the X-point with a band gap of 2.26 eV. The second CBM in the L-point at 2.6 eV and finally the direct gap in Γ at 2.78 eV. The link between the ZB and WZ band structures is the following: the hexagonal structure has 4 atoms per cell, while the cubic structure only 2, therefore there are twice as many bands per k points in the wurtzite structure. Two k points on the zincblende $\Gamma - L$ line fold onto one k point in the $\Gamma - A$ line of the hexagonal Brillouin zone. Also, WZ and ZB band gaps are very similar, as in WZ the folded bands derive from the ZB bands, and are therefore located at similar energies. In the case of WZ GaP, the L_{1C} minimum folds into the Γ_{8C} CBM, yielding a pseudo-direct band gap and pushing at higher energy the Γ_{7C} band. The $\Gamma_{8C} - \Gamma_{9V}$ transition is forbidden as both bands have p-like (uneven) symmetry, therefore yielding zero oscillator strength in the electric dipole approximation. Being GaP a pseudo-direct semiconductor it is expected to be an inefficient light emitter at room temperature. Band structure and optical transitions of GaP are shown in Fig.2.4.

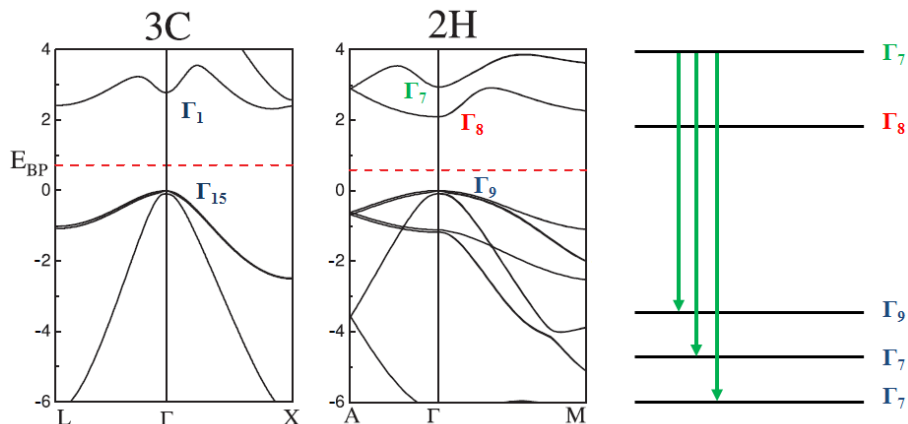


Figure 2.4: Left: detail of ZB GaP band structure (3C symmetry). Center: detail of WZ GaP band structure (2H symmetry). Right: schematic of the allowed (green) transitions in WZ GaP, according to the predicted oscillator strengths. Partially adapted from Ref.²⁶.

2.2.4 InP

Indium Phosphide (InP) is a direct semiconductor both in ZB and WZ symmetry. In ZB, the L_{1c} minimum is well above the Γ_{1c} CBM, therefore the folding maintains the band order, making WZ InP a direct semiconductor with the allowed transition $\Gamma_{7C} - \Gamma_{9V}$ across the band gap. Not only efficient emission, but also lasing has been demonstrated at room temperature for WZ InP²⁹, which certainly makes it an excellent candidate for solid state lighting. However, the low band gap around 1.5eV makes it an infrared emitter, therefore alloying with a higher band gap material, such as GaP and/or AlP is necessary to enter the visible region. Band structure and optical transitions of InP are shown in Fig.2.5.

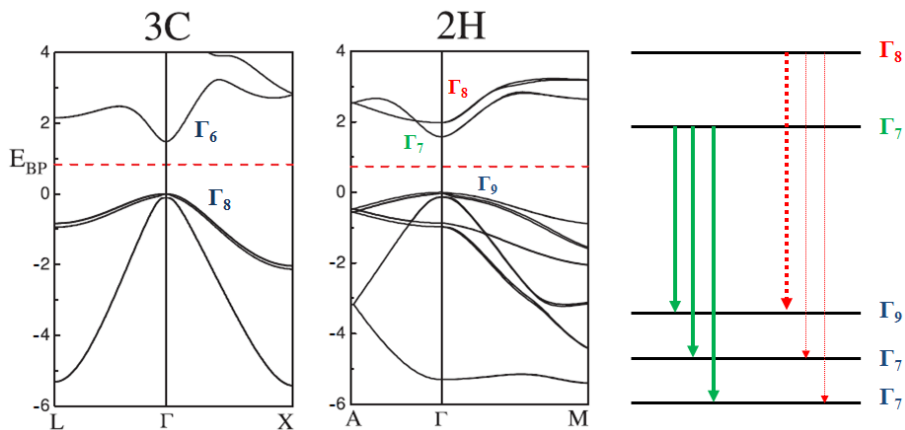


Figure 2.5: Left: detail of ZB InP band structure (3C symmetry). Center: detail of WZ InP band structure (2H symmetry). Right: schematic of the allowed (green) and weak (red) transitions in WZ InP. A thicker red line indicates a relatively higher oscillator strength. Partially adapted from Ref.²⁶.

2.2.5 AlP

AlP is always an indirect semiconductor, both in the Zincblende ($E_g = 2.45\text{eV}$) and Wurtzite symmetry (predicted $E_g = 3.025\text{eV}$). In fact, the folding of the L minimum in Γ leads to a Γ_{8C} minimum which is still higher than the new M minimum. Moreover, as the lowest Γ point in the conduction band is Γ_{8C} , the transition with the Γ_{9V} highest valence band is forbidden. However, a small oscillator strength is predicted, although more than 2 orders of magnitude lower than

the $\Gamma_{7C} - \Gamma_{9V}$ transition. AIP is therefore an uninteresting material for optical applications in both the ZB and WZ configurations. However, as it possesses a high band gap, alloying with InP should lead eventually to a direct-allowed band gap material in the visible range. Band structure and optical transitions of AIP are shown in Fig.2.6.

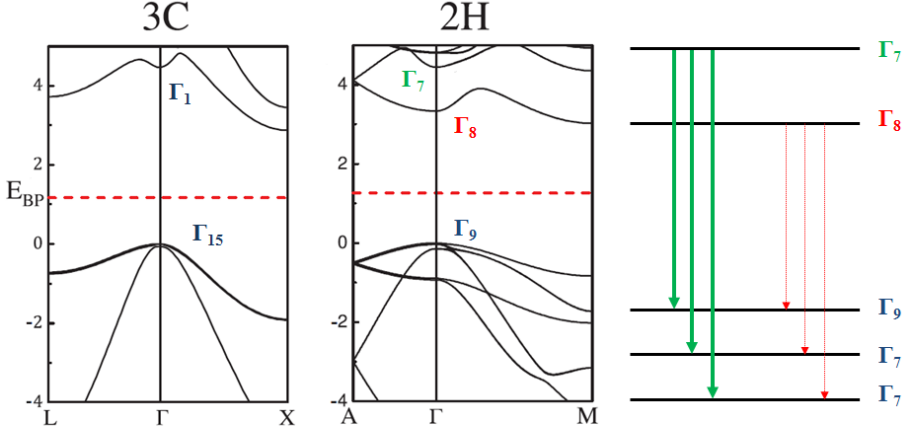


Figure 2.6: Left: detail of the ZB AIP band structure (3C symmetry). Center: detail of WZ AIP band structure (2H symmetry). Right: schematic of the allowed (green) and forbidden (red) transitions, according to the predicted oscillator strengths. Partially adapted from Ref. ²⁶.

	m_{hh}^A	m_{lh}^A	m_{so}^A	m_{e1}^A	m_{e2}^A	m_{hh}^M	m_{lh}^M	m_{so}^M	m_{e1}^M	m_{e2}^M
WZ GaP	1.13	0.87	0.13	1.18	0.16	0.28	0.31	0.52	0.18	0.25
WZ InP	0.13	0.29	0.10	0.09	0.13	0.19	0.22	0.55	0.15	1.26
WZ AIP	1.37	0.97	0.19	1.14	0.18	0.20	0.22	0.91	0.22	0.42

Table 2.1: WZ GaP: effective heavy-hole (hh), light-hole (lh), spin-orbit split-off masses and electron (e) masses in the lowest (1) or second lowest (2) conduction band for Γ_A and Γ_M directions. All effective masses are given in units of the free electron mass m . Adapted from Ref. ²⁶.

2. Theoretical concepts: from wurtzite growth to band structure

Structure	$E_g(\text{eV})$	$\Delta_{SO}(\text{eV})$	$\Delta E_V(\text{eV})$	$\Delta E_C(\text{eV})$
WZ GaP (Γ)	2.123	0.083	0.135	-0.474
WZ GaP (M)	2.266			-0.389
ZB GaP (Γ)	2.790	0.082		0
ZB GaP (X)	2.330			-0.460
WZ InP (Γ)	1.576	0.1	0.082	0.183
ZB InP (Γ)	1.475	0.104	0	0
WZ AlP (Γ)	3.335	0.062	0.123	-1.000
WZ AlP (M)	3.025			-1.310
ZB AlP (Γ)	4.458	0.061	0	0
ZB AlP (X)	2.877			-1.581

Table 2.2: Characteristic parameters of the WZ and ZB band structures of GaP and InP from approximate quasiparticle calculations including spin-orbit interaction. The band offsets ΔE_C and ΔE_V are given with reference to E_C and E_V in the ZB phase. Adapted from Ref.²⁶.

Material	Transition	Transition energy (eV)	Transition strength \perp (eV)	Transition strength \parallel (eV)
WZ GaP	$\Gamma_{9V} - \Gamma_{7C}(\Gamma_{8C})$	2.888 (2.123)	6.30 (0)	0 (0)
	$\Gamma_{7+V} - \Gamma_{7C}(\Gamma_{8C})$	2.929 (2.220)	5.66 (0)	2.05 (0)
	$\Gamma_{7-V} - \Gamma_{7C}(\Gamma_{8C})$	3.104 (2.404)	0.59 (0)	18.55 (0)
WZ InP	$\Gamma_{9V} - \Gamma_{7C}(\Gamma_{8C})$	1.576 (1.929)	8.85 (0.245)	0.011 (0)
	$\Gamma_{7+V} - \Gamma_{7C}(\Gamma_{8C})$	1.589 (1.967)	7.75 (0.016)	9.58 (0.016)
	$\Gamma_{7-V} - \Gamma_{7C}(\Gamma_{8C})$	1.703 (2.080)	4.15 (0.011)	17.46 (0.027)
WZ AlP	$\Gamma_{9V} - \Gamma_{7C}(\Gamma_{8C})$	4.445 (3.335)	8.06 (0.027)	0 (0)
	$\Gamma_{7+V} - \Gamma_{7C}(\Gamma_{8C})$	4.479 (3.367)	7.75 (0.016)	6.85 (0.003)
	$\Gamma_{7-V} - \Gamma_{7C}(\Gamma_{8C})$	4.594 (3.482)	2.10 (0.005)	25.06 (0.011)

Table 2.3: Optical transitions in WZ GaP, InP and AlP between bands of Γ_{9V} and $\Gamma_{7C}(\Gamma_{8C})$ symmetry. Listed are the predicted transition energies and transition strengths in eV. Adapted from Ref.²⁶.

2.2.6 Alloy band structure

Alloys of two semiconductors usually possess intermediate properties between the two pure materials they descend from. Vegard's law, derived from empirical observation, states that the lattice parameter of the alloy can be assumed as linearly dependent from the composition. Considering the III-V alloy $\text{In}_x\text{Ga}_{1-x}\text{P}$ we can write:

$$a_{\text{InGaP}} = xa_{\text{InP}} + (1-x)a_{\text{GaP}} \quad (2.10)$$

In this work, the lattice parameter of the studied hexagonal alloys was assumed to follow Vegard's law. The band gap of semiconductors is often related to the lattice parameter. Having stated the linear dependence of the lattice parameter to the composition, we can also expect a linear dependence of the band gap. However, it is often found that a linear relation cannot model properly the empirical data, therefore a band bowing term is introduced, giving origin to a parabolic function. Considering again $\text{In}_x\text{Ga}_{1-x}\text{P}$ we have

$$E_{g,\text{InGaP}} = xE_{g,\text{InP}} + (1-x)E_{g,\text{GaP}} - bx(1-x) \quad (2.11)$$

where b is the band bowing parameter. Such bowing can be due to different phenomena, first of all the random distribution of the substitutional atoms in the alloy, which partially breaks the translational symmetry. The band gap of an alloy varies because the positions in energy of the electronic bands change. As they move in energy, their order can also change, leading to crossovers. We have seen that WZ GaP, WZ InP and WZ AlP have, respectively, a pseudo-direct, direct and indirect band gap. The order of their CBM at the Γ point is in fact different. We can expect therefore that their alloys will have intermediate properties, thus leading to conduction band crossovers.

Chapter 3

Experimental methods, techniques and fabrication

In this chapter we discuss the methodology used for the metalorganic vapour phase epitaxy (MOVPE) growth, starting from the substrate patterning with nanoimprint and electron beam lithography. We illustrate the structural characterization of nanowires with scanning and transmission electron microscopy (SEM and TEM). We then discuss the optical characterization methods with photoluminescence.

3.1 Substrate preparation

Nanowire growth requires a careful substrate preparation in order to obtain high quality material. Two are the growth techniques used in this work: vapor-liquid-solid (VLS), using an array of gold catalyst droplets, and selective area, where nanowires grow through openings in a patterned silicon nitride (SiN_x) mask. In this thesis, the patterns for nanowire growth were fabricated by using two different techniques: nanoimprint and electron beam lithography (EBL).

3.1.1 Nanoimprint lithography

Nanoimprint lithography consists of the mechanical transfer of a predetermined shape into a resist by simple physical contact. A stamp in PDMS contains the negative of the features that need to be transferred into the resist. It is fabricated from a silicon master obtained with EBL lithography, where the positive features reside. The strategy of this whole process is to shorten the patterning time: exposing to EBL entire wafers might take a considerable amount of time, while

here only one EBL exposure is needed and the entire information is transferred chemically and mechanically in a shorter time.

The process starts with the spinning of a polymethylmetacrylate (PMMA) layer on the substrate, which will constitute the soft mask, 300nm thick. The PMMA is baked at 150°C for 15 minutes on a hot plate. Then, a layer of silicon oxide (SiO_2) sol-gel is spun on top of the baked PMMA. The PDMS stamp is carefully applied on top of the wafer by hand or by vacuum contact, making sure that no eventual air bubbles are left trapped under it. After about 3 hours, the stamp is removed by carefully peeling it off the substrate. The wafer is then treated with Reactive Ion Etching (RIE): first in a mixture of CHF_3/O_2 plasma to etch the SiO_2 hard mask, then in pure O_2 plasma which etches the PMMA layer, forming the soft mask. The wafer is rinsed in Orthophosphoric Acid (H_3PO_4) or Hydrofluoric Acid (HF) to eliminate any surface oxide generated during the last RIE step, then a layer of gold is Evaporated. Part of the gold will land on the mask, part on the substrate, defining the catalyst structures. The PMMA is then dissolved using Acetone, allowing the lift-off of the undesired gold layer, leaving only the gold nanostructures on the substrate.

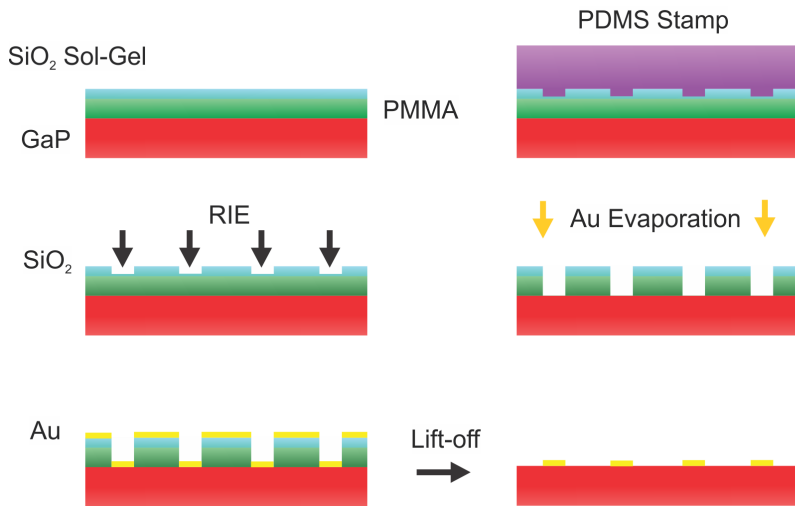


Figure 3.1: Nanoimprint lithography procedure. PMMA and SiO_2 sol-gel are spun on the substrate, then a PDMS stamp is used to imprint the nanofeatures. Two steps of RIE are used to open the features, then a gold layer is evaporated. Finally, the lift-off step is performed, leaving only the catalyst array on the substrate.

3.1.2 Electron beam lithography

EBL is based on the reactivity of a polymer to an electron beam, which changes its solubility and allows its selective removal with a solvent. The advantage of EBL is the higher resolution, which can produce features down to 10nm of diameter, allowing the fabrication of nanometric Au catalyst droplets or holes in a SiN_x mask. EBL is used when such resolution is necessary and cannot be provided by nanoimprint lithography, due to the physical constraints of the PDMS stamp. EBL lithography is performed on a Raith EBPG 150. The resist used is ZEP 520 with fullerene C₆₀ (positive resist), spun uniformly over the substrate, reaching a final thickness of 20nm. The resist is exposed to an electron beam, which enhances the solubility of the exposed area. It is then developed using n-amyl acetate and MIBK selective solvent, followed by gold evaporation. The lift-off is performed with PRS3000 and acetone.

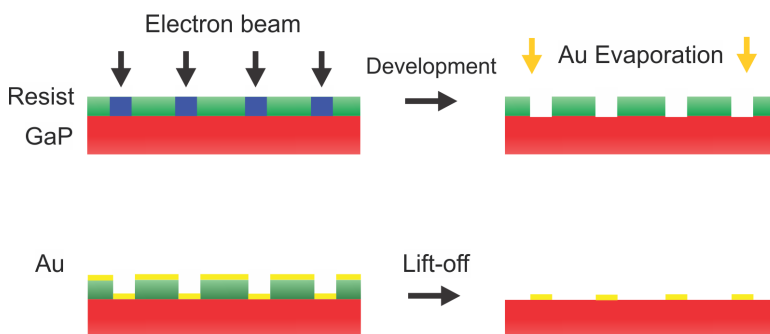


Figure 3.2: Electron beam lithography procedure. An electron-sensitive resist is spun on the substrate, which is then exposed to the electron beam. After development in a selective solvent, a metallic layer is evaporated. The final lift-off step defines the catalyst array.

3.1.3 Silicon nitride mask

In order to chemically isolate the substrate during VLS growth, or to perform catalyst-free selective area epitaxy, a Silicon Nitride (SiN_x) mask can be fabricated by depositing a layer of SiN_x on the substrate itself before the nanoimprint procedure. Before the eventual Au deposition, one more dry etching step will be required to open holes in the SiN_x and expose the substrate. Such mask is useful to avoid unwanted layer growth on the substrate during VLS growth or during shell growth, allowing a more controlled nanowire morphology and easier photoluminescence interpretation.

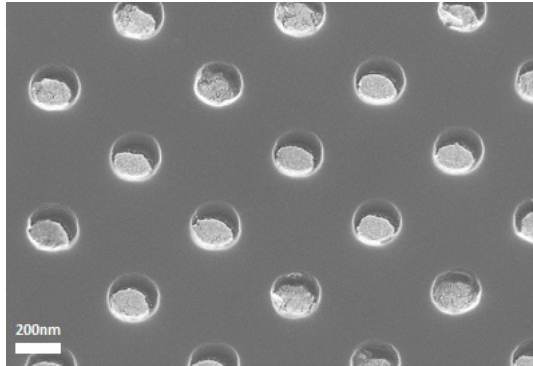


Figure 3.3: Nanoimprinted SiNx mask with 16nm thick Au disks. Such disks will then become droplets when heated in the MOVPE reactor. A droplet filling step is also performed before the actual growth by providing a flow of group III precursor.

3.1.4 Pre-deposition cleaning

The catalyst particles fabrication process can leave amounts of organic contaminants which can negatively affect the nanowire growth quality. In order to eliminate most of these residues, a cleaning step is necessary, for instance using piranha wet etching. The piranha solution used consisted in [4:1:1] concentrations of H_2SO_4 , H_2O , H_2O_2 . Oxygen plasma is also a viable alternative, especially when the piranha solution might etch the substrate as well, as in the case of InP. In order to make sure that all contaminants have been eliminated, a high-temperature annealing step is performed before each growth.

3.2 MOVPE

Metal-Organic Vapor Phase Epitaxy (MOVPE) is one of the main methods for nanowire growth, alongside Molecular Beam Epitaxy (MBE). The main advantage of MOVPE is a great flexibility in the choice of precursors and high growth rate. These are the main reasons why MOVPE and Chemical Vapor Deposition (CVD) in general are the most common methods of semiconductor growth in industrial applications. Two types of precursors were used in this thesis: metalorganics (e.g. Trimethylgallium, TMGa) and hydrides (e.g. Phosphine, PH_3). The metalorganic precursors are stored in bubblers, immersed in a thermal bath to allow better control on the mass flow, and are transported to the reaction chamber by a carrier gas, molecular Hydrogen (H_2). The samples are positioned on a graphite heater plate (susceptor), usually situated in the middle of the re-

action chamber, which is kept at low pressure, about 10-50mbar. Two reactors have been used in this work, which are described below.

3.2.1 Showerhead reactor

The Aixtron-CSS reactor operates in showerhead configuration. The precursors are therefore injected into the reaction chamber uniformly from directly above the samples: this geometry and the low pressure contribute to establish a laminar flow of precursors over the susceptor where the samples reside. The temperature of the sample allows the decomposition of the precursors on its surface and provides the energy needed for the deposition reaction.

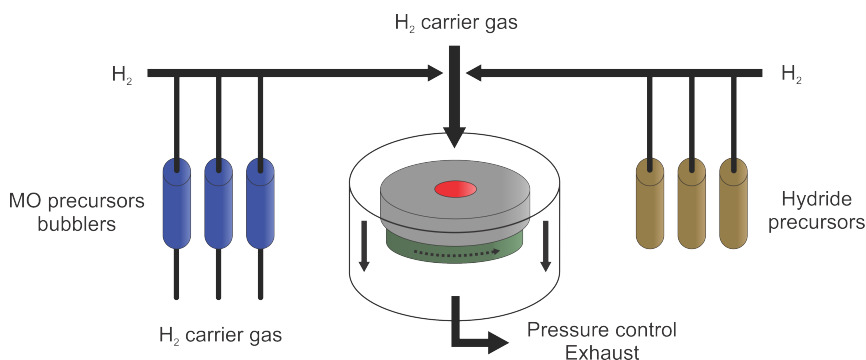


Figure 3.4: Showerhead MOVPE reactor scheme. Two types of precursors are used: metalorganic, typically carrying the group III atom and hydrides, typically providing the group V element. The gasses are mixed with the carrier gas, hydrogen, and injected in the chamber through a showerhead system above the susceptor, where the substrate (here in red) is located.

3.2.2 Horizontal flow reactor

The Aixtron 200 reactor operates in the horizontal flow geometry. The precursors are mixed with the carrier gas and injected into a transparent quartz tube where they flow horizontally over a graphite susceptor, heated by infrared lamps positioned outside the reactor. Compared to the showerhead system, the horizontal flow reactor provides with a slightly different reaction chemistry, as the precursors are heated by the infrared radiation before they reach the susceptor itself. The cracking of the precursor molecules therefore starts in the gas phase.

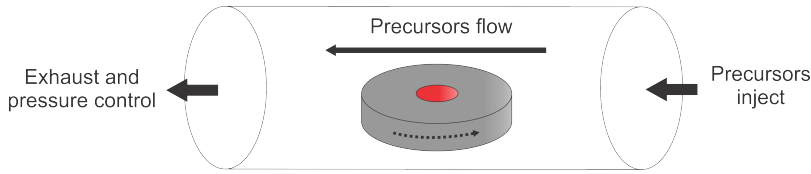


Figure 3.5: Horizontal flow MOVPE reactor scheme. The system is analogue to the showerhead reactor, but with the substantial difference that, using IR lamps, the precursors are heated already before reaching the susceptor. The growth results are however usually very similar between the two systems.

3.2.3 Cleaning and memory effect

In order to obtain high quality single crystals with high purity and low defectivity, the reaction conditions need to be optimal, especially when involving complex reaction mechanisms such as VLS. Due to the fact that the entire susceptor is heated, the precursors react not only on the samples, but on the entire hot surface, depositing a layer of material which is present also after the growth. This fact has to be taken into account when planning each growth, to avoid cross-contaminations which can alter the outcome of an experiment. Therefore, before growth, standard preparation recipes are run in order to bring the reactor to a known optimal state. The first important effect of this protocol is to ensure the cleaning of the reactor, minimizing any impurity i.e. Indium in GaP growth. Another important effect is the amount of material present on the susceptor during a growth: such material can be desorbed in non-negligible quantities and take part into the reaction, constituting a substantial precursor flow which cannot be ignored.

3.3 Scanning electron microscopy (SEM)

Scanning Electron Microscopy (SEM) is a necessary analysis technique for nanostructure development. Due to its relative simplicity and immediate accessibility, it can provide a fast feedback for nanowire epitaxy.

The electron source used is a Tungsten tip maintained under a bias of about 10 kV, generating a current of a few μA . The formation and manipulation of the electron beam is possible through a series of charged plates and magnetic lenses. The beam can therefore be focused to a fraction of nanometers of diameter, providing with an imaging resolution sufficient to study nanostructures. The electron beam is steered towards a rectangular matrix on the target (raster scanning). When the beam hits the material, backscattered electron (BSE), secondary electron (SE), Auger electrons (AE) and X-rays are emitted. The secondary electrons are col-

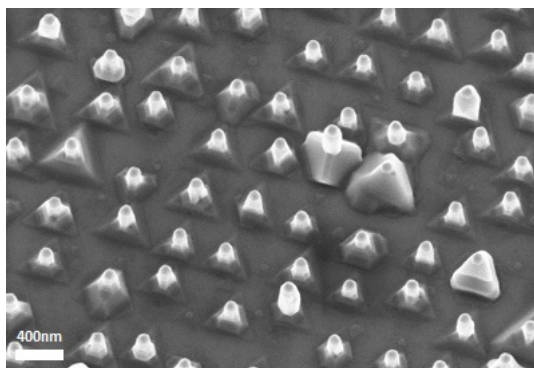


Figure 3.6: GaP nanowires growth attempt on (111)B GaP, using an Indium-polluted susceptor. Due to the Indium contamination, the supersaturation of the droplet is very different from the intended value and the growth rate is orders of magnitude lower than expected.

lected by an annular detector located in the terminal part of the column (in-lens), giving topographic information of the analyzed sample. The SEM images shown in the present work are all generated through secondary electrons.

3.4 Transmission electron microscopy (TEM)

The TEM is very similar to an SEM but differs in type of signal detected and overall purpose. In this case the electron beam is accelerated enough to be transmitted through a thin sample. The objective magnetic lens in a TEM is situated beyond the sample. A TEM can usually accelerate electrons with a bias of hundreds of kV, which gives them a wavelength small enough to resolve the dumbbells of single rows of atoms in a crystal, allowing to observe directly the crystal symmetry. Like the SEM, also the TEM can use EDS analysis to determine the composition of a sample, exploiting the advantage of a higher beam current and acceleration, which allows for a higher signal to noise ratio, and higher spatial resolution.

3.4.1 TEM modes

The bright field imaging mode is the most commonly used in TEM. The contrast is formed by scattering and absorption of electrons while transiting through the sample. Thicker regions will appear darker, as well as regions containing atoms with a higher atomic number. Strain can as well modify the contrast of an im-

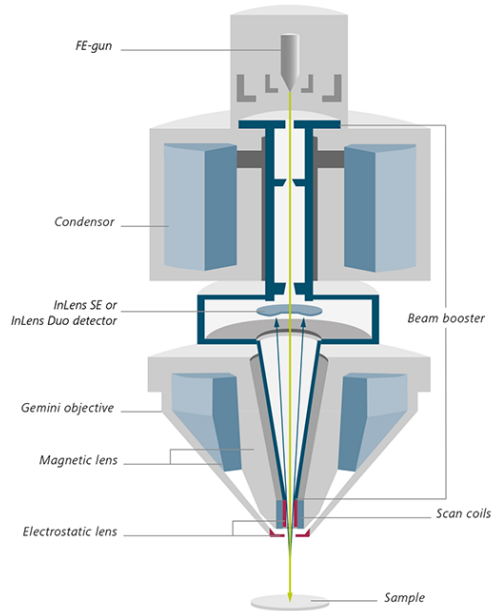


Figure 3.7: Schematic representation of an SEM column in section. Adapted from Zeiss documentation.

age, by changing the interference pattern of the transmitted electrons. In the scanning-TEM (STEM) mode the beam is concentrated into a spot and used to scan the sample in a raster, where the signal corresponding to each point constitutes a pixel of the final image. Three detectors can be available, depending on the microscope: the bright field (BF), the annular dark field (ADF) and the high-angle annular dark field (HAADF). In the bright field mode, imaging resolutions of about 1\AA can be achieved: when observing a crystal, the sample can be oriented along a specific zone axis and individual rows of atoms can be detected showing a characteristic "dumbbell" shape. Electron diffraction through the crystal and the observation of the dumbbells are useful to determine the crystal symmetry, the lattice parameter and eventual strain phenomena. The HAADF detector collects electrons scattered at high angles by the specimen, making it highly sensitive to the composition of the observed material and in particular to the atomic number (Z). The HAADF-STEM mode therefore yields images with Z-contrast, useful to highlight compositional changes and often performed in parallel with Energy Dispersive X-Ray Spectroscopy (EDS) spectroscopy. Due to the high energy of

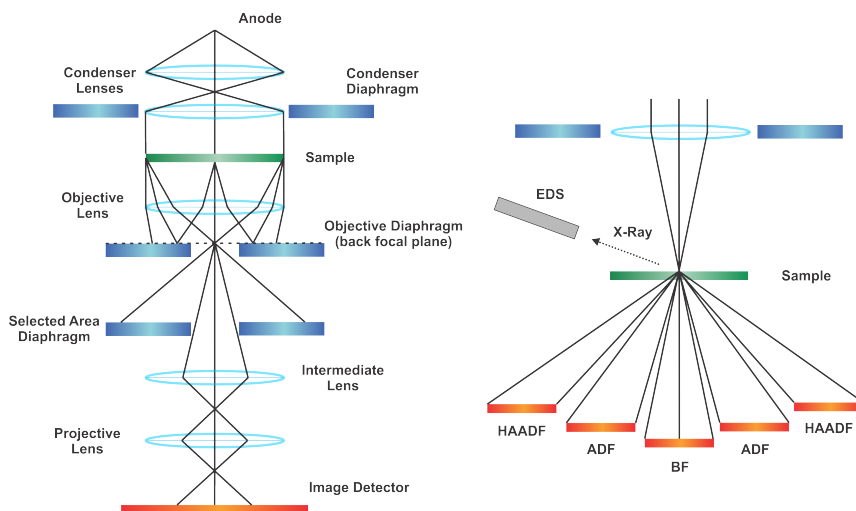


Figure 3.8: Left: Ray diagram for a TEM in imaging mode. Magnetic lenses and diaphragms allow to manipulate and focus the electron beam. Right: STEM mode. Different modes can be used: bright field (BF), annular dark field (ADF) and high-angle annular dark field (HAADF), which is often used together with EDS as the resulting image is strongly atomic number sensitive.

the beam in fact, the collisions will induce transitions involving core electrons. These transitions will result in the emission of X-Ray photons, which can be collected and analyzed through a dedicated X-ray spectrometer. Being the energy of these transitions a specific property of the atoms involved, one can quantify the composition of a material. All the TEM analysis contained in this work were performed by Dr. M.A. Verheijen.

3.4.2 Cross-sectional analysis

In a TEM, transparency of the sample to the electron beam is an important parameter: a too thick sample will hinder the electron beam in such a way that a detailed analysis may not be possible. Also, additional information about the inner morphology of a certain structure may be desired. A sample can be therefore cut using a Focused Ion Beam (FIB) while being held in place by a metal layer (e.g. a Cobalt cladding), allowing a nanostructure to be cut transversally in a thin lamella, thin enough to be observed in a TEM. Such technique is necessary to properly observe the radial development of core-shell nanowires.

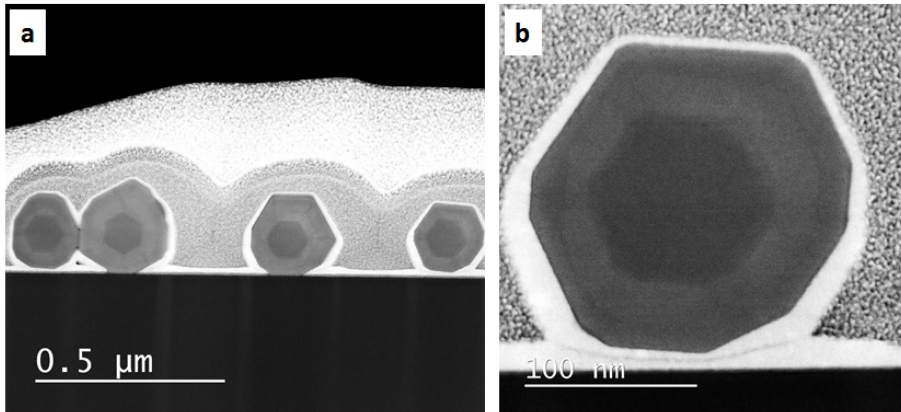


Figure 3.9: (a) TEM image of 100nm-thick lamellae of WZ $\text{In}_x\text{Ga}_{1-x}\text{P}$ nanowires, embedded in cobalt and platinum in a TEM window. The underlying substrate is silicon (b) Close-up TEM image of a single 100nm-thick lamella of a WZ $\text{In}_x\text{Ga}_{1-x}\text{P}$ nanowire

3.4.3 Nanomanipulation

In order to study single nanowires, it is sometimes necessary to transfer them individually. For example, in Fig.3.10 we show the successful transfer of two WZ $\text{Al}_x\text{In}_{1-x}\text{P}$ nanowires to a carbon mesh grid in order to perform TEM-EDS analysis. As these nanowires have a low aspect ratio, they cannot be simply broken off by mechanical rubbing of the TEM grid on the sample, but require to be picked singularly with the nanomanipulation needle shown in Fig.3.10a.

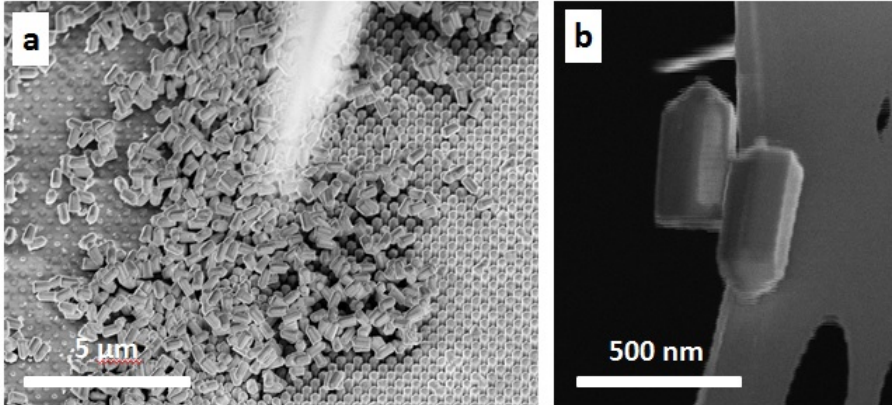


Figure 3.10: (a) SEM image of $\text{Al}_x\text{In}_{1-x}\text{P}$ nanowires during the nanomanipulation process. The nanowire array is visible (right), as well as bunches of freestanding nanowires lying on the InP/SiN_x substrate. (b) SEM image of two WZ $\text{Al}_x\text{In}_{1-x}\text{P}$ nanowires transferred on a carbon mesh grid for TEM analysis.

3.5 Photoluminescence

Every material has a characteristic electronic structure in which electrons can perform energy transitions. Some of these transitions involve photons and can be explored through optical means. In a luminescence experiment the electrons of a sample are excited through one of different means (e.g. photons, current, electron beam) in order to let them return to their original energetic states by emitting photons. These photons can be collected and used for extensive analysis aimed towards the understanding of the electronic structure of the sample involved.

In a photoluminescence (PL) experiment photons are generated from a known source and focused on a sample, which will in turn emit other photons at a different wavelength. When studying a semiconductor sample, the energy of the excitation photons is usually chosen to be higher than the band gap: the electrons of the valence band will then be excited to states of the conduction band, leaving an empty state, called hole, in the valence band. In a perfect semiconductor electrons and holes will thermalize and gather at the conduction and valence band extrema. If the semiconductor has a direct band gap and the transition is allowed (the oscillator strength is non-zero), electrons and holes will recombine, emitting a photon through a band to band transition.

Other radiative recombination mechanisms can also take place. Excitons are quasiparticles formed by an electron in the conduction band and a hole state in the valence band, due to their reciprocal Coulomb attraction. As it is formed

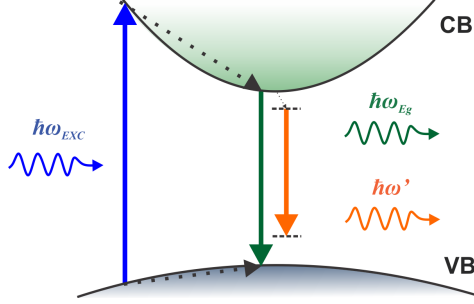


Figure 3.11: Schematic of the photoluminescence mechanism. An electron-hole pair is generated by the absorption of an incident photon with energy $\hbar\omega_{EXC}$. The carriers thermalize respectively to the conduction band minimum (CBM) and the valence band maximum (VBM), where they recombine radiatively, emitting a photon with energy $\hbar\omega_{Eg}$. Other radiative recombination mechanisms, such as excitons and impurities, cause the emission of photons at different, usually lower, energy $\hbar\omega'$.

by two elementary charges, this quasiparticle is assumed to have wavefunction approximable to those of the hydrogen atom. The binding energy of the exciton is calculated, in the Wannier-Mott approach, as:

$$E_n = E_g - \frac{\mu e^4}{2\epsilon_r^2 \epsilon_0^2 \hbar^2 n^2} \quad (3.1)$$

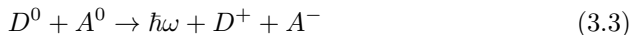
where μ is the reduced effective mass $\mu^{-1} = m_e^{-1} + m_h^{-1}$, ϵ_r is the dielectric constant, ϵ_0 is the permittivity of vacuum, and n is the energy level occupied by the electron. From the formula we understand that these energy levels are below the band gap E_g . Furthermore, the binding energies are in the order of 1-10meV. For instance, the free exciton in WZ InP has a binding energy of 6.4meV⁴⁸. Due to such low binding energy, most excitons are stable only at low temperature. With increasing temperature, in fact, the thermal energy of the phonons becomes sufficient to ionize the exciton. If the ionization rate is too high, the exciton will not be able to recombine radiatively anymore. The activation energy of this process can be measured from the temperature dependence of the integrated photoluminescence emission $I(T)$:

$$\frac{I(T)}{I_0} = \frac{1}{1 + C e^{-\frac{E_A}{k_B T}}} \quad (3.2)$$

where I_0 is the integrated PL emission at low temperature (in our case 10K), E_A is the activation energy of the ionization process, C is a constant.

At low temperature, carriers are frozen on impurities, leading to free-to-bound and donor-acceptor pair recombinations. In the free-to-bound transition electrons in the conduction band recombine with holes in acceptors, where the emitted photon energy will be $E_g - E_A$.

Often a semiconductor may contain both donors (D) and acceptors (A). The photogenerated carriers can therefore be trapped at the D^+ and A^- sites to produce neutral D^0 and A^0 centers. To return to equilibrium, electrons in D^0 sites might recombine radiatively with holes in A^0 sites, yielding a donor-acceptor pair (DAP) transition. It can be represented by the reaction



The energy of the emitted photon will therefore depend on the binding energy of the donor (E_D) and the acceptor (E_A), and on the Coulomb interaction between the ionized donor and acceptor. The energy of the transition will therefore be

$$\hbar\omega = E_g - E_A - E_D + \frac{e^2}{4\pi\epsilon_0\epsilon_r R} \quad (3.4)$$

where R is the distance between donor and acceptor participating in the transition. The energy is increased by the Coulomb interaction because the energy of the final, ionized state is lowered by the interaction itself. It is clear that as such sites are distributed in host lattice, the distance R will depend on the donor-acceptor pair actually involved. Therefore, further away pairs will have a lower energy.

The time taken by an electron-hole pair to recombine is also an important quantity to determine the nature of the transition. When a finite number of photons (e.g. a laser pulse) is absorbed, it excites a finite number of electron hole pairs, which start recombining, both radiatively and non-radiatively through competitive channels. The total decay rate of the photoexcited population is therefore

$$R_{Decay} = \frac{1}{\tau_{tot}} = \frac{1}{\tau_r} + \frac{1}{\tau_{nr}} \quad (3.5)$$

where $1/\tau_r$ and $1/\tau_{nr}$ are, respectively the radiative and nonradiative recombination rates. Intuitively, direct allowed transitions will have a large radiative recombination rate and therefore short carrier lifetime τ_r , while the opposite will happen for indirect and/or forbidden transitions. For a DAP transition, the radiative rate depends on the overlap of the carrier wavefunctions, therefore it can be written as⁴⁷

$$\frac{1}{\tau_{DA}} \propto \exp(-2R/a_{DA}) \quad (3.6)$$

where R is again the distance between donor and acceptor and a_{DA} is the larger Bohr radius between donor and acceptor.

3.5.1 Experimental setup

The setup used can be roughly divided into three sections: sources, optical line and detection. The sources available are three:

- Pulsed-wave 420nm laser diode, 1-80 MHz repetition rate. Circular excitation spot with diameter $1\mu\text{m}$.
- Pulsed-wave frequency-doubles Titanium-Sapphire (Ti-Sa) 405nm laser, 80 MHz repetition rate
- Wavelength-tunable source, constituted by a plasma-injected white lamp emitting between 400-800nm, coupled with a 0.30m spectrometer equipped with 1200g/mm grating (500nm blazing angle). Coupled in a $300\mu\text{m}$ multi-mode fiber, resulting into a circular excitation spot with diameter $10\mu\text{m}$.

Pulsed sources are used as they enable carrier lifetime measurements. Also, through a reduced duty cycle, they allow the system to cool down between pulses, avoiding heating effects which can affect the results.

Mirrors and optical fibers are used to steer the beam, while neutral density filters and polarizers are used to manipulate respectively its intensity and polarization. A Nikon 50X CR objective (NA=0.7) objective, mounted on an XYZ piezoelectric stage, is positioned in front of the sample in backscattering configuration to perform micro-photoluminescence (μPL). The samples are placed in an Oxford Instruments MicrostatHiRes2 cryostat to tune the temperature in the range 4-300K. The signal from the sample is analyzed using a 0.30m spectrometer equipped with 300 g/mm, 1200 g/mm and holographic 2400 g/mm gratings (500nm blazing angle), with a PIXIS charge coupled device (CCD) detector and a time correlated avalanche photodiode (APD) detector (130ps resolution). For time-resolved photoluminescence measurements, a Picoharp 300 time-correlated single photon counting (TCSPC) system, connected to both the pulsed-wave 420nm laser and the APD. Laser pulse generation and photon detection are therefore time-correlated and the intensity of the photoluminescence emission can be followed in time by repeating the experiment at high frequency and integrating the results. The intensity decays exponentially in time and the characteristic lifetime of the transition can be extracted.

3.5.2 Photoluminescence excitation spectroscopy

In photoluminescence excitation spectroscopy (PLE), a single wavelength of the photoluminescence emission is selected, then its intensity is recorded as a function

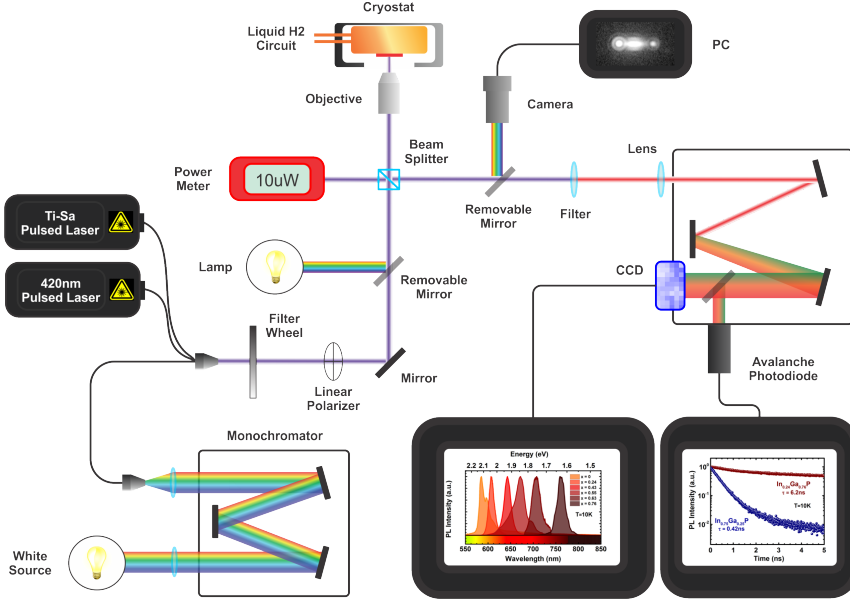


Figure 3.12: Schematic of the photoluminescence setup used in this work. Steady-state and time-resolved photoluminescence can be performed, in a range of temperature between 4-300K. Photoluminescence excitation spectroscopy is possible using the tunable source constituted by a white lamp and a monochromator.

of the excitation photon energy. In certain conditions, the PLE can be assumed as roughly equivalent to the absorption spectrum. We can write the relation between the PLE intensity I_{PLE} and the excitation intensity I_{EXC} as

$$I_{PLE} = P_{abs}P_{rel}P_{em}I_{EXC} \quad (3.7)$$

where P_{abs} is the probability of photon absorption by the probed material, P_{rel} is the probability of relaxation to the radiative state, P_{em} is the probability of radiative recombination after relaxation. P_{em} can be considered as constant during a PLE experiment as the radiative rate itself doesn't depend on the excitation, while P_{rel} depends strongly on the electron-hole pair energies. However, if the studied material possesses high crystal quality and low impurity levels, the probability of non-radiative recombination can be assumed as negligible compared to relaxation by electron-phonon interaction. In this case, P_{rel} can be considered as unity, and I_{PLE} as proportional to P_{abs} . Therefore we can rewrite I_{PLE} as⁴⁷

$$I_{PLE} \propto (E - E_0)^A I_{EXC} \quad (3.8)$$

where $A = 1/2$ for direct semiconductors and $A = 2$ for indirect semiconductors.

Chapter 4

Pseudo-direct to direct compositional crossover in wurtzite GaP/InGaP core-shell nanowires

A new degree of freedom in band structure engineering has become available in the form of crystal phase tuning in semiconductor nanowires, allowing the control of the material polytype^{2;49}. Crystal phase engineering thus unlocks new optical and electronic properties while maintaining compatibility with well-established mainstream semiconductor technology. This provides a promising method to surpass the conventional limits of commonly used semiconductors^{3;25}. Various nanowire growth mechanisms enable the formation of unusual crystal phases which are not accessible in bulk, such as Wurtzite (WZ) in III-Phosphides⁵, and by exploiting 3D epitaxial overgrowth such crystal phase can be transferred from the core to its surrounding shell⁵⁰. Wurtzite nanowires are very promising candidates for solid state lighting²⁹, photovoltaics⁵¹ and solar hydrogen conversion⁷. Recently it has also been shown that Wurtzite III-Phosphides might enable direct band gap green emitters, opening a possible way to "bridge the green gap"⁵. WZ GaP and WZ InP have been studied, both theoretically²⁶ and experimentally^{46;45}, and their optical properties are known. Both materials have a Γ_{9V}

⁰Contributions to this work: Dr. M.A. Verheijen (Philips Innovation Services) performed the TEM analysis, M. Albani and Prof. L. Miglio (Università Milano-Bicocca) performed the FEM simulations, Dr. A. Belabbes (KAUST) and Prof. F. Bechstedt (University of Jena) performed the DFT calculations.

highest valence band but, importantly, the first two conduction bands have a different order: the lowest conduction band in WZ GaP has Γ_{8C} symmetry, followed by a Γ_{7C} band at higher energy. In WZ InP this situation is reversed and Γ_{7C} is the lowest band. This has a strong influence on the optical properties of the materials as the $\Gamma_{8C} - \Gamma_{9V}$ transition is forbidden, while the $\Gamma_{7C} - \Gamma_{9V}$ is instead allowed with a large oscillator strength, as in WZ GaAs⁵² and WZ InP²⁹. By tuning the $\text{In}_x\text{Ga}_{1-x}\text{P}$ composition a crossover at the Γ point is expected, where the Γ_{8C} (lowest for Ga-rich) will be crossed by the Γ_{7C} band for increasing In concentrations. Such a Γ -crossing has not been observed so far for III-V semiconductors through compositional tuning. Moreover, the electronic properties of the WZ $\text{In}_x\text{Ga}_{1-x}\text{P}$ alloy are still fully unexplored.

4.1 Core-shell nanowire growth

4.1.1 Wurtzite GaP core growth

The WZ GaP cores are grown with MOVPE technique in an Aixtron-CSS showerhead reactor. Prior to the growth, the substrates are cleaned with piranha solution. An in-situ annealing step at 615°C is performed at the start of the growth process. Heating the substrate allows the desorption of carbon-related impurities and an eventual native oxide. Organic impurities in particular are responsible for inducing the movement of the Au droplet along the surface, introducing a randomization of the final nanowire positions. The randomization of the position can also change dramatically the synergetic growth effect, changing the effective V/III ratio at every single droplet, disrupting the optimal growth conditions⁴³. The temperature is then lowered to 480°C to perform a short droplet filling step providing Trimethylgallium (TMGa) and a nucleation step to initiate the nanowire growth. The temperature is raised again to 615°C, at which the growth takes place. The (111)B oriented ZB GaP substrate is situated on a graphite susceptor kept under rotation to uniform the gas flow over the sample, as shown in Chapter 3. The precursors used were TMGa and Phosphine (PH_3), with the addition of HCl. HCl is used to: 1) enhance the diffusion of the group III adatoms through the formation of partially chlorinated species, allowing more material to reach the Au catalyst thus enhancing the growth rate⁵; 2) passivate the sidewalls of the nanowires to inhibit lateral growth⁵³; 3) etch excess material from the sidewalls to maintain atomically sharp surfaces^{5;54}. The final result is shown in Fig.4.1.

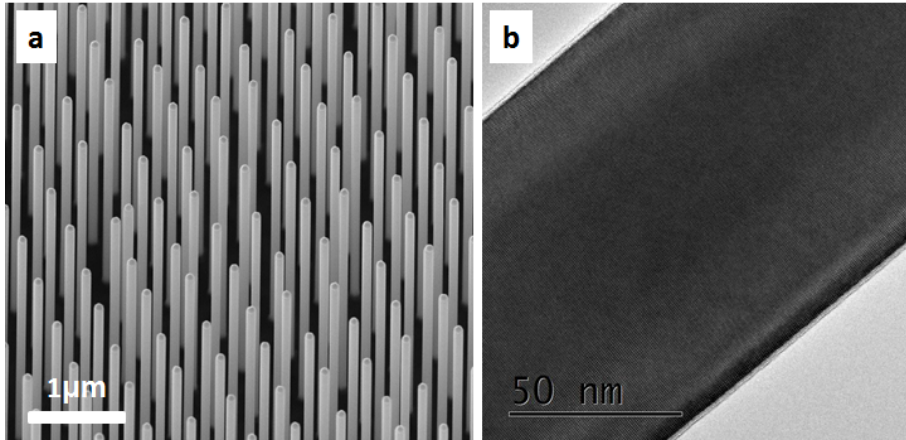


Figure 4.1: (a) SEM image of a WZ GaP nanowire array. The catalyst array was fabricated with nanoimprint lithography and the annealing temperature was 700°C , high enough to desorb carbon impurities, but low enough to prevent wandering of the Au droplet on the surface. (b) HR-STEM image of a WZ GaP nanowire in the $\langle 10\bar{1}0 \rangle$ zone axis. The uniformity of the contrast demonstrates defect-free morphology. A stacking fault would have been visible as a straight line perpendicular to the growth axis.

4.1.2 Catalyst Etching

The Au catalyst is etched *ex situ* after the core growth. Three solutions are used: H_3PO_4 to dissolve the native oxide, diluted King's Water ($\text{H}_2\text{SO}_4 + \text{HNO}_3$) and Iodine solution (KI/I_2). We used diluted King's water first as we speculate that a thin layer of GaP might form around the Au-Ga droplet during the cooldown after growth, which protects it from the Iodine solution. After this thin layer is dissolved, the Iodine solution etches the catalyst while leaving almost atomically smooth sidewalls as shown in Fig.4.2a-b. The subsequent epitaxy can therefore be performed without the introduction of defects due to the etching step. An insufficient etching time leads to the formation of smaller Au nanoparticles, which in turn diffuse along the sidewalls or form branches during the shell growth. An excessive etching time instead leads to severe roughness on the WZ GaP surface, shown in Fig.4.2c-d, which in turn yields an erratic shell growth with unpredictable effects, as shown in Fig.4.2e.

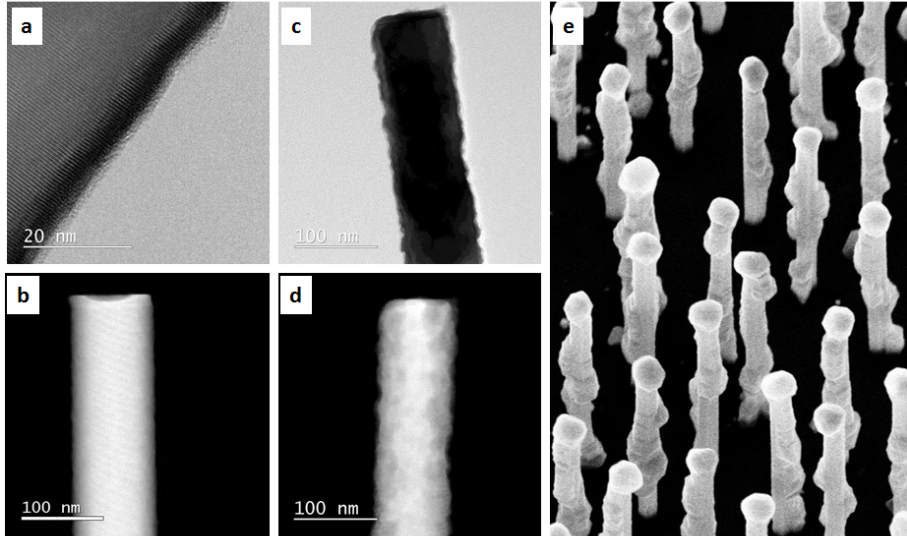


Figure 4.2: (a-b) STEM (a) and HAADF (b) images of a WZ GaP nanowire after catalyst wet etching. Sidewall roughness is present, but very limited. (c-d) TEM bright field (c) and HAADF (d) images of an overetched WZ GaP nanowire, showing evident sidewall roughness (e) SEM image of a growth attempt of InGaP shell on overetched WZ GaP wires. The resulting growth is heavily dishomogeneous and uncontrollable.

4.1.3 Wurtzite InGaP Shell Growth

The etched cores are used as a template for the shell growth at 585°C in the same reactor, using TMGa, PH_3 and Trimethylindium (TMIn) as Indium precursor with a very high V/III ratio (>1000 in our case) to promote layer growth. The concept schematic of the nanowire structure is presented in Fig.4.3a. A representative SEM image of the resulting WZ $\text{In}_x\text{Ga}_{1-x}\text{P}$ nanowires is shown in Fig.4.3b. The WZ GaP/ $\text{In}_{0.24}\text{Ga}_{0.76}\text{P}$ wires are uniform and may bend in random directions with an angle up to 10 degrees. $\text{In}_x\text{Ga}_{1-x}\text{P}$ in fact possesses a larger lattice parameter than GaP and we expect the shell to be compressively strained. Bending is due to possible asymmetrical defect density and/or composition in the shell and this phenomenon will be investigated in Chapter 6. In Fig.4.3c we show an HAADF image of a WZ GaP/ $\text{In}_{0.10}\text{Ga}_{0.90}\text{P}$ nanowire, from which we can notice a large grain, with ZB crystal symmetry, grown on the top facet of the nanowire itself. This phenomenon is known⁵⁵, as the $[0001]$ direction allows the growth of ZB, due to the possibility of adopting its typical ABC stacking. In the $\langle 10\bar{1}0 \rangle$ directions instead the epitaxially grown material must

adopt the ABAB stacking of WZ. Therefore the crystal structure transfer in this system can be achieved only in the radial direction, but not in the axial one.

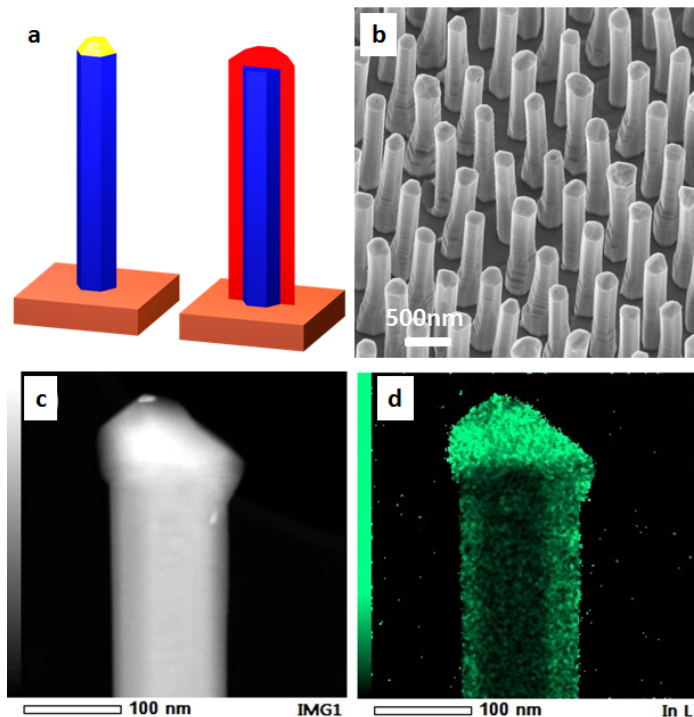


Figure 4.3: (a) Schematics of the nanowires in this work. Left: WZ GaP (blue) with the gold catalyst droplet (yellow). Right: WZ GaP/In_xGa_{1-x}P core-shell nanowire (In_xGa_{1-x}P in red, notice the absence of the catalyst). (b) SEM image of a representative WZ GaP/In_xGa_{1-x}P core-shell sample (in this case WZ GaP/In_{0.24}Ga_{0.76}P). The bending due to asymmetric strain is visible in some nanowires. (c-d) WZ GaP/In_{0.25}Ga_{0.75}P core-shell nanowire: (c) HAADF image. (d) EDS 2D map of Indium. The top ZB segment has a higher (In_{0.75}Ga_{0.25}P) Indium concentration than the WZ shell.

Hydrogen Chloride (HCl) is also used during the growth, in order to control the shell morphology. HCl has two important effects on the shell growth. Firstly, it etches material from the nanowire surfaces, preferentially etching Indium over Gallium: as we show in Fig.4.3d, we observed that the ZB domains are richer in Indium, and as such they are more effectively etched by HCl⁵⁶. As we demon-

strate in Fig.4.4a-b, the correct optimization of the HCl flow allows to eliminate almost completely the ZB segment on the top of the nanowire.

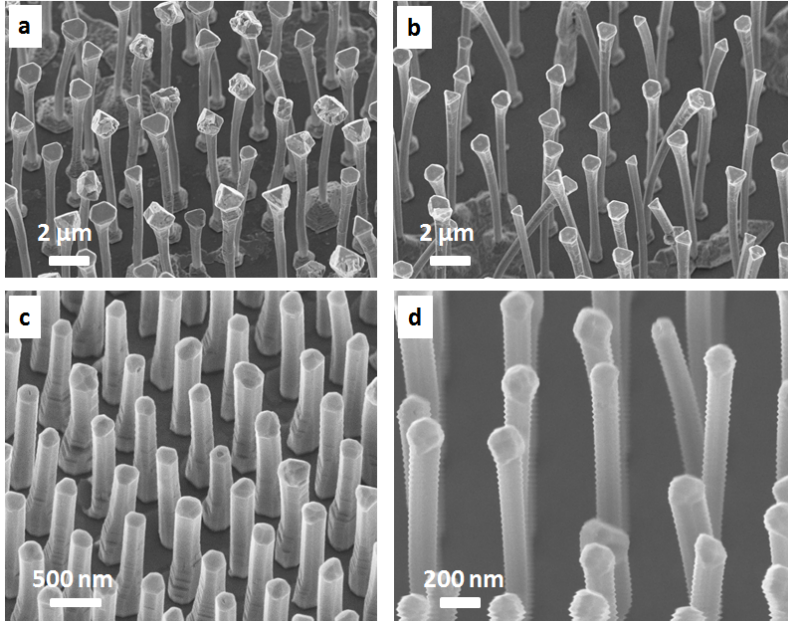


Figure 4.4: (a-b) WZ GaP/In_{0.60}Ga_{0.40}P core-shell nanowires grown with identical recipe, but different HCl flow. (a) Lower flow. (b) Optimized flow. Note the large ZB grains on top of the nanowires in (a), which are rare in (b). (c-d) WZ GaP/In_xGa_{1-x}P core-shell nanowires grown with same precursor flows. (c) was grown for 45m (same as Fig. 4.3) featuring passivation removal steps, reaching 80nm shell thickness, while (d) was grown for 60m, but without passivation removal steps, reaching only 10nm shell thickness. Core thickness was 100nm.

Secondly, HCl passivates the surface of III-Phosphides⁵³, leading to a progressive saturation of the surface by Chlorine, eventually stopping the growth and limiting the maximum thickness of the shell to about 20-40 nm. This surface passivation effect can be avoided by applying a growth process featuring two alternating steps: a 15 minutes long growth step as we described earlier, alternated by a 45s step to remove the passivation layer. The passivation removal step is performed with a lower HCl flow and a higher Gallium flow, providing no Indium. During this step, TMGa reacts with Chlorine at the nanowire sidewalls, producing GaCl₃ and thereby removing the passivation layer. Using this cyclic growth, an arbitrarily thick WZ In_xGa_{1-x}P shell can be grown. In Fig.4.4c-d we

show the effect of the cyclic growth protocol (c), which successfully avoids the passivation effect of HCl (d).

4.2 TEM analysis and strain simulations

The morphology and the crystal quality, i.e. the purity of the WZ phase and the absence of defects are analyzed with Transmission Electron Microscopy (TEM). For this study the overall structures need to be sufficiently transparent to the electron beam in order to allow high-resolution imaging and therefore a maximum diameter of about 140 nm is used with a 15nm shell thickness. As shown in Fig.4.5a, the $\text{In}_{0.23}\text{Ga}_{0.77}\text{P}$ shell shows a WZ crystal structure. Shells with low Indium content (up to $x = 0.10$) are defect-free, while the ones with higher Indium content show misfit dislocations (arrow in Fig.4.5a). The shell composition is determined by Energy-dispersive X-Ray Spectroscopy (EDS), as shown in Fig.4.5b-e. We used the EDS data to calibrate the precursor flows to obtain the desired average composition of each shell.

The experiment is performed in two different crystallographic orientations: in projection (Fig.4.5b) along the $\langle 11\bar{2}0 \rangle$ zone axis, and in cross-section (Fig.4.5c-e), with the nanowire cut perpendicularly to its main $[0001]$ axis as described in Chapter 3. Cross-sectional analysis is necessary to observe the surface faceting and to observe the inner structure of the shell. From the cross-sectional EDS analysis shown in Fig.4.5c-e we obtain an average Indium fraction of $x=0.24\pm 0.04$ for this sample. The facets of the WZ $\text{In}_x\text{Ga}_{1-x}\text{P}$ shells belong to two different families: $\{1\bar{1}00\}$ parallel to the core facets and $\{11\bar{2}0\}$. The number of facets increases with shell thickness as it is possible that the $\{11\bar{2}0\}$ facets in WZ $\text{In}_x\text{Ga}_{1-x}\text{P}$ are low energy facets which appear to minimize the total surface energy. Also, the substitution of the corner between $\{1\bar{1}00\}$ facets with a $\{11\bar{2}0\}$ facet likely helps to minimize the energy. A 2-5nm thin shell with lower Indium concentration (5-10%) can also be observed in Fig.4.5d in between two WZ $\text{In}_x\text{Ga}_{1-x}\text{P}$ shells with higher Indium content, resulting from the layer growth during the chlorine removal step after growing the first $\text{In}_x\text{Ga}_{1-x}\text{P}$ shell. Regions with lower Indium concentration are visible along the rods radially extending from the corners of the hexagonal core, a phenomenon also observed in previous work on core-shell nanowires. We studied one of these "sunburst segregations" more in detail and we present the results in Fig.4.6. The structure shows a sensibly lower Indium concentration of about 10% and a thickness of less than 10nm. We judge these structures as substantially negligible concerning the interpretation of the optical properties, as they are much smaller in volume than the entire shell and possess a higher band gap.

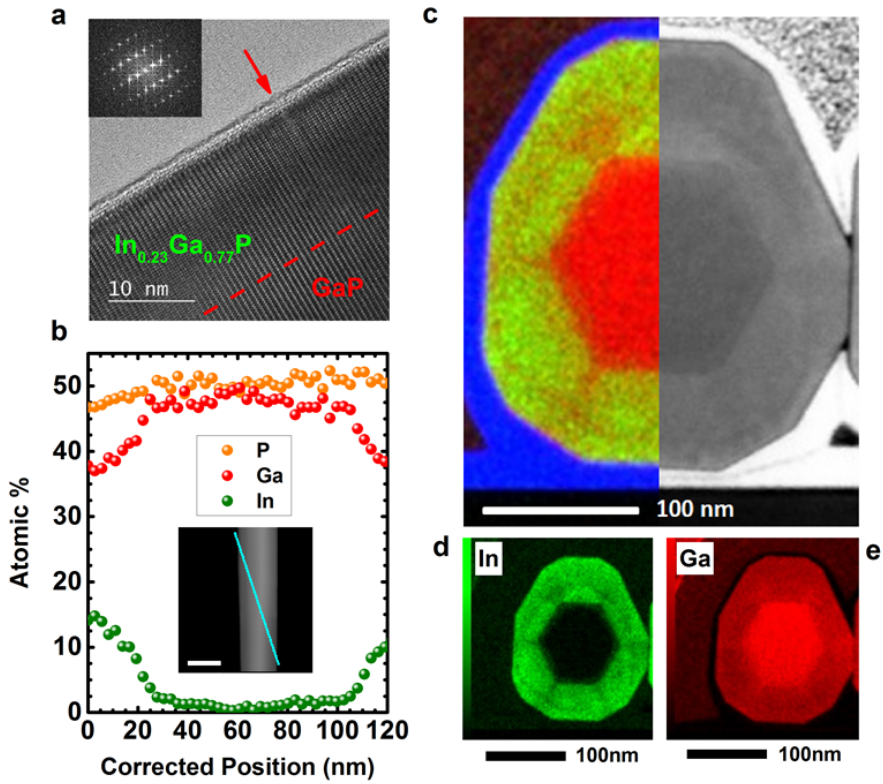


Figure 4.5: (a) TEM image of a WZ GaP/ $\text{In}_{0.23}\text{Ga}_{0.77}\text{P}$ core-shell nanowire, showing a missing crystal plane in the 15nm thick shell (indicated by the arrow). Inset: Fast Fourier Transform of the shown image, showing the $[2-1-10]$ zone as pattern of the wurtzite crystal structure. (b) EDS compositional line profile of the same nanowire in (a), showing the shell composition, with some limited asymmetry. Inset: HAADF image to show the executed line scan (scalebar: 100nm). The length scale of the EDX line profile has been converted to a radial profile. A slight shell thickness dishomogeneity ($\approx 10\text{nm}$) is also visible. (c) 2D EDS mapping (left) and HAADF-STEM image (right) of a WZ GaP/ $\text{In}_{0.24}\text{Ga}_{0.76}\text{P}$ core shell nanowire in cross section (blue: Cobalt). The core facets and the 6 shell facets parallel to them belong to the $\langle 10\bar{1}0 \rangle$ family. The other 6 shell facets belong to the $\langle 11\bar{2}0 \rangle$ family. (d-e) Quantified EDS element maps of the same lamella for Indium (d) and Gallium (e).

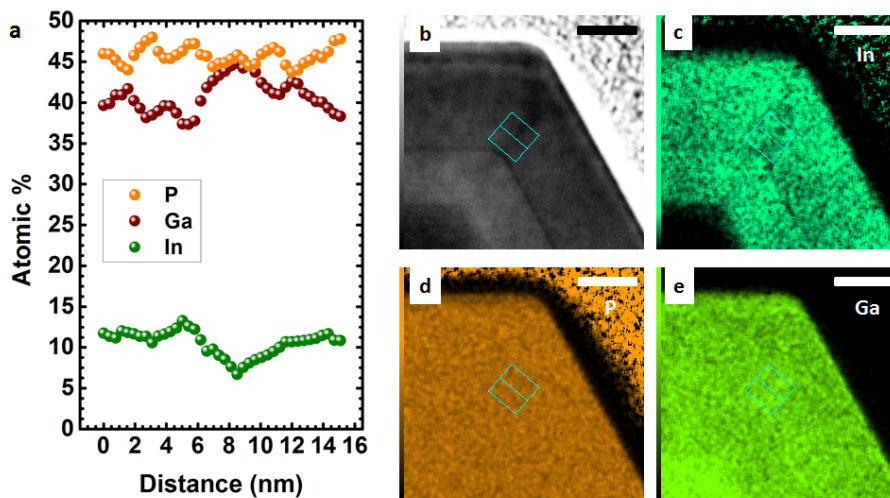


Figure 4.6: WZ GaP/In_{0.24}Ga_{0.76}P core-shell nanowire. (a) EDS line scan plot of the cross section of the nanowire. (b) Bright field TEM image. (c-e) EDS 2D maps of (c) Indium (d) Phosphorous and (e) Gallium. The light blue box describes the study area, integrated as a line scan and plotted in (a).

In order to evaluate the strain magnitude and distribution within the core/shell system, Finite Element Method (FEM) simulations of hydrostatic strain have been performed for a WZ GaP/In_xGa_{1-x}P core-shell nanowire geometry with a core apothem and shell thickness both of 50nm and for a corresponding planar geometry. The simulations have been performed by M. Albani and Prof. L. Miglio (Universita' Milano-Bicocca). The results are displayed in Fig.4.7. A six-fold symmetry is clearly present, with six pockets at lower strain in the shell caused by the geometric relaxation induced by the six corners, in agreement with previous studies. This phenomenon results in a much lower average hydrostatic strain (less than one third) than expected for a corresponding planar heterostructure with identical lattice mismatch as reported in Table 4.1. This means that the nanowire geometry allows for very efficient strain relaxation, probably delaying the onset of plastic relaxation to shell thickness three times larger than the critical thickness in a planar film. These strain effects have been taken into account for the analysis of the photoluminescence.

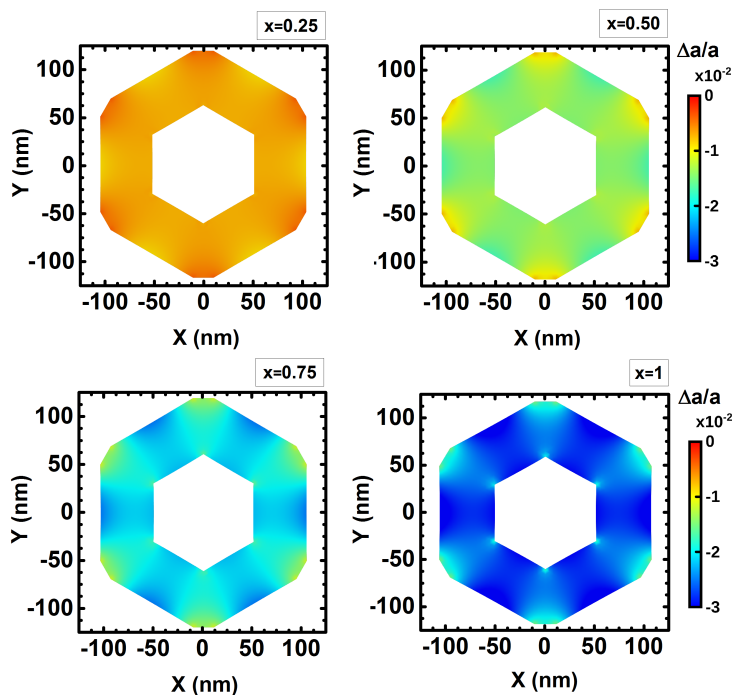


Figure 4.7: FEM simulations for the shell in WZ GaP/In_xGa_{1-x}P core-shell nanowires for $x=0.25, 0.50, 0.75$ and 1 . The six-fold symmetry of the strain relaxation is clearly visible, due to the larger free surface at the corners, which allows an easier bi-dimensional relaxation.

Indium fraction x	Average hydrostatic strain	Strain expected in planar layer	Strain range [min, max]
0.25	-0.7%	-2.7%	[-0.5, -0.8]%
0.50	-1.4%	-5.1%	[-1.0, -1.6]%
0.75	-2.0%	-7.3%	[-1.5, -2.3]%
1	-2.6%	-9.2%	[-2.0, -3.0]%

Table 4.1: FEM calculated strain in the shell of WZ GaP/In_xGa_{1-x}P core-shell nanowires, compared to the expected strain in a corresponding planar heterostructure. The strong relaxation given by the three-dimensional nature of nanowires allows to reduce the average hydrostatic strain by about 60% of the total.

4.3 Low temperature photoluminescence

4.3.1 Steady-state PL

The optical properties of the WZ GaP/In_xGa_{1-x}P core-shell nanowires are investigated by photoluminescence (PL) measurements as a function of the Indium concentration. We directly correlate the emitted PL wavelength with Indium composition by transferring nanowires onto a TEM grid and performing PL first and then EDS studies on the same nanowires. With this method we can avoid difficulties arising from wire-to-wire variations. The emission wavelength of WZ In_xGa_{1-x}P shifts from 590nm (2.1eV) to 760nm (1.6eV) by increasing x from $x = 0$ to $x = 0.76$ as shown in Fig.4.8.

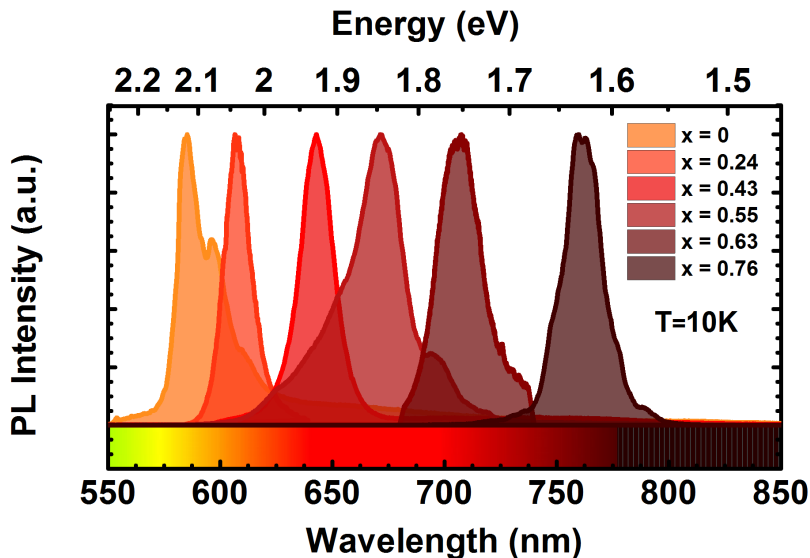


Figure 4.8: Photoluminescence spectra at 10K of various WZ GaP/In_xGa_{1-x}P core shell nanowires, emitting in different spectral regions. Excitation power density: 3kW/cm².

The emission of the WZ In_xGa_{1-x}P shells is polarized perpendicular to the growth c-axis (as shown in Fig.4.9) demonstrating that the emission originates from the WZ crystal structure. The degree of polarization of the photoluminescence emission of the WZ GaP/In_xGa_{1-x}P nanowires was calculated using the following formula:

$$P = \frac{I_\pi - I_\sigma}{I_\pi + I_\sigma} \quad (4.1)$$

where I_π and I_σ are respectively the integrated photoluminescence intensities of the polarizations perpendicular and parallel to the axis of the nanowire (wurtzite c-axis). We obtain a polarization degree for two different nanowires of 80% in Fig.4.9a and 55% in Fig.4.9b. However, as both the $\Gamma_{8C} - \Gamma_{9V}$ and $\Gamma_{7C} - \Gamma_{9V}$ optical transitions of WZ $\text{In}_x\text{Ga}_{1-x}\text{P}$ are expected to emit with polarization perpendicular to the nanowire, the polarization selection rules do not allow to discriminate between these two bands.

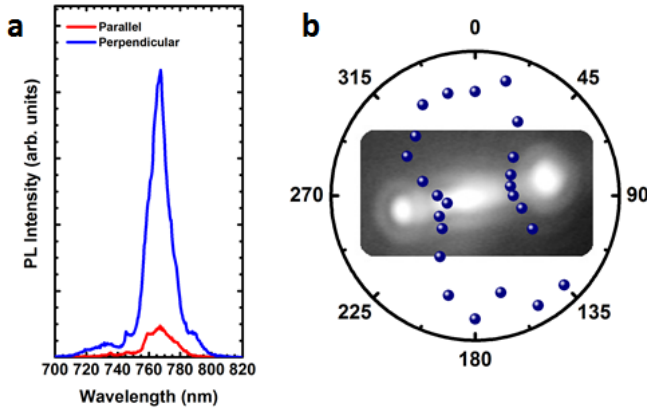


Figure 4.9: Left: photoluminescence spectra of WZ $\text{GaP}/\text{In}_{0.80}\text{Ga}_{0.20}\text{P}$ core-shell nanowire at 10K. The signal was filtered by a polarized, rotated perpendicular or parallel to the emitting nanowire. The degree of polarization is 80%.

Right: radial plot of PL intensity as a function of signal polarization, superimposed on a panchromatic image of an emitting WZ $\text{GaP}/\text{In}_{0.63}\text{Ga}_{0.37}\text{P}$ nanowire. The perpendicular polarization confirms WZ emission.

In PL spectra taken at lower excitation power density, sharp emission lines are present, located below the average emission of the shell. We attribute these features to the carrier localization at low temperature in pockets of material with slightly higher (1-2%) Indium concentration, due to alloy composition fluctuations. We tend to exclude the presence of actual quantum dots, as we find no evidence of quantum confinement: in cases reported in literature, in fact, such lines are present above the overall energy of emission of the nanowire, while in this case they are at slightly lower energy than the overall shell emission, hinting to simple localization effects. In Fig.4.10 we show a photoluminescence power

series of a single WZ GaP/In_xGa_{1-x}P nanowire: localization effects are present at low excitation power, while at higher power a more intense peak emerges, which corresponds to the average emission of the shell. The integrated PL intensity as a function of the excitation power follows a linear behavior with slope $S = 0.90 \pm 0.1$, indicating a prevalent radiative recombination. The slope $S < 1$ however suggests a possible impurity recombination such as donor-acceptor pairs (DAP) or defectivity in the sample. As we know from TEM analysis that the samples contain dislocations, the latter explanation is a more likely possibility. However, for the purpose of this work, the eventual presence of DAP recombination does not prejudice the conclusions, as will be demonstrated later.

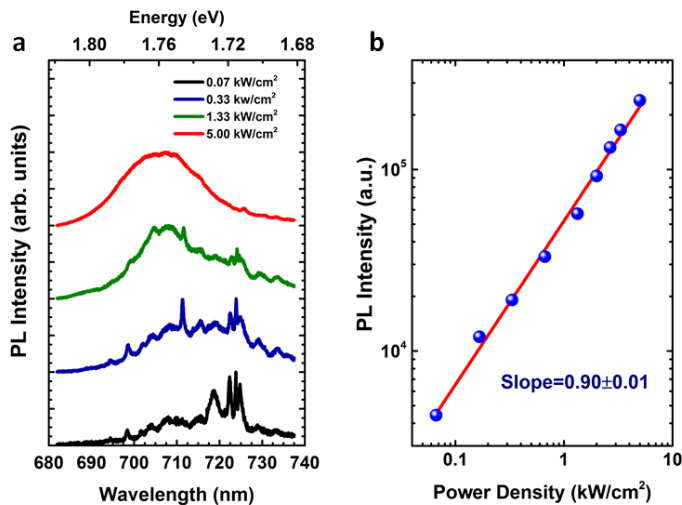


Figure 4.10: (a) Photoluminescence power series of a WZ GaP/In_{0.65}Ga_{0.35}P showing carrier localization at low power, leading to a more intense emission at higher energy, corresponding to the average emission of the shell. (b) Integrated PL intensity as a function of the excitation power. The slope $\alpha = 0.90$ indicated a prevalent radiative recombination.

4.3.2 Time-resolved photoluminescence

In order to identify the bands involved in the emission and to find the $\Gamma_{8C} - \Gamma_{7C}$ crossover point as a function of the Indium composition, time-resolved PL (TRPL) measurements are performed at 10K, using the experimental setup described in Chapter 3. Two representative TRPL measurements are shown in Fig.4.11a from samples with $x=0.24$ and $x=0.75$ (WZ In_xGa_{1-x}P) with lifetimes of 6.2ns and 0.4ns, respectively, obtained by fitting the curve with a single expo-

ponential decay. Measurements performed over a wide compositional range at 10K and averaged over several nanowires show that the emission from WZ $\text{In}_x\text{Ga}_{1-x}\text{P}$ shells with $x \leq 0.25$ features lifetime well above 1ns, while shells with higher Indium composition show a lifetime well below 1ns, as reported in Fig.4.11b. A significant and reproducible difference in lifetime is observed between samples with $x \leq 0.25$ and $x \geq 0.38$. Since a small (large) oscillator strength, and thus a long (short) lifetime, is expected for the pseudo-direct $\Gamma_{8C} - \Gamma_{9V}$ (direct $\Gamma_{7C} - \Gamma_{9V}$) transition, this provides a first signature of the Γ_{8C}/Γ_{7C} crossover. However, these data are not conclusive as the decrease in lifetime could also be attributed to other decay mechanisms, for instance induced by defects, which are indeed present in the shells. Therefore, more evidence is needed to conclude on the conduction band crossover.

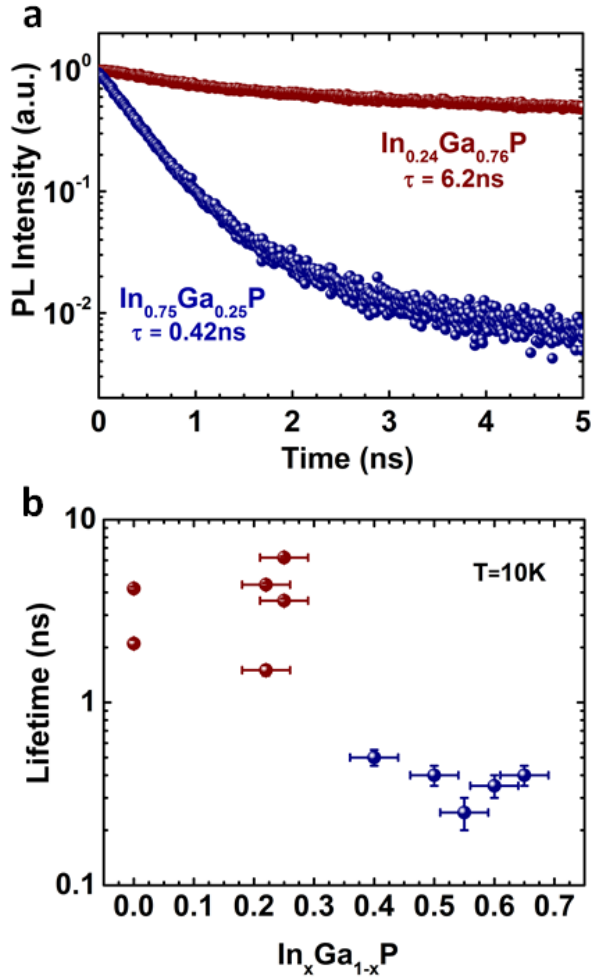


Figure 4.11: (a) Time-resolved photoluminescence measurements of two nanowires with different composition, showing an order of magnitude of difference in lifetime. Excitation power density: $0.2\text{kW}/\text{cm}^2$.

(b) Photoluminescence lifetime as a function of Indium fraction: for $x \leq 0.28 \pm 0.04$, the emission shows a lifetime well above 1ns, while for $x \geq 0.45 \pm 0.04$ the lifetime is one order of magnitude shorter. Excitation power density: $0.1\text{ kW}/\text{cm}^2$. All measurements are performed at 10K on single wires transferred on SiO_2 .

4.3.3 Temperature dependent photoluminescence

From temperature-dependent PL measurements we can further study the Γ_{8C}/Γ_{7C} crossover point. The integrated PL emission intensities as a function of temperature for WZ $\text{In}_{0.24}\text{Ga}_{0.76}\text{P}$ and WZ $\text{In}_{0.63}\text{Ga}_{0.37}\text{P}$ are shown in Fig.4.12a. The ratio between the integrated emission at 300K (I_{300K}) and 4K (I_{4K}) differs by more than two orders of magnitude between the two samples. As a side note, in WZ $\text{In}_{0.63}\text{Ga}_{0.37}\text{P}$ the increase of the integrated PL intensity above 58K, corresponding to a thermal energy of 4meV, is attributed to carrier detrapping from defects such as impurities and dislocations. The values for the I_{300K}/I_{10K} ratio as a function of the Indium content are shown in Fig.4.12b. Below $x=0.25$ values of about 0.01% are obtained, while above $x=0.38$ the ratio steeply rises by three orders of magnitude, reaching a maximum of 18%. Since the $\Gamma_{8C} - \Gamma_{9V}$ transition is only weakly allowed, in WZ $\text{In}_x\text{Ga}_{1-x}\text{P}$ with low Indium content the carrier recombination is mostly non-radiative, causing the low I_{300K}/I_{10K} ratio. In WZ $\text{In}_x\text{Ga}_{1-x}\text{P}$ with $x \geq 0.38$ instead the high oscillator strength of the $\Gamma_{7C} - \Gamma_{9V}$ transition provides with high band to band transition intensity up to 300K, leading to a high I_{300K}/I_{10K} ratio. This therefore substantiates the Γ_{8C}/Γ_{7C} crossover at an Indium fraction in the range $0.25 < x < 0.38$. This steep increase in I_{300K}/I_{10K} ratio in the range $0.25 < x < 0.38$ is directly correlated with the large decrease of the PL lifetime shown in Fig.4.11b. This result cannot be explained by the emergence of non-radiative recombination channels, such as surface states or increased defect density, since such channels would also shorten the lifetime, but at the same time lower the I_{300K}/I_{10K} ratio. On the other hand, an increase in I_{300K}/I_{10K} ratio cannot be explained by a possible decrease of surface states with increasing Indium fraction, as this would also have the effect of increasing the lifetime, not shortening it as we see. We therefore conclude that the explanation for these observation should be a change in the nature of the band gap transition from direct-forbidden to direct-allowed, which explains the increase in I_{300K}/I_{10K} ratio and the shortening of the lifetime. We identify this phenomenon as the Γ_{8C}/Γ_{7C} crossover for WZ $\text{In}_x\text{Ga}_{1-x}\text{P}$ in the composition range $0.25 < x < 0.38$.

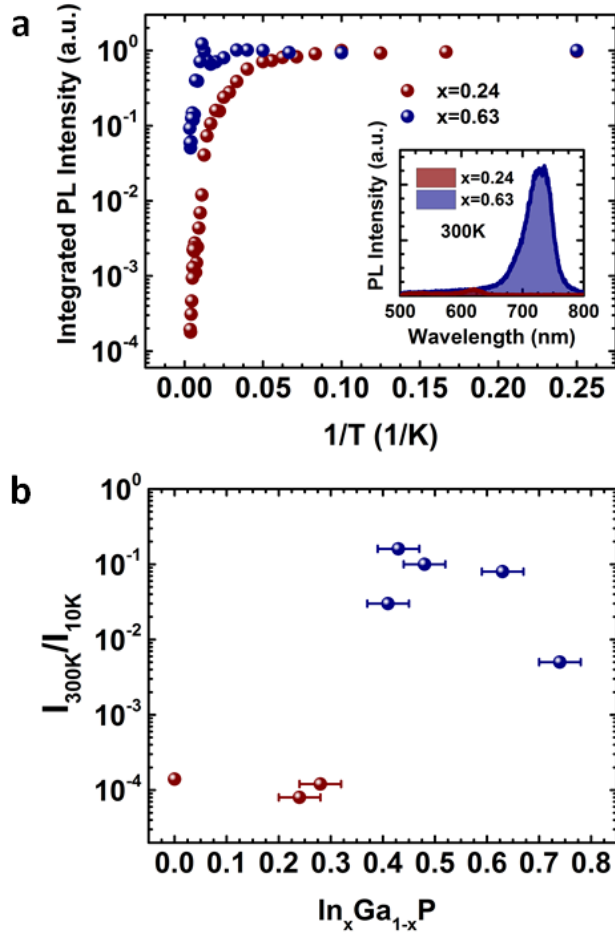


Figure 4.12: (a) Integrated PL intensity as a function of the inverse of temperature for WZ GaP/In_{0.24}Ga_{0.76}P and WZ GaP/In_{0.63}Ga_{0.37}P core-shell nanowires. In WZ In_{0.63}Ga_{0.37}P the increase of the integrated PL intensity above 58K, corresponding to a thermal energy of 4meV, is attributed to carrier detrapping from defects such as impurities and dislocations. Inset: comparison of the spectra at 300K, showing much stronger emission by the WZ GaP/In_{0.63}Ga_{0.37}P nanowire.

(b) I_{300K}/I_{10K} ratio as a function of Indium fraction x . All samples with $x \leq 0.28 \pm 0.05$ showed a ratio around 10^{-4} , while for $x \geq 0.41 \pm 0.04$ the ratio strongly increases, up to 0.18.

4.4 WZ InGaP band structure

In order to correlate the photoluminescence of our nanowires with the composition, we performed a PL study on a TEM carbon mesh grid, to be able to directly correlate the emission location in the nanowire with EDS data. Fig.4.13 shows a camera image with the relative measured PL spectrum and an HAADF image of the same wire, with highlighted the emitting area where the EDS scan and quantification were performed. In all studies, PL was performed prior to the TEM studies, in order to avoid possible changes in PL by electron beam irradiation effects.

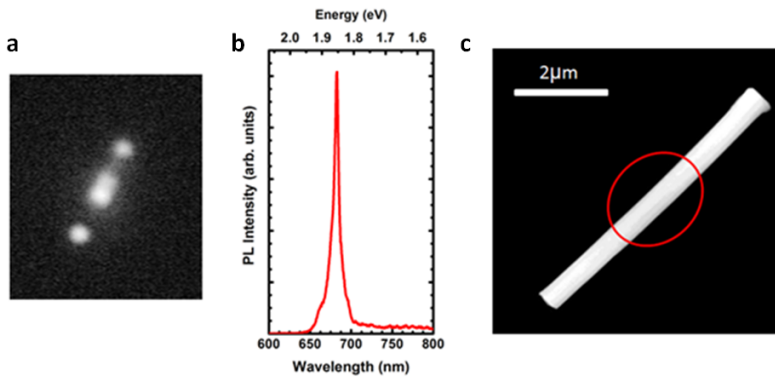


Figure 4.13: (a) Panchromatic image of an emitting WZ GaP/In_{0.45}Ga_{0.55}P core-shell nanowire. (b) PL spectrum of the nanowire at 10K. (c) HAADF image of the nanowire, with circled in red the emitting region during the experiment (as observable in the panchromatic image).

The inaccuracy in the compositional results is caused by two main factors: firstly, thickness of the wires which causes X-ray reabsorption, and secondly compositional and thickness inhomogeneities of the shells. Small (<100nm) areas of compositional inhomogeneities cannot be recognized in the side view studies and can thus not be corrected for. We therefore attribute a $\pm 4\%$ of uncertainty on the EDS quantification of the composition of WZ In_xGa_{1-x}P, as we estimate it as sufficient to take into account all the experimental uncertainties. To take into account carrier localization during the PL measurement, we always used the highest value of Indium concentration obtained in every EDS measurement of a wire. Carriers in fact tend to migrate and recombine in the regions with lowest band gap, which correspond to the highest Indium concentration. An additional factor that affects the PL-TEM correlation is strain which may still be present in non-relaxed portions of the wire: this aspect will be taken into account at a

later stage. In order to obtain a calibration function for our photoluminescence data, we fitted the data obtained from the PL-TEM correlation procedure using a parabolic fit as shown in Fig.4.14:

$$E_{g,InGaP} = x \cdot E_{g,InP} + (1 - x) \cdot E_{g,GaP} - bx(1 - x) \quad (4.2)$$

obtaining for the $\Gamma_{7C} - \Gamma_{9V}$ a bowing parameter $b = 0.7 \pm 0.1$ eV, an acceptable value for a III-V semiconductor. The $\Gamma_{8C} - \Gamma_{9V}$ data were fitted linearly as the bowing is expected to be very low and not observable from our data. The crossover point was calculated from the intersection of these two curves, at about $x=0.43$. With this method, we are therefore able to attribute a composition to the PL emission of WZ $In_xGa_{1-x}P$, and the resulting fitting functions are our proposed empirical functions for the transitions energies of WZ $In_xGa_{1-x}P$. In the following paragraphs, we will instead compare our experimental data with theoretical calculations.

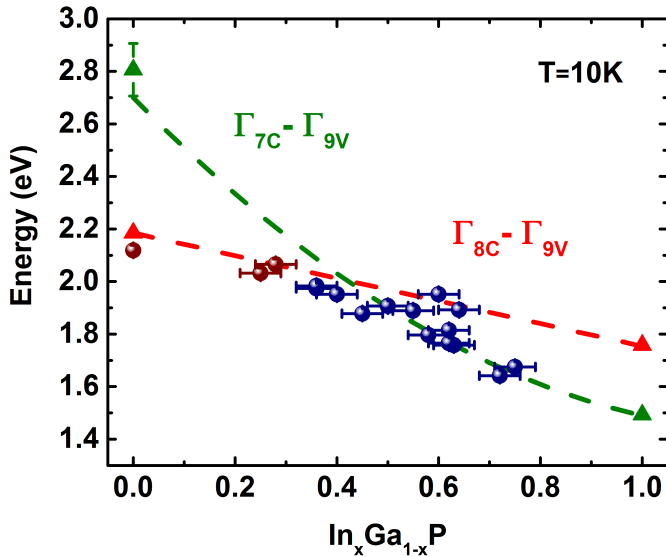


Figure 4.14: Measured emission energy as a function of Indium fraction. Triangles: data from literature. Red dashed line: $\Gamma_{8C} - \Gamma_{9V}$ transition connecting the literature data. Green dashed line: $\Gamma_{7C} - \Gamma_{9V}$ transition. A parabolic fit is performed for the $\Gamma_{7C} - \Gamma_{9V}$ data, obtaining a bowing parameter $b=0.7\pm 0.1$. The $\Gamma_{8C} - \Gamma_{7C}$ crossover is estimated to lie at $x=0.42$.

In order to provide a deeper understanding of the observed transitions, the

band structure of WZ $\text{In}_x\text{Ga}_{1-x}\text{P}$ is calculated for different compositions. The calculations have been performed by Dr. A. Belabbes (KAUST) and Prof. F. Bechstedt (University of Jena), using total-energy calculations in the framework of the density functional theory with the exchange-correlation functional in local density approximation (LDA)⁵⁷ as implemented in the Vienna ab initio simulation package (VASP)⁵⁸. Quasiparticle corrections to account for the excitation aspect are considered in the framework of the LDA-1/2 method²⁶. The results are shown in Fig.4.15 together with the parabolic fit of the optical transition energies (solid and dotted lines), to facilitate the comparison with the experimental data. The band alignment of WZ $\text{In}_x\text{Ga}_{1-x}\text{P}$ with WZ GaP has also been calculated and found to be Type I for $x < 0.75$. As all our WZ $\text{In}_x\text{Ga}_{1-x}\text{P}$ samples have $x \leq 0.75$, we conclude that all observed photoluminescence can be safely attributed to recombination in WZ $\text{In}_x\text{Ga}_{1-x}\text{P}$, as the carriers will be confined in the shell.

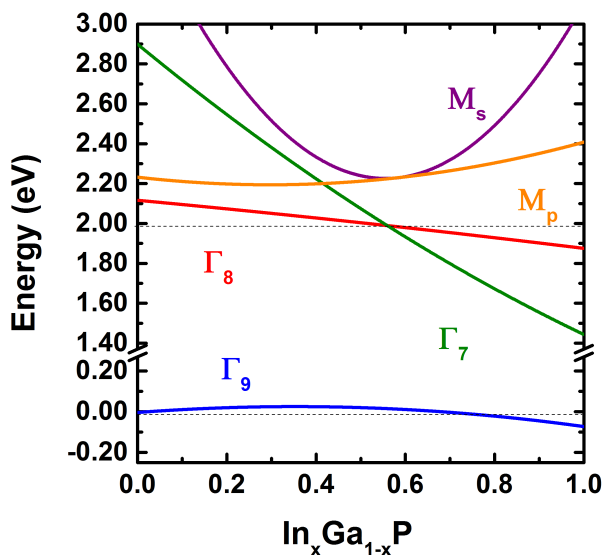


Figure 4.15: Calculated band structure of WZ $\text{In}_x\text{Ga}_{1-x}\text{P}$. The top valence band energy varies by a small amount with composition. The dashed line indicates the valence band maximum for WZ GaP, indicating the band alignment with Wz InGaP, which is Type I for $x < 0.75$, and a shallow Type II for $x > 0.75$.

To complete our understanding, we now plot the obtained emission wavelengths as a function of the WZ $\text{In}_x\text{Ga}_{1-x}\text{P}$ composition in Fig.4.14, obtained by correlation of PL measurements and EDS analysis on the same wires. In ad-

dition, we plot the energy values for the $\Gamma_{7C} - \Gamma_{9V}$ transition in WZ GaP and $\Gamma_{8C} - \Gamma_{9V}$, $\Gamma_{7C} - \Gamma_{9V}$ transitions in WZ InP available in literature (triangles in Fig. 4.16)^{46;45}. As the emission in WZ GaP is impurity-related⁴⁶, we report both the emission in this work and the band position from literature. Although we note a discrepancy between experimental and calculated data, the results validate our assignment of the PL emission to the $\Gamma_{8C} - \Gamma_{9V}$ transition for Indium-poor WZ $\text{In}_x\text{Ga}_{1-x}\text{P}$ and to the $\Gamma_{7C} - \Gamma_{9V}$ transition for Indium-rich WZ $\text{In}_x\text{Ga}_{1-x}\text{P}$. This discrepancy is reasonable, considering the predictive power of the quasiparticle calculations within an accuracy of $\pm 0.1\text{eV}$. In addition, we should consider alloy disorder and carrier localization effects during the PL measurements, which will result in a lower emission energy, contributing to this discrepancy. From these calculations it is clear that the M minimum cannot be responsible for any observed emission as it is considerably higher in energy. From the correlation of the PL data with the band structure calculations we can also assess if strain in the shell is a dominant factor. In Fig.4.16 we also show (green and red dotted lines) the calculated effect of the average compressive hydrostatic strain on the $\Gamma_{8C} - \Gamma_{9V}$ and $\Gamma_{7C} - \Gamma_{9V}$ transitions, using the theoretically expected strain without relaxation via defects (Table 4.1). It can be seen that the band shift compatible with the maximum compressive hydrostatic strain (absence of plastic relaxation) moves the $\Gamma_{8C} - \Gamma_{7C}$ crossover towards the WZ InP side. From this it can be concluded therefore that the strain in the nanowires is almost completely relaxed through the previously described geometrical effect and plastic relaxation confirming the structural analysis. The spread obtained in the data-points in Fig.4.16 is likely due to a small ($\leq 1\%$) residual compressive strain in some nanowires, which raises the $\Gamma_{7C} - \Gamma_{9V}$ transition to higher energies.

4.5 Conclusions

In this work we have realized WZ GaP/ $\text{In}_x\text{Ga}_{1-x}\text{P}$ core-shell nanowires with tunable Indium fraction between $0 < x < 0.75$, obtaining tunable polarized light emission between 590nm (2.1eV) and 760nm (1.63eV). From the analysis of the time-resolved and temperature-dependent photoluminescence and the comparison of the experimental data with the theoretical DFT model we have identified the $\Gamma_{7C} - \Gamma_{8C}$ conduction band crossover of $\text{In}_x\text{Ga}_{1-x}\text{P}$. We locate this crossover at an Indium fraction in the interval $0.25 < x < 0.38$, according to the experimental data, in qualitative agreement with theoretical simulations. As we have seen, the discrepancy in the crossover composition might be due to the uncertainty in the experimental method of the PL-TEM correlation. In order to improve the accuracy of the identification of the crossover composition, future work should focus first on the growth of homogeneous WZ $\text{In}_x\text{Ga}_{1-x}\text{P}$, for example by growing shells on lattice-matched cores. As WZ $\text{In}_x\text{Ga}_{1-x}\text{P}$ with $x \geq 0.4$ has a Γ_{7C}

conduction band minimum, this material can be used for efficient light emission in light emitting diodes. In order to tune further the band gap and extend it to higher energies, alloying with Aluminum is desirable, forming WZ AlInGaP or WZ AlInP. In particular, WZ AlInP for green light emission will be explored in the following Chapter.

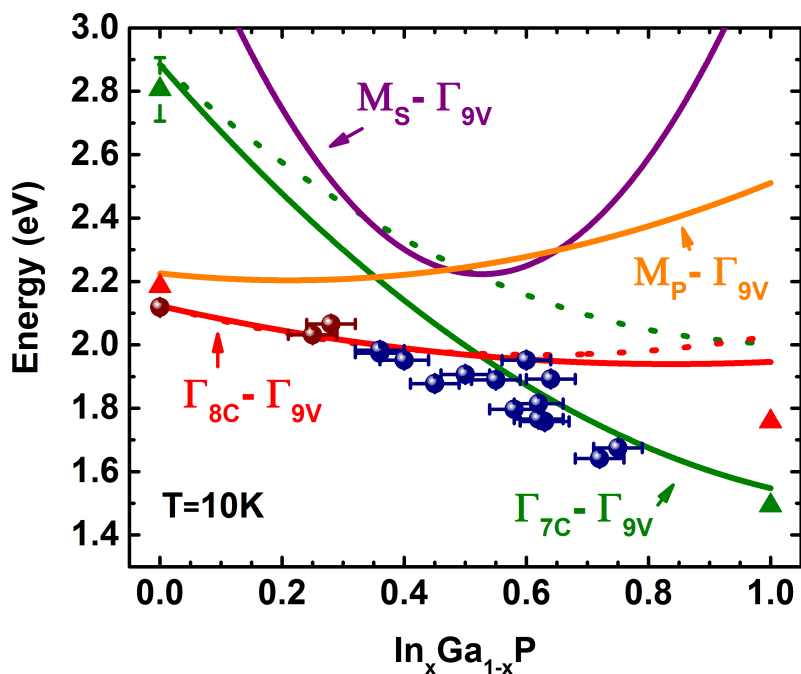


Figure 4.16: Experimental and simulated data of the main optical transitions in WZ $\text{In}_x\text{Ga}_{1-x}\text{P}$. Blue (dark red) circles: emission attributed to band to band $\Gamma_{7C} - \Gamma_{9V}$ ($\Gamma_{8C} - \Gamma_{9V}$ -related DAP) transition. Green (bright red) triangles: data from literature for the $\Gamma_{7C} - \Gamma_{9V}$ ($\Gamma_{8C} - \Gamma_{9V}$) transition. Lines: calculated energy values of the optical transitions in WZ $\text{In}_x\text{Ga}_{1-x}\text{P}$. Green solid line: $\Gamma_{7C} - \Gamma_{9V}$ transition. Red solid line: $\Gamma_{8C} - \Gamma_{9V}$ transition. The $\Gamma_{8C} - \Gamma_{7C}$ crossover is in this way estimated to lie at $x=0.53$. Green (red) dotted line: simulated $\Gamma_{7C} - \Gamma_{9V}$ ($\Gamma_{8C} - \Gamma_{9V}$) transition under average compressive hydrostatic strain. Data for average compressive strain in the shell as a function of composition are taken from Table 1.

Chapter 5

Infrared to green emitting pure wurtzite AlInP nanowires

In Chapter 4 we have realized WZ $\text{In}_x\text{Ga}_{1-x}\text{P}$ and studied its optical properties. In light of technological applications, we have found that the realization of efficient LEDs is theoretically possible, but only up to an emission energy of roughly 2.0eV, in the red range. We therefore now try to increase this limit through the substitution of Aluminum in place of Gallium, as this will yield a higher band gap of the alloy. Growing WZ $\text{Al}_x\text{In}_{1-x}\text{P}$ in fact allows us to tune the emission of the material across a wide range in the near infrared (NIR) and visible (VIS) spectrum, while also obtaining a nanowire geometry, ideal for LEDs and lasers.

5.1 AlInP nanowires growth

The catalyst-free selective area growth is performed in an Aixtron 200 horizontal flow MOVPE reactor, on a patterned (111)A ZB InP surface as described in Chapter 3. The pattern is fabricated with nanoimprint lithography, with hole size 200nm and pitch 512nm. The growth is performed at 700°C, using Trimethylindium (TMIn), Trimethylaluminum (TMAI) and Phosphine (PH_3) and the results are shown in Fig.5.1. The growth protocol is divided in two

⁰Contributions to this work: Dr. M.A. Verheijen (Philips Innovation Services) performed the TEM analysis, Dr. A Belabbes (KAUST) and Prof. F. Bechstedt (University of Jena) performed the DFT calculations, M. Kruijssse and S.P.M. de Jong (TU/e) provided research assistance on PL measurements.

steps: growth of a short WZ InP stem (about 100nm), followed by the growth of WZ AlInP. We tested the effect of the WZ InP stem on WZ $\text{Al}_x\text{In}_{1-x}\text{P}$ nucleation: the nanowires nucleate when the stem is used, whereas the nanowire formation is completely hindered when the stem is absent, as we show in Fig.5.2. This is very likely due to the insufficient growth rate anisotropy of WZ $\text{Al}_x\text{In}_{1-x}\text{P}$: without a fast growth in the axial direction, the nanowire itself cannot form, leading to formation of irregular, low aspect ratio crystals. WZ InP is therefore necessary to start the nanowire growth, which can be then continued by WZ $\text{Al}_x\text{In}_{1-x}\text{P}$.

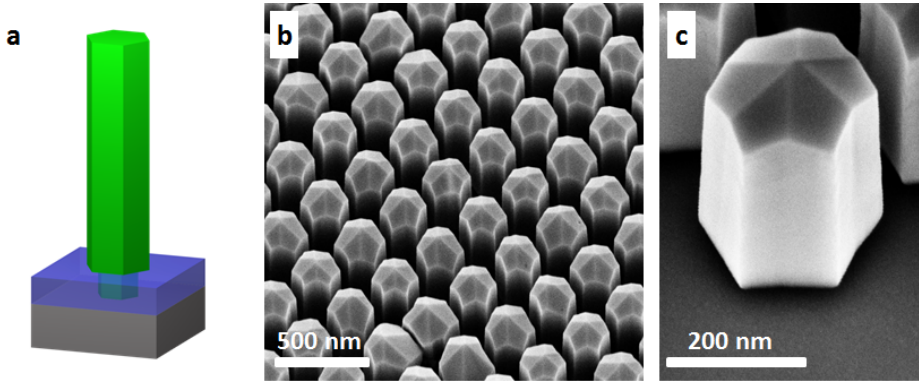


Figure 5.1: (a) Concept of an $\text{Al}_x\text{In}_{1-x}\text{P}$ nanowire. (b) SEM image of a WZ $\text{Al}_{0.25}\text{In}_{0.75}\text{P}$ nanowire array. (c) SEM image of a single WZ $\text{Al}_{0.25}\text{In}_{0.75}\text{P}$ nanowire, showing the complex faceting.

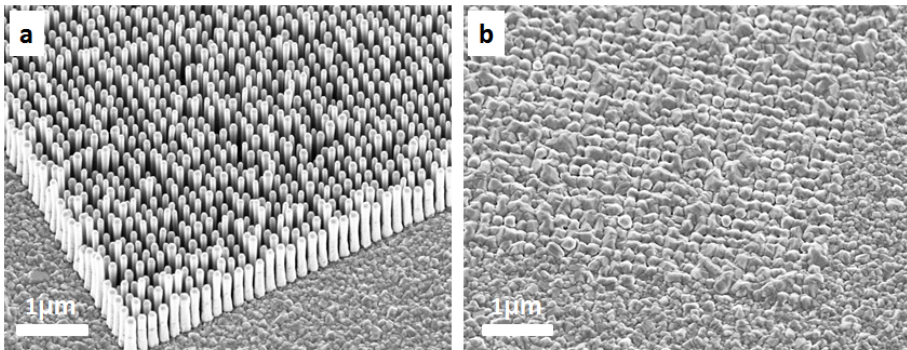


Figure 5.2: Influence of the WZ InP stem on WZ $\text{Al}_x\text{In}_{1-x}\text{P}$ nanowire formation. (a) With WZ InP stem. (b) Without WZ InP stem.

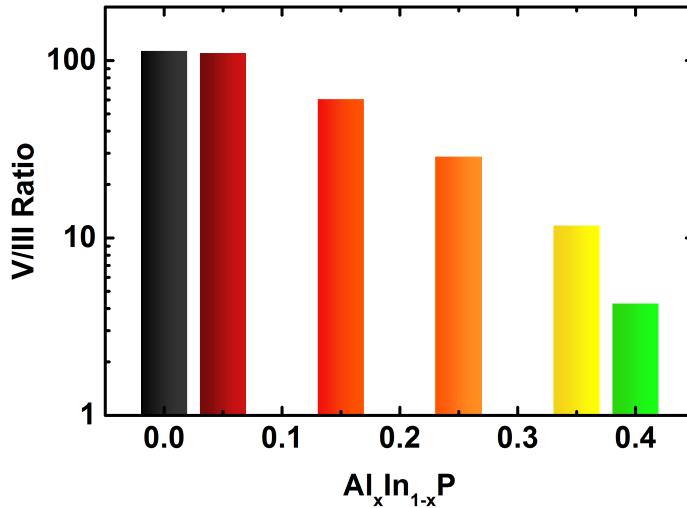


Figure 5.3: V/III ratio as a function of the composition of $\text{Al}_x\text{In}_{1-x}\text{P}$ nanowires. The values are given for the samples used in this work.

We found that the optimized V/III ratio for WZ $\text{Al}_x\text{In}_{1-x}\text{P}$ is dependent to the composition. In particular, the V/III ratio had to be lowered with increasing Aluminum fraction, as shown in Fig.5.3, up to an extremely low value of about 3.5, in the case of WZ $\text{Al}_{0.40}\text{In}_{0.60}\text{P}$. Our understanding is that Aluminum has low surface diffusivity, as the Al-P is stronger than the In-P bond⁵⁹, and lowering the V/III ratio raised the mean free path of the Al adatoms, allowing them to reach the nanowires more efficiently. In fact, for too high V/III ratio we observed parasitic growth on the SiNx mask, indicating that the material nucleated before reaching the nanowires. The presence of Aluminum also lowers the aspect ratio of the nanowires, promoting radial growth, a direct consequence of the low diffusivity, which prevents Al atoms to reach the top of the nanowires. WZ InP nanowires in fact show an aspect ratio which is higher by a factor of 2-3 compared to WZ $\text{Al}_x\text{In}_{1-x}\text{P}$ nanowires grown on the same pattern for the same amount of time, as shown in Fig.5.4.

The V/III ratio appeared to change the top faceting of the nanowires, ranging between top flat $\{0001\}$ polar facets and slanted $\{10\bar{1}2\}$ semipolar facets as shown in Fig.5.4 and more in detail in Fig.5.5. The presence of different faceting seems to be of kinetic origin, related to the V/III ratio during the growth, which enhances or suppresses the growth of the different facets. With a lower V/III ratio, the semipolar $\{10\bar{1}2\}$ facets tend to be favored. This behavior has also been ob-

served in ZnO nanowires, which always adopt WZ crystal symmetry, where the supersaturation during the growth determines the top faceting⁶⁰. High-index facets tendentially possess a higher surface energy density and typically vanish quickly in favor of the low-index facets like the {0001}. However, recent literature⁶⁰ suggests that if a relevant energetic barrier is present which prevents the diffusion of the adatoms between a high-index facet and a low-index one, such high-index facet can form, although thermodynamically metastable. This effect happens mostly at the perimeter of the top faceting of the nanowire, where the nuclei of new facets appear, then form a crystal plane layer by layer.

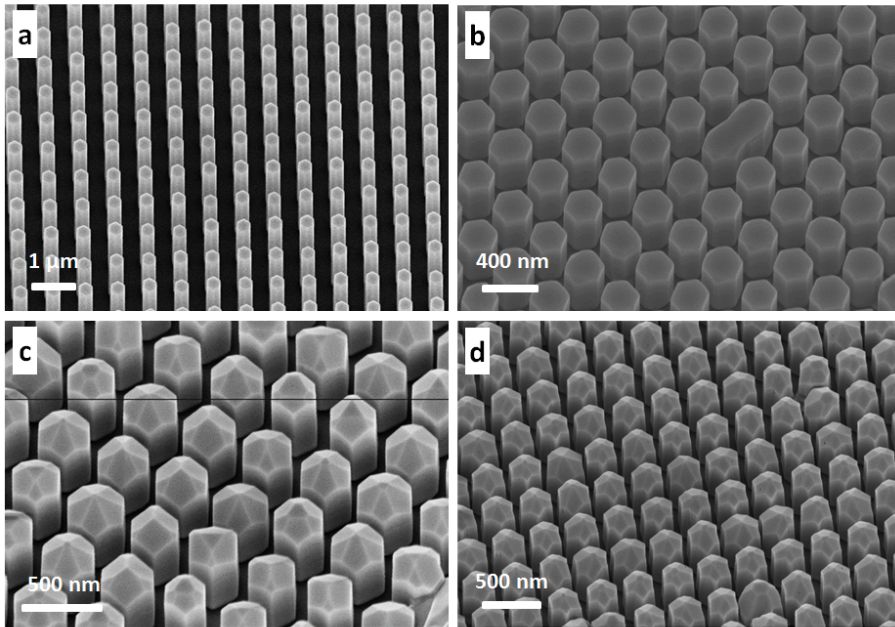


Figure 5.4: SEM images of WZ $\text{Al}_x\text{In}_{1-x}\text{P}$ nanowire arrays. (a) $x = 0$ (b) $x = 0.05$ (c) $x = 0.15$ (d) $x = 0.35$. Notice the different aspect ratio between WZ InP and WZ $\text{Al}_x\text{In}_{1-x}\text{P}$, and the different top and side faceting.

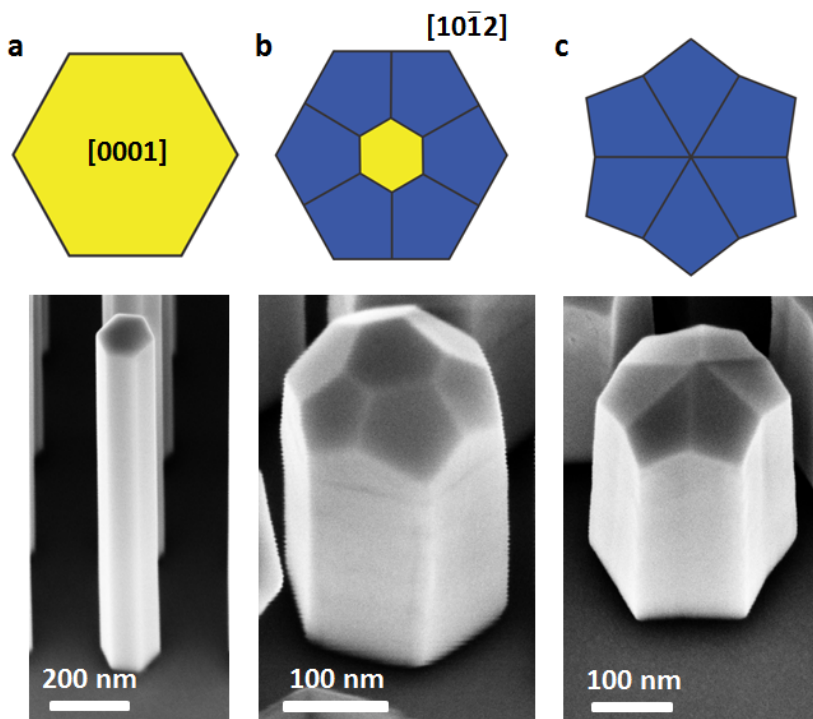


Figure 5.5: Examples of faceting in WZ $\text{Al}_x\text{In}_{1-x}\text{P}$ nanowires. Top row: scheme of the top faceting. Bottom row: SEM images. (a) WZ InP nanowire, showing an hexagonal $[0001]$ top facet. (b) WZ $\text{Al}_{0.15}\text{In}_{0.85}\text{P}$ nanowire, showing both the $[0001]$ facet and $\{10\bar{1}2\}$ top facets. (c) WZ $\text{Al}_{0.25}\text{In}_{0.75}\text{P}$, showing only $\{10\bar{1}2\}$ top facets.

The top facets seem to be connected to the dodecagonal cross-section of the nanowire. This complex cross-section is likely due to radial growth: in fact, when radial growth is not present, the cross section of wurtzite nanowires is hexagonal, as in WZ InP in Fig.5.5a. WZ $\text{Al}_x\text{In}_{1-x}\text{P}$ nanowires with high Aluminum fraction tend to expose high-index side facets, which should not be thermodynamically stable. It is likely that the formation of both the side and top facets are inter-related, one triggering the nucleation of the other through the aforementioned kinetic mechanism, as their geometry suggests. As a last remark, we can notice that even in the most regular sample shown in Fig.5.1b, some nanowires possess an asymmetric geometry, which indicates a kinetic facet formation mechanism rather than a thermodynamic one.

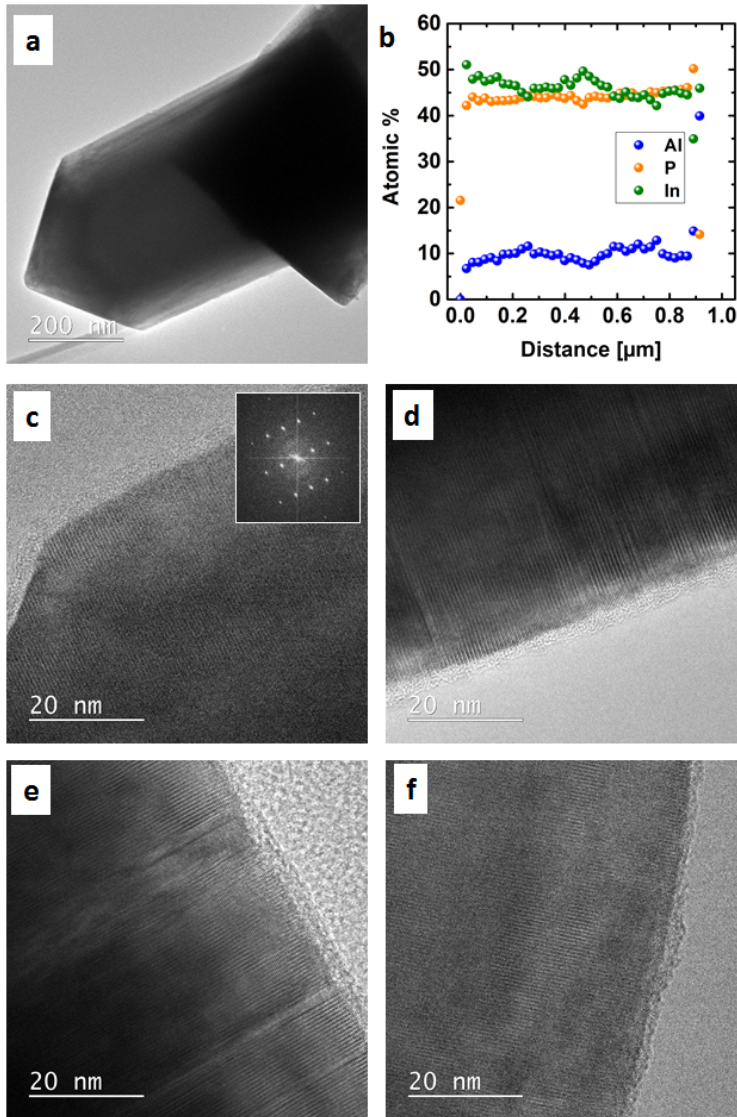


Figure 5.6: (a) TEM bright field images of a WZ $\text{Al}_{0.22}\text{In}_{0.78}\text{P}$ nanowire showing nearly perfect phase purity. (b) EDS line scan of the nanowire in (a), showing the chemical quantification. (c) HR-STEM image of the nanowire in (a). Inset: fast fourier transform of the image, demonstrating hexagonal crystal structure. (d-f) HR-STEM bright field images of other $\text{Al}_x\text{In}_{1-x}\text{P}$ nanowires: (d) $x = 0.05$ (e) $x = 0.15$ (f) $x = 0.35$.

In order to gain insight on the crystal structure, the $\text{Al}_x\text{In}_{1-x}\text{P}$ nanowires have been transferred by nanomanipulation to carbon mesh grids. HR-STEM imaging and EDS have been performed, as shown in Fig.5.6. EDS yielded the chemical composition of the nanowires, allowing us to calibrate the precursor flows during growth. Optimized recipes yielded low-defectivity Wurtzite ($<2\text{sf}/\mu\text{m}$) as shown in Fig.5.6c and f, while unoptimized nanowires showed a higher defectivity or mixed phase structure between wurtzite and zincblende, as in Fig.5.6d-e. Interestingly, defect-free WZ forms when the characteristic high-index faceting shown in Fig.5.1c is most regular across the sample. As we have seen in Chapter 2, we obtain wurtzite when the nucleation energies satisfy $\Delta G_{WZ}^* < \Delta G_{ZB}^*$, which depends on the supersaturation. Therefore, both the facet formation and crystal phase nucleation are related by the fact they are both determined by the supersaturation.

In order to obtain detailed information on the inner structure of the nanowires, we fabricated lamellae from the WZ $\text{Al}_{0.25}\text{In}_{0.75}\text{P}$ sample as shown in Fig.5.7 and Fig.5.8, using the procedure described in Chapter 3. In Fig.5.7 we see the entire lamella, where three nanowires have been cut. Of these, two have been cut perpendicularly to their growth axis, one parallel. From Fig.5.7 and Fig.5.8a-c we notice that the nanowires possess a core and a shell, although the growth protocol did not include any shell growth. The core shows a higher ($x=0.25$) Aluminum fraction than the shell ($x=0.20$). There are also evident Aluminum-rich segregations, which are usually formed at the edges between two facets. The adatoms in fact tend to migrate away from corners, as they possess a higher chemical potential than the facets. Statistically, the corners end up being enriched of the slowest species, in this case Aluminum. In this case they suggest that the shell grows with 60° -rotated facets respect to the core. A thin (about 10nm) Aluminum-rich inner shell is also visible between the first and second shell. In Fig.5.8e-f we show another lamella of a nanowire from the same sample, this time cut along the growth axis. In Fig.5.8f we notice that the bottom of the nanowire shows a higher Indium fraction than the top. We therefore conclude that the Indium-rich shell is thicker at the bottom of the nanowire, as suggested by the contrast in Fig.5.8e. In light of these results, the growth mechanisms appears particularly complex. To explain it, we formulate the following hypothesis: the epitaxy begins with the growth of a core with diameter of about 150nm with obliquous facets, giving the nanowire an inversely tapered geometry. We therefore understand that the Aluminum-rich segregations form at the top of the nanowire, at the edges between the top facets, during the growth itself. The shell grows almost at the same time, which renders the side facets of the nanowire vertical. We find a hint of this in Fig.5.8e, as we see that the Indium-rich shell meets the core at the top of the nanowire. The different composition might be given by different reactivity of the facets, which can cause preferential incorporation of one element

over another. Another explanation might be that, due to the large diameter of the wires and the relatively small pitch, the precursor gases cannot access the side facets as much as the top ones. In this case surface diffusion would play an important role, allowing the fastest diffusing species, in this case Indium, to reach the bottom of the nanowire more than the slower species, Aluminum.

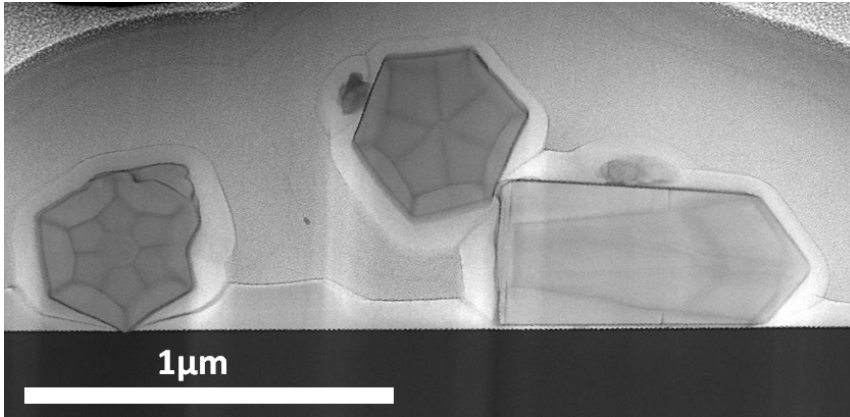


Figure 5.7: HAADF image of the lamella of three WZ $\text{Al}_{0.25}\text{In}_{0.75}\text{P}$ nanowires, two cut perpendicular to their growth axis, one parallel. We notice the presence of a core and a shell in all three nanowires. They both vary in thickness as a function of the length of the nanowire. We therefore deduce that the nanowire to the left was cut close to its bottom, while the central wire was cut closer to the top.

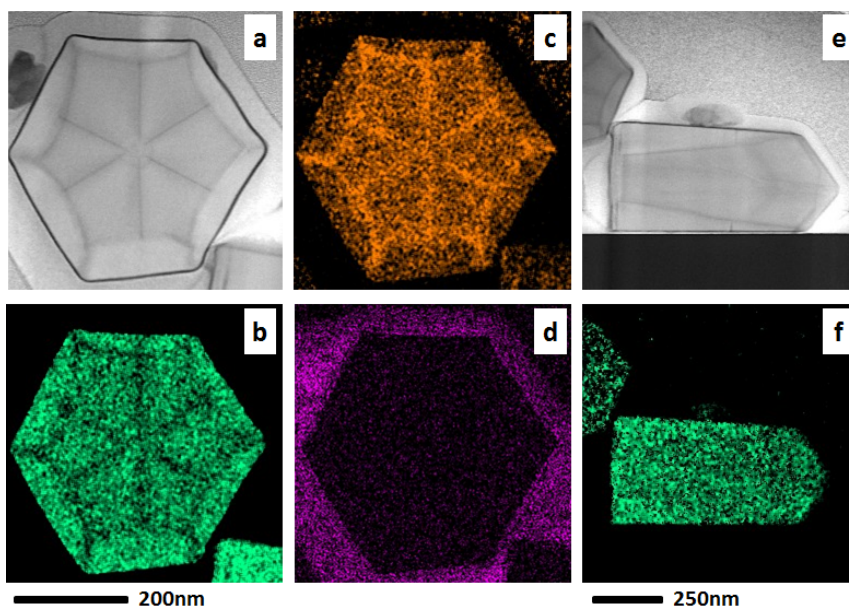


Figure 5.8: (a) HAADF image of the lamella of a WZ $\text{Al}_{0.25}\text{In}_{0.75}\text{P}$ nanowire. (b-d) EDS maps of the nanowire lamella: (b) Indium, (c) Aluminum, (d) Oxygen, showing no shell oxidation. The nanowire appears to be composed of a core and two shells with different composition. The inner shell shows higher Aluminum fraction. Inner shell: Aluminum $x=0.25$. Outer shell: $x=0.20$. Aluminum-rich sunburst segregations are present. The two shells present rotated segregations, which suggests a phenomenon of facet rotation during growth. (e) HAADF image of the lamella of a WZ $\text{Al}_{0.25}\text{In}_{0.75}\text{P}$ nanowire, where the nanowire was cut transversally across its growth axis. (f) EDS map of the same nanowire, showing the Indium signal. The bottom of the nanowire is more indium-rich than the top.

We also investigated a WZ $\text{Al}_{0.40}\text{In}_{0.60}\text{P}$ (average composition) nanowire in cross position, as shown in Fig.5.9. This nanowire was standing upside-down on the TEM grid carbon mesh, therefore we could image it from its bottom. The nanowire was damaged during the transfer, but its main features are clearly visible. The nanowire has an average Aluminum fraction of $x = 0.40$, but shows inhomogeneities. Aluminum-rich sunburst segregations with $x = 0.65$ are present, corresponding to the corners of the nanowire. This is due to the fact that the nanowire grew not only axially but also radially. Another explanation might be that the segregations have formed at the top of the nanowire, at the corners between the facets. However, contrary to the previous case, these segregations point towards the corners of the nanowire, therefore hinting towards the radial growth

mechanism. Interestingly, the nanowire shows a dodecagonal cross-section, therefore exposing high-index facets. This observation suggests once again that the exposed facets are formed kinetically, therefore they are the fastest to form. A minimum of x is reached in correspondence of the facets, where $x = 0.27$. Contrary to the nanowires in Fig.5.8, this nanowire does not present an Aluminum-poor shell. We therefore conclude that the growth conditions affect the presence of a shell, likely by controlling the side facets of the nanowire "core", which in turn determine the incorporation of Indium and Aluminum.

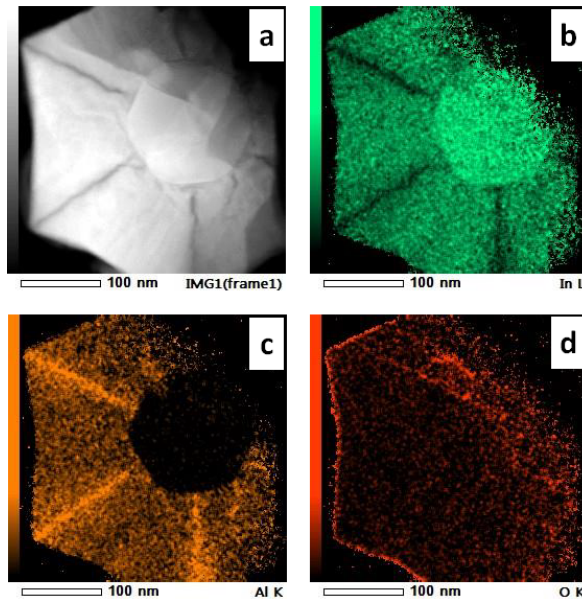


Figure 5.9: (a) HAADF image of a WZ $\text{Al}_{0.40}\text{In}_{0.60}\text{P}$ (average composition) nanowire, which was standing on the TEM carbon mesh, allowing cross-sectional imaging. The nanowire was damaged during the transfer, but its main features are clearly visible. (b-d) EDS maps of the nanowire: (b) Indium, (c) Aluminum, (d) Oxygen, showing little shell oxidation. The nanowire appears to be inhomogeneous due to the presence of Aluminum-rich sunburst segregations. The Aluminum fraction in these regions is $x = 0.65$, while the minimum Aluminum fraction, reached halfway between the segregations themselves, is $x = 0.27$. The pure InP section is the stem of the nanowire, used to obtain correct nucleation.

5.2 Optical Properties

The optical properties of WZ $\text{Al}_x\text{In}_{1-x}\text{P}$ nanowires are investigated with photoluminescence (PL). In Fig.5.10 we show the steady-state PL at 10K of several WZ $\text{Al}_x\text{In}_{1-x}\text{P}$ nanowire arrays with Al fraction $0 < x < 0.40$, while in Fig.5.11 we show the photoluminescence of the same samples at room temperature. We therefore demonstrate room temperature emission tunability between the near-infrared 875nm (1.43eV) and the green 555nm (2.23eV). The emission of WZ InP is the sharpest in the dataset, especially at low temperature. WZ $\text{Al}_x\text{In}_{1-x}\text{P}$ is in fact affected by alloy broadening, namely the wavelength dispersion of the photoluminescence emission due to alloy disorder. Also, local compositional fluctuations can cause further broadening⁶¹: we see in fact low energy tails which suggest the presence of impurities, or pockets of material with higher Indium content and therefore lower band gap, as we saw in Fig.5.8, especially in the WZ $\text{Al}_{0.15}\text{In}_{0.85}\text{P}$ and WZ $\text{Al}_{0.40}\text{In}_{0.60}\text{P}$ samples. The WZ $\text{Al}_{0.05}\text{In}_{0.95}\text{P}$ and WZ $\text{Al}_{0.15}\text{In}_{0.85}\text{P}$ samples contain stacking faults as previously shown in Fig.5.6, which contribute to broadening. In fact, the presence of ZB in a WZ crystal gives origin to type II transitions at a lower energy than the WZ band gap, leading to peak broadening. Also, the growth kinetics might be different in the case of ZB and WZ nucleation, therefore alloy fluctuations might be enhanced. The WZ $\text{Al}_{0.25}\text{In}_{0.75}\text{P}$ and WZ $\text{Al}_{0.35}\text{In}_{0.65}\text{P}$ show a narrower peak, and in fact show lower defectivity than the previous two samples (see Fig.5.6). In order to understand more on the identity of the photoluminescence peaks we observe, we analyze the dependence of the emission as a function of the excitation power.

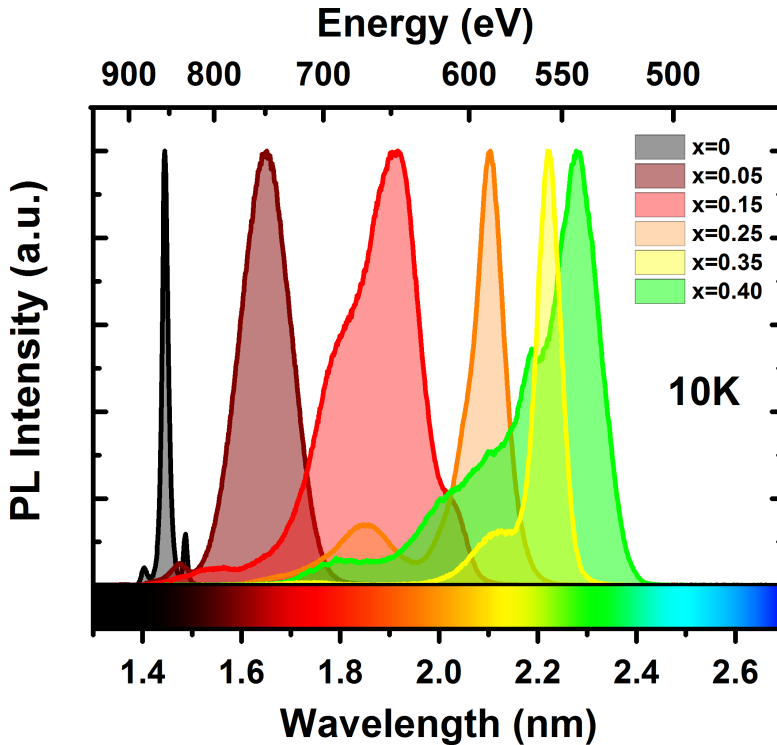


Figure 5.10: Low temperature photoluminescence spectra of WZ $\text{Al}_x\text{In}_{1-x}\text{P}$ nanowire arrays. The color coding approximates the real emission color at room temperature. The WZ InP spectrum presents three peaks, corresponding to band gap-related emission (1.49 eV), donor-acceptor pair recombination (1.44 eV) and ZB substrate (1.40 eV)⁶². The spectra of all WZ $\text{Al}_x\text{In}_{1-x}\text{P}$ nanowire arrays are subject to alloy broadening. The spectra of WZ $\text{Al}_{0.05}\text{In}_{0.95}\text{P}$ and WZ $\text{Al}_{0.15}\text{In}_{0.85}\text{P}$ are additionally broadened due to the presence of stacking faults, which causes additional type 2 transition between ZB and WZ.

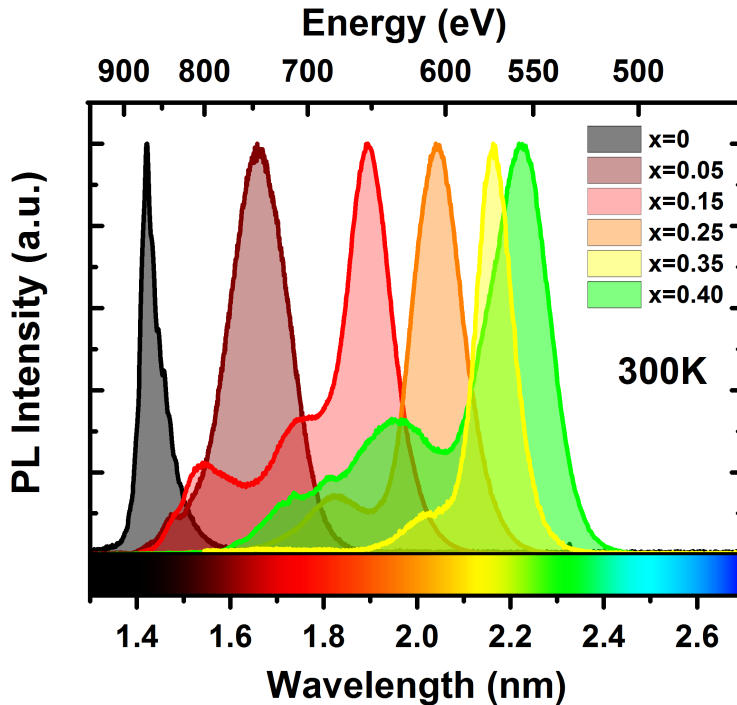


Figure 5.11: Room temperature photoluminescence spectra of WZ $\text{Al}_x\text{In}_{1-x}\text{P}$ nanowire arrays showing emission tunability between about 850nm (1.45eV) and 555nm (2.23eV). The color coding approximates the real emission color. The spectra of WZ show alloy broadening and lower energy emission from pockets with higher Indium content and possible stacking faults (see TEM analysis).

5.2.1 Power dependence of the photoluminescence

We now study the power-dependence of the photoluminescence of the WZ $\text{Al}_x\text{In}_{1-x}\text{P}$ nanowire arrays, in order to gain insight on the origin of the emission. In Fig.5.12a we show the photoluminescence spectrum as a function of excitation of the WZ $\text{Al}_{0.40}\text{In}_{0.60}\text{P}$ nanowire array. We find two peaks, one at 2.1eV, which dominates at low excitation power, and another one at about 2.3eV, which instead dominates at higher excitation power. In Fig.5.12b we show the integrated photoluminescence intensity as a function of excitation power density for the same array, finding a linear relation. The green datapoints refer to the 2.3eV peak and show a slope $S = 1.05 \pm 0.05$, while the red ones refer to the 2.1eV peak,

with a slope of $S = 0.75 \pm 0.05$. The slope close to unity indicates a band-gap related recombination, while a lower slope points towards an impurity recombination, such as donor-acceptor pairs. It is possible that the high concentration of Aluminum, which possesses high reactivity, might have promoted the incorporation of impurities such as carbon or oxygen. The resulting binding energy (about 200meV) is high, but realistic for impurities in a wide band gap material. Another explanation might be that the extremely low V/III ratio promoted phase segregation and enhanced the phenomenon of pocketing, therefore causing a relevant volume of material to have a lower band gap and therefore emit at lower energy. The EDS analysis in Fig.5.8 and Fig.5.9 suggest that this might be the case. Regarding the lower slope of the power-dependence, it is possible that these low band gap regions are usually located closer to the surface and therefore are particularly affected by surface recombination, which lowers the efficiency. In Fig.5.13 we plot the slope of the linear dependence between I_{PL} and P_{EXC} at low temperature, as a function of the composition, for all the nanowire arrays we studied. For clarity, here we plot only the higher energy emission, for example the 2.3eV peak in the WZ $\text{Al}_{0.40}\text{In}_{0.60}\text{P}$ sample, with the exception of WZ InP, where we report the band-gap related emission (BGR) and the donor-acceptor pair recombination (DAP), as they are well-known in literature^{45;48} and help us in the interpretation of the power-dependence of the other samples. The BGR peak of WZ InP shows a value of $S = 1.20 \pm 0.05$, while the DAP recombination has a value of $S = 0.80 \pm 0.05$. The band-gap related recombination should have a value of approximately 1, therefore it is possible that the emission we are observing contains some excitonic contribution, for example bound excitons, which present a slope higher than unity⁶³. We see that the slope of the power dependence increases gradually with Aluminum fraction, up to values around 1 for $x \geq 0.25$. It is possible that defectivity, as shown in Fig.5.6, might affect the result and lead to a lower slope for $x < 0.25$. For $x > 0.25$ the values of the slopes are compatible with unity, therefore confirming the band gap-related origin of the emission observed. This is an important result, as a strong band gap-related emission is needed for solid state lighting applications and the fact we obtained a power dependence slope close to unity in the yellow and green range is a strongly encouraging result. However, more evidence is needed in order to draw conclusions on the nature of the photoluminescence observed. We therefore proceed to analyze the time-dependent and temperature-dependent behavior of the emission.

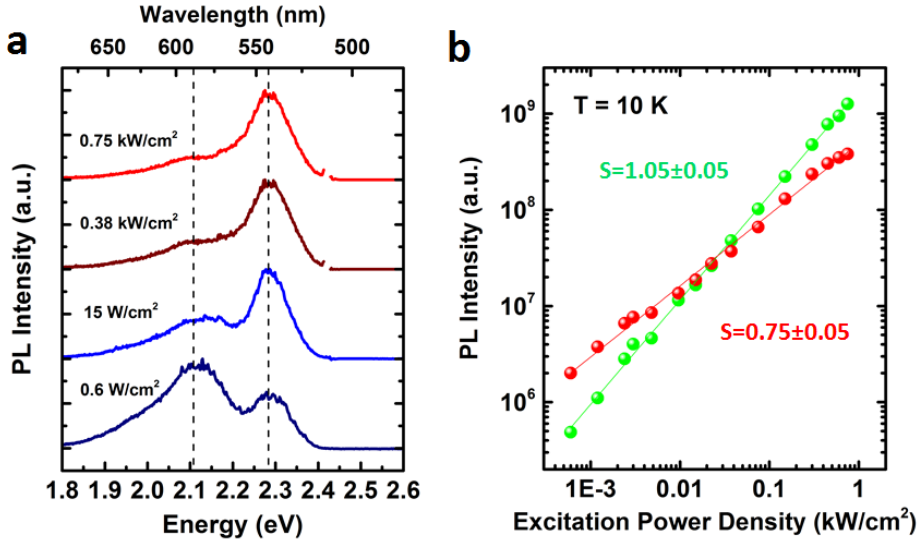


Figure 5.12: (a) Photoluminescence spectra of the WZ $\text{Al}_{0.40}\text{In}_{0.60}\text{P}$ nanowire array as a function of excitation power density at 10K. We notice two peaks, one at 2.1eV dominating a low excitation power, one close to 2.3eV, becoming dominant at higher excitation power. (b) Integrated photoluminescence intensity as a function of excitation power density for both peaks in (a). Red: 2.1eV peak. Green: 2.3eV peak. The slope of the 2.3eV peak is close to unity, indicating a band gap-related recombination. The slope of the 2.1eV peak is instead 0.75 ± 0.05 , indicating an inefficient recombination mechanism, for example impurity recombination.

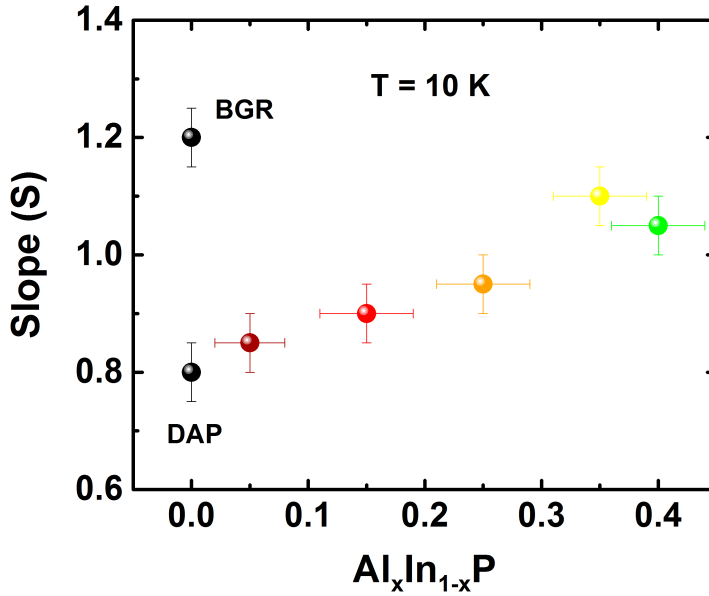


Figure 5.13: Slope of the integrated photoluminescence intensity as a function of power, at 10K of WZ $\text{Al}_x\text{In}_{1-x}\text{P}$ nanowire arrays, plotted as a function of Aluminum fraction. The color coding approximates the real emission color. Two values are reported for WZ InP, as it presented two peaks: a donor-acceptor pair (DAP) recombination and a band-gap related (BGR) emission. The slope S of WZ $\text{Al}_x\text{In}_{1-x}\text{P}$ with $x \neq 0$ approaches unity with increasing Aluminum fraction. This might be due to decreasing defectivity as shown in Fig.5.6. A value close to unity indicates purely radiative recombination.

5.2.2 Time-resolved photoluminescence

In order to acquire an insight on the nature of the optical transitions involved, time-resolved photoluminescence (TRPL) is investigated. The Picoharp time-correlated acquisition system described in Chapter 3 is used. The carrier lifetime as a function of the alloy composition is shown in Fig.5.14 at 10K (circles) and 300K (triangles). Again, we report two datapoints at 10K for WZ InP, corresponding to the BGR and DAP peaks. We see here a strong difference, with the BGR peak showing a very short lifetime of 0.5ns, while the DAP peak shows a two orders of magnitude longer lifetime of 80ns. A short lifetime is typical for a direct recombination with high oscillator strength, while the long lifetime for the DAP peak is explained by the small overlap of the carrier wavefunctions in the impurity pairs, which lowers the recombination rate. Also here we can use WZ InP as a guide to interpret the rest of the data. For all WZ $\text{Al}_x\text{In}_{1-x}\text{P}$ compositions we observe a rather short lifetime at 10K, with $1.5 \leq \tau \leq 0.5$, proving a direct-allowed recombination mechanism, which is a major point for application in solid state lighting. As a side note, we see that the WZ $\text{Al}_{0.05}\text{In}_{0.95}\text{P}$ sample shows a somewhat longer lifetime at 10K. This might indicate some contribution of impurities or type II recombination at stacking faults, which increases the overall lifetime⁶⁴. At room temperature the carrier lifetime is below 1ns for all samples and always comparable or lower than at 10K. This is expected, as non-radiative recombination channels might be activated with increasing temperature, therefore decreasing the overall carrier lifetime.

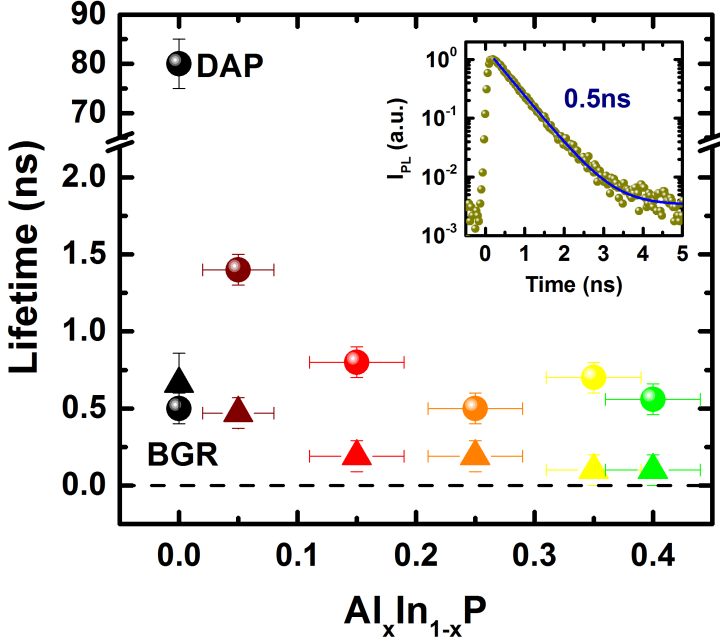


Figure 5.14: Time-resolved photoluminescence measurements at 10K of WZ $\text{Al}_x\text{In}_{1-x}\text{P}$ nanowire arrays as a function of composition. The color coding approximates the real emission color. The datapoints are collected at 10K (circles) and 300K (triangles). The band gap-related emission lifetimes are all around 1ns, suggesting direct recombination. The resolution limit of the setup is down to 0.3ns, values below should be considered below the instrumental resolution limit. Inset: TRPL decay plot of the WZ $\text{Al}_{0.25}\text{In}_{0.75}\text{P}$ nanowire array, fitted with a single exponential decay.

5.2.3 Temperature-dependent photoluminescence

In order to complete our understanding of the photoluminescence, we analyze its temperature behavior. In Fig.5.15a we show the photoluminescence of the WZ $\text{Al}_{0.40}\text{In}_{0.60}\text{P}$ nanowire array as a function of temperature. We notice again the two peaks, one dominant at 2.3eV and a less intense one, redshifted. In this case the smaller peak is at a different energy than in Fig.5.12, previously at 2.1eV, now at 2.2eV. This is because the position of this peak resulted different in different points of the sample, while the main peak shifted by a smaller amount. This is due to inhomogeneities during the growth process, which lead to nanowires with slightly different composition as a function of the position on the substrate. The

change in position of the peaks therefore corroborates the hypothesis that the lower energy peak is emitted by sections of the nanowire with different composition, as we saw in the EDS analysis. Increasing the temperature from 10K, the main peak first blueshifts by about 15meV. This behavior can be explained by carrier detrapping from local alloy fluctuations due to increased thermal energy. The carriers therefore recombine also in regions with slightly higher band gap, leading to blueshifted emission. Increasing the temperature further, the main peak redshifts, ending at 2.23eV at room temperature, following therefore the typical behavior of band gap decrease with temperature found in semiconductors⁶⁵. Fig.5.15b we show the integrated photoluminescence intensity of the WZ Al_{0.40}In_{0.60}P as a function of the inverse of temperature. We fit the data using an Arrhenius-type function⁶⁶:

$$I(T) = \frac{I_{10K}}{1 + A \cdot \exp(-E_1/kT) + B \cdot \exp(-E_2/kT)} \quad (5.1)$$

where A and B are parameters describing the process rate and E_1 and E_2 are activation energies of a thermally activated process which quenches the photoluminescence. Two activations energies have been used, as the use of only one activation energy led to a poor fit. We obtained $E_1 = 11meV$ and $E_2 = 58meV$. E_1 corresponds to a temperature of 127K, which is comparable with the temperature at which we obtain a blueshift in Fig.5.15a, around 100K. E_2 is harder to relate to any known quantity: it might be another detrapping energy from deeper pockets, or the binding energy of an impurity which was contributing to the emission. Repeating the same analysis for the other WZ Al_xIn_{1-x}P samples, we obtain very similar activation energies, which suggests that the same processes happen in all our samples. We now examine the integrated photoluminescence intensity at 10K (I_{10K}) and 300K (I_{300K}) as shown in Fig.5.16. We can see that the intensity overall tends to decrease with increasing Aluminum fraction, with this trend being much more pronounced at 300K than at 10K. At low temperature the intensity overall decreases of a factor of 5, while at 300K it decreases by a factor of 50. We also calculate the ratio between I_{300K}/I_{10K} as it completes the overview on the temperature behavior of the emission. We see that indeed this ratio decreases by an order of magnitude from WZ InP to WZ Al_{0.40}In_{0.60}P, following the same trend of the PL intensity at 300K. However, we don't see abrupt changes neither in the integrated intensity nor in the I_{300K}/I_{10K} ratio from one sample to the other, as we would expect in case of a band crossover, as we saw in Chapter 4. This gradual trend suggests that non-radiative recombination channels are progressively increasing with increasing Aluminum fraction. Surface recombination is in fact expected to be very fast in Al_xIn_{1-x}P with high x, with surface recombination velocity $S \approx 10^5 - 10^6$ cm/s, in the same range of GaAs^{67,68}.

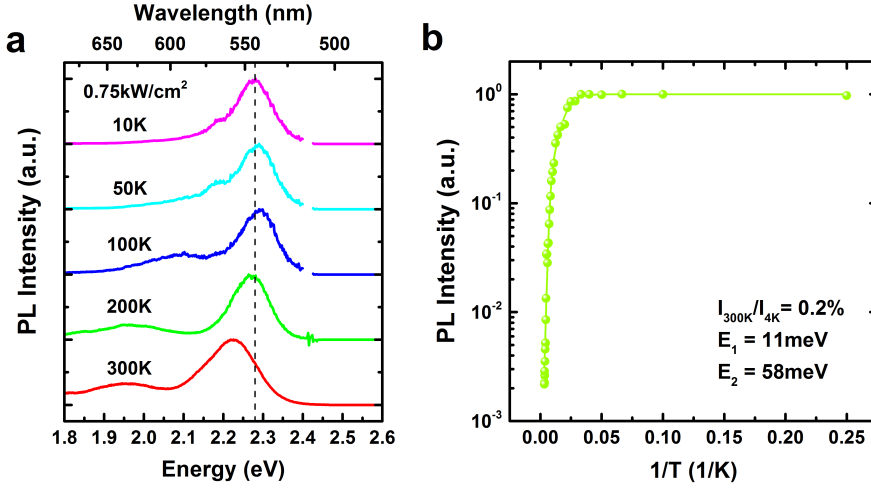


Figure 5.15: (a) Photoluminescence spectra of the WZ $\text{Al}_{0.40}\text{In}_{0.60}\text{P}$ nanowire array as a function of temperature between 10K and 300K. We notice again two peaks, a main one at 2.3eV and a less intense one at lower energy. The main peak first blueshifts, then redshifts. This might be due to carrier detrapping from local alloy fluctuations, then followed by the typical behavior of band gap decrease with temperature found in semiconductors. (b) Integrated photoluminescence intensity as a function of temperature of the main peak in (a). The I_{300K}/I_{4K} ratio is 0.2%. We fitted the datapoints with a double exponential function, extracting two activation energies for thermally activated processes which quench the photoluminescence.

However, such high recombination velocity would not allow the strong room temperature emission we observe, like in the case of GaAs where surface passivation is needed^{69;70}, therefore we speculate that for WZ $\text{Al}_x\text{In}_{1-x}\text{P}$ surface recombination unexpectedly plays a smaller role than in ZB $\text{Al}_x\text{In}_{1-x}\text{P}$. This is surprising also due to the fact that nanowires possess a larger surface to volume ratio than planar material. It is possible that the side facets of the nanowires (e.g. $\{10\bar{1}0\}$, $\{11\bar{2}0\}$) possess a lower density of surface states than in ZB material, leading to lower surface recombination velocity. Alloy fluctuations might also play a role, as they tend to localize the carriers, preventing them from reaching the surface and therefore avoiding non-radiative recombination. With rising temperature, the carriers are detrapped, leading to lower radiative efficiency at higher temperature. In Fig.5.8 we showed nanowires with a very peculiar structure, showing segregations with high Aluminum fraction, which constitute barriers to the carriers. Such a mechanism might therefore prevent carriers from reaching the surface, thus blocking a major non-radiative recombination channel. How-

ever, in Fig.5.9 we showed that some samples might not have such a structure, therefore this explanation cannot hold for the entire dataset, making the hypothesis of increasing surface recombination a more likely explanation. Aluminum is also well known for binding with Oxygen, forming non-radiative recombination centers. Oxygen impurities, which might be present in an MOVPE reactor, would therefore contribute to lower the efficiency of WZ $\text{Al}_x\text{In}_{1-x}\text{P}$, a phenomenon well known, for example, in ZB AlGaInP ⁷¹ and AlGaAs ⁷², where the density of non-radiative recombination centers increases with increasing Aluminum fraction. An alternative explanation is a higher electron scattering into the indirect M conduction band minimum, which is expected to increase with Aluminum fraction: since the radiative recombination probability in the indirect minimum is very small, these carriers tend to recombine non-radiatively, for example at the surface or at point defects like vacancies⁷³.

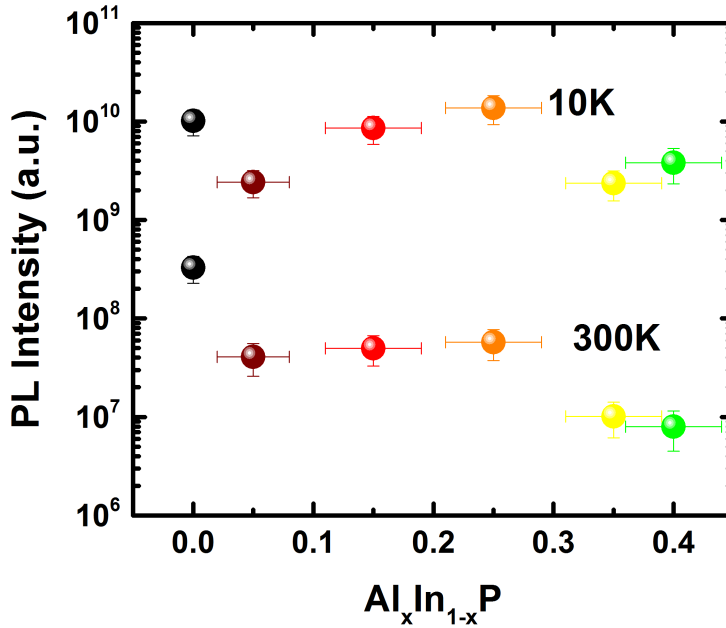


Figure 5.16: Integrated photoluminescence intensity of WZ $\text{Al}_x\text{In}_{1-x}\text{P}$ nanowire arrays as a function of composition at 10K and 300K. At 10K, the intensity of all samples is within an order of magnitude, while at 300K a trend is visible, where the intensity decreases with increasing Aluminum fraction. This is likely due to increasing surface recombination, as a higher Aluminum fraction makes the surface more reactive to the atmospheric oxygen, producing an oxide layer. Another hypothesis is that the decreasing energy difference between the Γ and M conduction band minima might allow increasing carrier scattering in the indirect minimum, increasing the probability of non-radiative recombination.

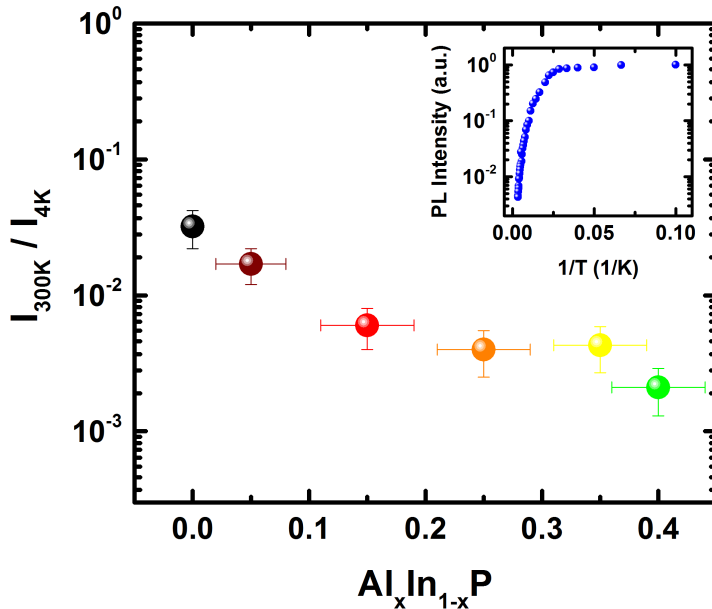


Figure 5.17: Internal quantum efficiency (IQE) of WZ $\text{Al}_x\text{In}_{1-x}\text{P}$ nanowire arrays as a function of composition. The color coding approximates the real emission color at 300K. The IQE of the samples is comparable within one order of magnitude and decreases with increasing Aluminum fraction, respecting the same trend observed in Fig.5.16. Inset: integrated photoluminescence intensity as a function of the inverse of temperature of the WZ $\text{Al}_{0.25}\text{In}_{0.75}\text{P}$ nanowire array.

5.3 Band structure of WZ AlInP

The band structure of WZ $\text{Al}_x\text{In}_{1-x}\text{P}$ is calculated by Dr. A. Belabbes (KAUST) and Prof. F. Bechstedt (University of Jena) using density functional theory (DFT) calculations in the local density approximation (LDA 1/2) and is shown in Fig.5.18a, where we compare the model data (lines) with the experimental data (circles). The theoretical model of WZ $\text{Al}_x\text{In}_{1-x}\text{P}$ predicts a fairly complex behavior as a function of composition, with two crossovers. WZ InP possesses a Γ_7 conduction band minimum (CBM) but around $x = 0.25$ WZ $\text{Al}_x\text{In}_{1-x}\text{P}$ presents a direct to pseudo-direct conduction band crossover, switching to a Γ_8 CBM. As we can see in Fig.5.18b, the oscillator strength of the CBM-VBM transition is equal to zero around $x = 0.25$. For $x > 0.25$, WZ $\text{Al}_x\text{In}_{1-x}\text{P}$ is expected to be a

very weak light emitter at room temperature, due to its pseudo-direct band gap. Close to $x = 0.6$ we find a pseudo-direct to indirect conduction band crossover, as the minimum in the M point becomes the CBM. Also a third crossover is actually present, although it does not involve the CBM: the $\Gamma_7 - M$ crossover at about $x = 0.40$. From these results we can conclude that, according to the DFT calculations, the predicted interesting composition range for efficient light emission in WZ $\text{Al}_x\text{In}_{1-x}\text{P}$ should be $0 \leq x \leq 0.25$. However, we observe strong room temperature photoluminescence also for $0.25 \leq x \leq 0.40$, which contradicts the theoretical prediction. The experimentally observed behavior was only gradually changing with composition, which is in contrast with a sharp crossover behavior like in WZ $\text{In}_x\text{Ga}_{1-x}\text{P}$ ⁷⁴. The discrepancy is due to the fact that the DFT model is developed considering a digital alloy, where substitutional atoms (e.g. Aluminum) are placed at regular distances between each other. This is however not realistic: substitutional atoms tend to distribute randomly and this factor has to be taken into account.

We therefore now repeat the DFT calculations for different atom arrangements, namely a random configuration, where the substitutional atoms are placed randomly; a clustered configuration, where substitutional atoms tend to be closer to each other; a superlattice configuration, where substitutional atoms are placed in precise atomic planes at regular distances, to reproduce an ordering effect as reported in literature for ZB $\text{Al}_x\text{In}_{1-x}\text{P}$ ^{75;76;77}. We then average the results obtained from these configurations and obtain a new predicted band structure, as shown in Fig.5.19a. We now see that the $\Gamma_{8C} - \Gamma_{9V}$ transition is now at higher energy and the Γ_{8C} band is never the CBM. The only crossover at the CBM is now the direct-indirect $\Gamma_{7C} - M$ crossover around $x = 0.43$. These new DFT calculations for the WZ $\text{Al}_x\text{In}_{1-x}\text{P}$ alloy now lead to an excellent agreement with the experimental data. This result suggests therefore that the loss in luminescence at room temperature in the samples with higher Aluminum fraction might be due not only to lack of passivation, but also to scattering of carriers into the indirect M minimum, leading to enhanced non-radiative recombination. Based on the oscillator strength calculations in Fig.5.19b, we see that the probability of radiative recombination decreases by more than a factor of 4 with increasing Aluminum fraction, from $x=0$ to $x=0.5$. Therefore, it is possible that the ratio between radiative and non-radiative recombination decreases, leading to the decrease in photoluminescence intensity and I_{300K}/I_{4K} ratio. However, in Fig.5.16 we have seen that the brightness of WZ $\text{Al}_x\text{In}_{1-x}\text{P}$ was comparable to WZ InP, therefore the decrease in oscillator strength might not play a larger role than the expected increase in surface recombination.

Based on our results, we can conclude that all the photoluminescence emission observed experimentally originates from the direct-allowed $\Gamma_{7C} - \Gamma_{9V}$ transition of the WZ $\text{Al}_x\text{In}_{1-x}\text{P}$ band gap. WZ $\text{Al}_x\text{In}_{1-x}\text{P}$ is therefore suitable for appli-

cations in light emitting diodes between the infrared and green range.

5.4 Conclusions

In this work we have developed the catalyst-free selective area epitaxy of WZ $\text{Al}_x\text{In}_{1-x}\text{P}$ nanowires with $0 < x < 0.4$, achieving efficient light emission in the range between 850nm (1.45eV) in the near-infrared region, to 555nm (2.23eV) in the green region. We attributed the emission to the $\Gamma_{7C} - \Gamma_{9V}$ direct-allowed band gap transition, as we did not find any sharp change in emission behavior as a function of composition, contrary to what we observed in Chapter 4 for WZ $\text{In}_x\text{Ga}_{1-x}\text{P}$. Comparing the experimental data with a DFT theoretical model, we have formulated the hypothesis that the elemental arrangement, and in particular phenomena of ordering of Aluminum and Indium in the lattice, modify the band structure and allow WZ $\text{Al}_x\text{In}_{1-x}\text{P}$ with $x > 0.25$ to emit efficiently. Future work should be focused on proving this hypothesis, for example through detailed TEM or Atom Probe Tomography (APT) studies. We have developed our nanowires on ZB InP (111)A substrates, but it should be possible to grow the same nanostructures on Silicon substrates. Such a development might have an impact on light emitting diodes, which are commonly grown on expensive III-V substrates. WZ $\text{Al}_x\text{In}_{1-x}\text{P}$ nanowires can therefore lower the cost of LEDs in the infrared to green region of the spectrum. As we saw in Chapter 1, nanowires possess also other advantages in terms of light outcoupling and junction area, making WZ $\text{Al}_x\text{In}_{1-x}\text{P}$ nanowires ideal for practical applications. In Chapter 9 we will discuss these results and draw a realistic business model, which might serve as a guideline for future innovations in light emitting diodes.

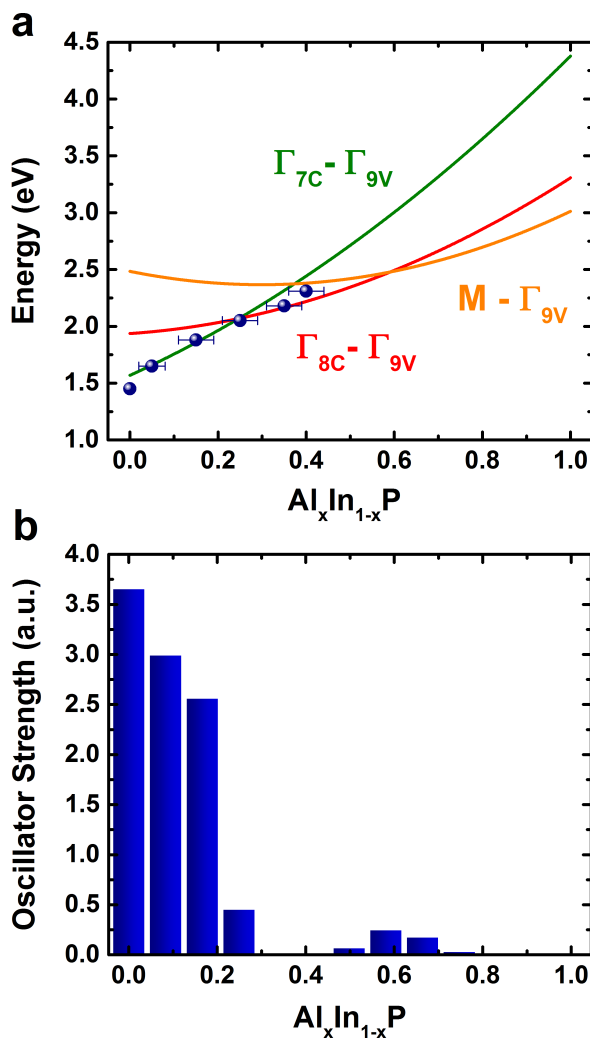


Figure 5.18: (a) Optical transitions in WZ $\text{Al}_x\text{In}_{1-x}\text{P}$ as a function of composition. Lines: DFT calculated. Green: $\Gamma_{7C} - \Gamma_{9V}$, red: $\Gamma_{8C} - \Gamma_{9V}$, orange: indirect transition $M - \Gamma_{9V}$. Circles: PL emission. The emission properties of the samples with $x \leq 0.25$ were found to be in line with a Γ_{7C} -type behavior instead of the predicted Γ_{8C} -type behavior. (b) DFT-calculated conduction band minimum - valence band maximum (CBM-VBM) transition oscillator strength of WZ $\text{Al}_x\text{In}_{1-x}\text{P}$ as a function of composition. The oscillator strength reaches zero at the $\Gamma_{7C} - \Gamma_{8C}$ crossover. This is however in contradiction with the experimental data.

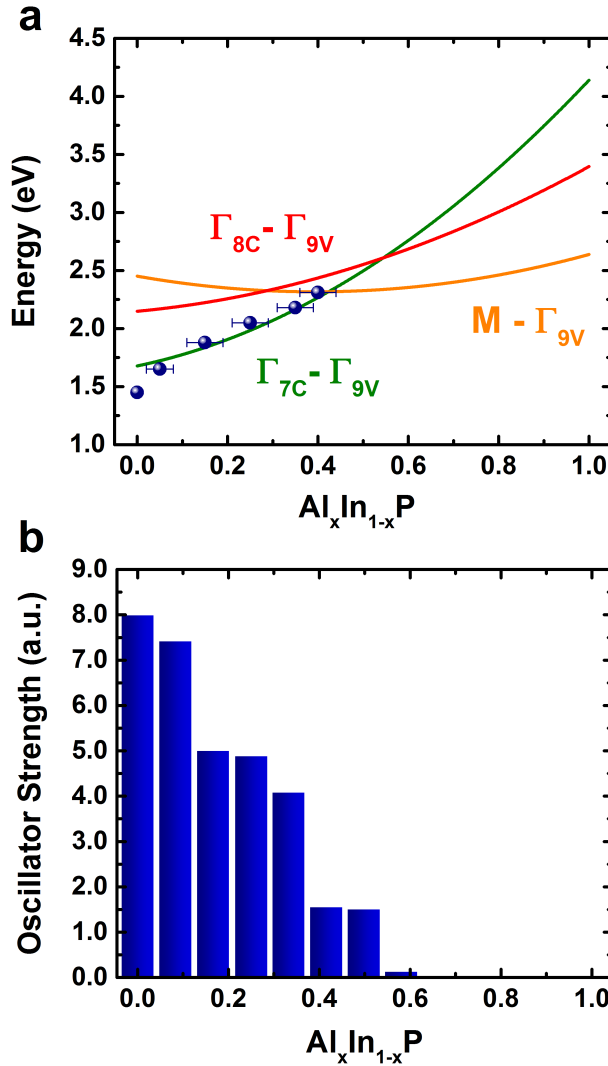


Figure 5.19: (a) Optical transitions in WZ Al_xIn_{1-x}P as a function of composition. Lines: DFT calculated. Green: $\Gamma_{7C} - \Gamma_{9V}$, red: $\Gamma_{8C} - \Gamma_{9V}$, orange: indirect transition $M - \Gamma_{9V}$. Circles: PL emission. Theoretical and experimental data reach excellent quantitative agreement, as all our experimental datapoints are related to the $\Gamma_{7C} - \Gamma_{9V}$ transition. (b) DFT-calculated conduction band minimum - valence band maximum (CBM-VBM) transition oscillator strength of WZ Al_xIn_{1-x}P as a function of composition. The oscillator strength reaches zero around $x = 0.5$, a result which is consistent with the experimental photoluminescence data.

Chapter 6

Understanding the origin of bending in wurtzite GaP/InGaP core-shell nanowires

Nanowires have emerged as a promising platform for the development of novel heterostructures inaccessible in bulk material. However, although nanowires allow for an advanced strain management, the growth of high quality lattice mismatched heterostructures is still a relevant challenge. Numerous recent studies are investigating the elastic properties of nanowires^{78;79}, with the attention recently focused also on their bending properties^{80;81;82}. Here we study the asymmetry-induced bending of wurtzite GaP/In_xGa_{1-x}P core-shell nanowires with transmission electron microscopy and energy dispersive x-ray spectroscopy. We compare the experimental data with finite element method simulations, modeling the entire nanowires with good agreement with the experiment. Starting from this case study, we expand our theoretical predictions to a generalized model valid for all core-shell nanowire lattice mismatched heterostructures. Our work provides understanding on a wide range of heterostructured core-shell nanowire systems and the processes that lead to bending in a core-shell nanowire.

⁰Contributions to this work: Dr. M.A. Verheijen (Philips Innovation Services) performed the TEM analysis, M. Albani and Prof. L. Miglio (Università Milano-Bicocca) performed the FEM simulations.

6.1 Single nanowire case study

The structure of the WZ GaP/ $\text{In}_x\text{Ga}_{1-x}\text{P}$ nanowires has been studied with TEM and Finite Element Method (FEM) simulations, to compare our experimental observations with a theoretical model in order to understand the bending of these nanostructures. The FEM simulations have been performed by M. Albani and Prof. L. Miglio (Università Milano-Bicocca). In Fig.6.1 we show SEM images of WZ GaP/ $\text{In}_x\text{Ga}_{1-x}\text{P}$ core-shell nanowires with core diameter of 100nm and a shell of about 40nm, grown with the method illustrated in Chapter 4, which show clear bending. The nanowires are bent in different directions, with apparently no preferential orientation. Some nanowires are bent in two different directions, resulting in an S-shape, which indicates an asymmetry which not only develops radially, but also changes along the length. As the shell is lattice-mismatched with the core, such bending should be caused by some asymmetry in the shell, which in turn generates an asymmetric strain condition. This asymmetric strain condition is enough to cause bending up to 20° . A simple SEM observation is not enough to gain insight on the structure of the nanowires and understand the origin of bending. We therefore analyze the nanowires with TEM.

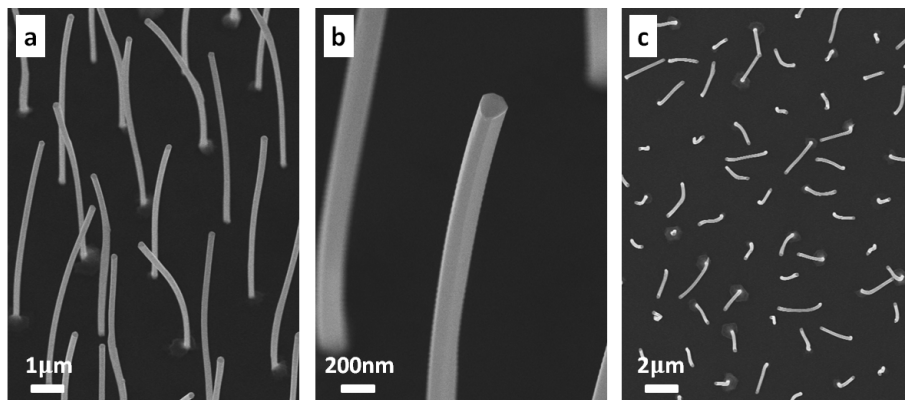


Figure 6.1: SEM images of WZ GaP/ $\text{In}_x\text{Ga}_{1-x}\text{P}$ core-shell nanowires grown on a ZB (111) GaP substrate. (a) SEM image taken at 30° tilt, showing the clear bending of the nanowires. The nanowires exhibit different degrees of bending, in some cases being bent in two different directions, forming an S-shape, suggesting asymmetry in the core-shell structure developing not only radially, but also axially along the nanowire length. (b) Close-up of a bent WZ GaP/ $\text{In}_x\text{Ga}_{1-x}\text{P}$ core-shell nanowire. (c) Top-view SEM image, showing the different bending directions of the nanowires. The degree of bending and the orientation seem to be mostly randomized.

We studied several WZ GaP/ $\text{In}_x\text{Ga}_{1-x}\text{P}$ nanowires with TEM as shown in

Fig.6.2. In Fig.6.2a we show the HAADF image of a nanowire, clearly demonstrating a strong bending. We see that the wire has two sections, one thicker and one thinner. Knowing that our WZ GaP nanowires are untapered (see Chapter 4), we deduce that the difference in thickness is caused by the $\text{In}_x\text{Ga}_{1-x}\text{P}$ shell. As to the origin of such difference, the thicker part of the nanowire corresponds to the lower section, therefore we speculate that a larger amount of material reached the bottom of the nanowire than the top due to surface diffusion on the substrate. This diffusion likely provided additional material to a portion of the nanowire already subject to a certain asymmetry, in this case located in the bottom section, enhancing the phenomenon. The formation of a bottom thicker section in nanowires due to surface diffusion of adatoms from the surroundings of the nanowire is a common and well-investigated phenomenon^{83;84;85} (see also Chapter 8).

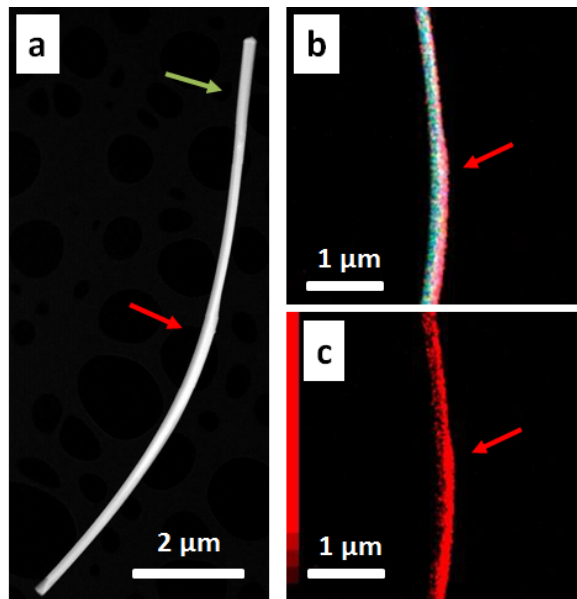


Figure 6.2: (a) HAADF image of a WZ GaP/ $\text{In}_{0.2}\text{Ga}_{0.8}\text{P}$ (average composition) core-shell nanowire. The nanowire is bent due to strain, given by the lattice mismatch between core and shell. The difference in thickness between the upper and lower section of the nanowire are likely given by a larger flow of material in the lower section due to surface diffusion on the substrate. (b-c) EDS color map of the same nanowire, demonstrating the difference in thickness and composition between the two sections of the nanowire. In (b) we show the signals of both Gallium (green) and Indium (red), while in (c) we show only the Indium signal to underline the thickness asymmetry.

In Fig.6.2b-c we show EDS maps in which we can directly observe the thickness and composition of the two sections of the nanowire. The arrows indicate the points of the nanowire where we report detailed EDS linescans, as shown in Fig.6.3. In the inset of each plot we show the precise area of the nanowire where the linescan was taken. The lower apparent Indium concentration in the center of the nanowire is due to the small thickness of the shell, which causes a relevant portion of the core to be probed during the measurement, leading to an underestimation of the Indium content. The linescan is more reliable when only (or mostly) the shell is being probed by the electron beam, which happens at the two sides of the nanowire. We notice some relevant differences between the two sections of the nanowire. First of all, we confirm that the thickness difference is due to the shell itself: in the upper section the shell is approximately symmetric with a thickness of 40nm on either side. In the bottom section instead the shell shows strong thickness asymmetry, with about 80nm of thickness on the convex side of the nanowire and only about 10nm on the concave one. We notice that the composition of the shell follows the same trend, with the upper section being symmetric within the experimental uncertainty ($\pm 3\%$), while the bottom section of the nanowire shows a strong compositional asymmetry between the two sides. The Indium content in the shell also tends to increase radially, as it is clear in the bottom section. This is likely due to the progressive relaxation of the shell, which is able to accommodate material with larger lattice parameter, while accumulating lower elastic energy. We summarize the experimental data in Table 6.1. From these results we can understand the cause of bending in the nanowire: the higher Indium content on one side of the nanowire causes the shell to have larger lattice parameter on one side compared to the other. Furthermore, the thickness asymmetry contributes to increase the strain in the same direction. The two effects, summed together, give rise to the bending. Our hypothesis is that the asymmetry is due to diffusion of material during the growth. Due to the lattice mismatch, elastic energy is accumulated during epitaxial growth of a pseudomorphic layer, therefore the material tends to minimize this energy by accumulating preferentially on one side of the nanowire, where it can relax more strain due to the lower contact surface with the shell. Compositional and thickness asymmetry are therefore very likely related, as each one tends to induce a favorable condition for the development the other asymmetry phenomenon. This mechanism appears to happen in almost all nanowires, as we have seen in Fig.6.1. This might be due to the fact that such migration mechanism might be triggered by a random event, for example the formation of an island on the surface of the WZ GaP core, or by some nanometric roughness caused by the Au catalyst etching. Once the event happens in a random position on the surface of the core, the asymmetric shell growth is triggered, thus resulting in a random bending degree and orientation. The S-shaped nanowires might be then caused by two of these events happening

independently in distant points of the core.

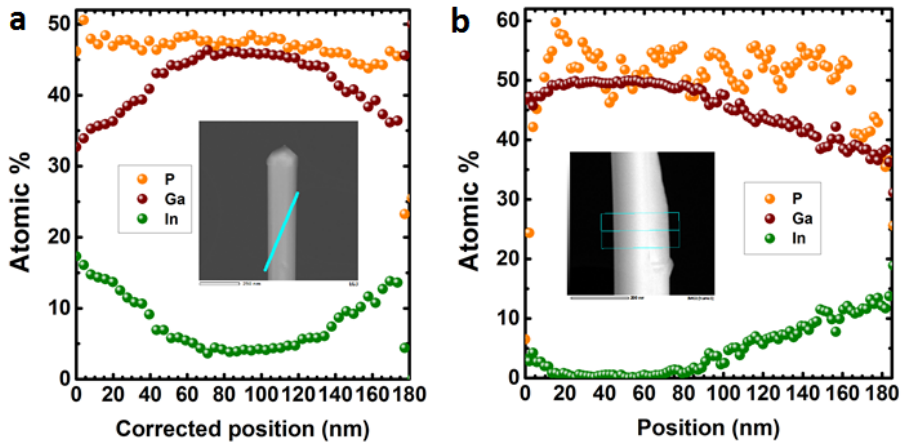


Figure 6.3: EDS linescans of the WZ GaP/In_{0.2}Ga_{0.8}P core-shell nanowire. The insets indicate the positions where the measurements were taken, where (a) is across the top section of the nanowire, (b) across the bottom section. We notice that the upper section of the nanowire is approximately symmetric, both in thickness and composition, while the bottom section shows both strong thickness and composition asymmetry.

	Thickness left side	Indium fraction left side	Thickness right side	Indium fraction right side
Top section	40±5nm	0.30±0.04	35±5nm	0.28±0.04
Bottom section	10±5nm	0.10±0.04	80±5nm	0.22±0.04

Table 6.1: Structural parameters of the WZ GaP/In_xGa_{1-x}P core-shell nanowire shown in the previous figures, obtain by TEM analysis. We report the thickness and the composition of the In_xGa_{1-x}P shell on either side of the nanowire. The resulting asymmetries cause the bending of the nanowire. We see that the asymmetry is more prominent in the bottom section, which corresponds with the previously shown TEM images.

In order to understand the strain distribution in the nanowire, we modeled the WZ GaP/In_{0.2}Ga_{0.8}P core-shell nanowire with Finite Element Method (FEM) simulations using COMSOL Multiphysics software, performed by M. Albani (Universita' di Milano-Bicocca). In FEM simulations we define a three-dimensional model of the nanowire (the "mesh") and subdivide it in smaller domains where the

elastic calculations are carried out. We choose the structure to be an untapered single core-shell nanowire with hexagonal cross section, as shown in Fig.6.4. In order to perform the simulations, some assumptions are needed: the WZ $\text{In}_x\text{Ga}_{1-x}\text{P}$ alloy has never been studied in detail before, therefore no structural information about it is available in literature, to the best of our knowledge. The lattice constants of WZ GaP and WZ InP are indeed available^{86;87}, therefore we assume that the lattice constant of WZ $\text{In}_x\text{Ga}_{1-x}\text{P}$ follows the empirical Vegard's law⁸⁸ for alloys, where it varies linearly with composition between the two extremes, represented by the lattice constants of the binaries. As WZ $\text{In}_x\text{Ga}_{1-x}\text{P}$ has never been studied, also its elastic constants are unknown, without which elastic calculations are evidently not possible. The elastic constants for ZB $\text{In}_x\text{Ga}_{1-x}\text{P}$ cannot be used, as the WZ crystal structure, being hexagonal, has a lower symmetry than the cubic structure, therefore needs more elastic constants. Such constants have however been predicted from pseudopotential calculations^{89;90}, allowing us to use them for the present calculations. In Fig.6.4 we show the concept of the strained core-shell nanowires considered in this study. The shell is asymmetrical in thickness and causes bending of the entire nanowire due to the asymmetric strain condition in the shell. In Fig. 1b-c we show the two types of asymmetry considered. First, thickness asymmetry, which we model as a core displacement respect to the center of the shell. Due to the different thickness, the two sides of the shell will store a different amount of elastic energy, higher on the thicker side. The thicker side of the shell will then tend to bend the nanowire towards the thinner side. Second, we consider compositional asymmetry, where the composition varies linearly across the shell, around an average value. The lattice constant of the crystal is related to the composition, therefore the side of the shell with the higher lattice constant will bend the nanowire towards the side with the lower lattice constant.

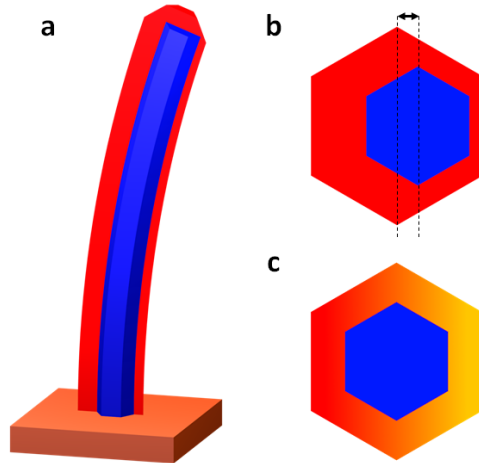


Figure 6.4: Schematic concept drawing illustrating the structure of the studied nanowires. (a) WZ GaP/In_xGa_{1-x}P core-shell nanowire. Blue: WZ GaP core. Red: WZ In_xGa_{1-x}P shell. The nanowire is bent due to asymmetry in the shell, which can be of two types. (b) Illustration of thickness asymmetry, which we model as a displacement of the core respect to the center of the shell. (c) Illustration of compositional asymmetry, where the orange side represents a lower Indium composition than the red side. We model the composition as varying linearly between the two sides.

In Fig.6.5 we show the result of the simulation, where we overlay the FEM model over the TEM image, obtaining excellent agreement. We modelled the displacement of the core as linearly varying across the length of the nanowire, as shown in Fig.6.5b. Regarding the total thickness, we selected a model divided in three parts: a $3.5\mu\text{m}$ long top part with 180nm of thickness, a $5.5\mu\text{m}$ long lower part with 190nm of thickness and a $1\mu\text{m}$ long central section connecting the two, with linearly varying thickness in order to avoid surface discontinuities in the simulation. The composition of the shell was the one listed in Table 6.1, with intermediate composition selected for the central segment. In Fig.6.5c we show the hydrostatic strain in the nanowire by displaying three bidimensional cross sections, corresponding to the three different segments. We can see that in all cases the core is in average tensilely strained (red color), while the shell is in average strained compressively (blue). The distribution of the strain changes across the length of the nanowire, passing from a substantially symmetric distribution in the top to a strong asymmetry in the bottom section. Also the core is affected by the asymmetry, and even shows compressive strain on the concave side of the bottom section. We notice that the shell on the convex side of the

bottom section shows very little strain, being almost completely relaxed in its last 20nm closer to the surface. On the other hand, the opposite side of the shell is very strongly compressed. The same behavior is visible in the central section, although less pronounced. From these results we conclude that the strain conditions and consequent bending are directly connected to the asymmetry in the shell.

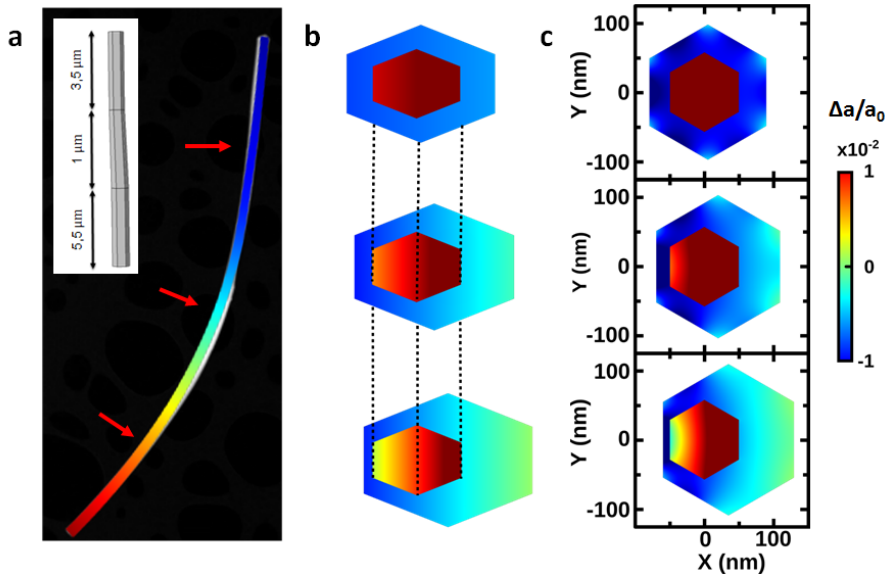


Figure 6.5: (a) Comparison between FEM simulation and TEM HAADF image of the WZ GaP/In_{0.2}Ga_{0.8}P core-shell nanowire. The inset shows the three sections used for the FEM simulation. The central section was used to avoid surface discontinuities in the model. (b) Plots of the axial strain in the three sections of the nanowire, to illustrate the variation of the displacement of the core as a function of the length of the nanowire. (c) Hydrostatic strain plots in the three sections of the nanowire. The degree of asymmetry in the shell clearly affects the asymmetry in strain distribution. In the bottom section, the left side of the core is subject to compressive strain, while the right side is almost completely relaxed. Only elastic relaxation is considered in the simulation.

6.2 Systematic study of the shell asymmetry

We now want to understand the relation between the asymmetry and bending in a systematic way, considering also the influence of the core diameter on the bending. We therefore calculate the nanowire curvature as a function of core diameter and total shell thickness (the sum of left and right side thickness) using FEM simulations, for WZ GaP/In_xGa_{1-x}P nanowires with average Indium fraction $x=0.25$. The simulated nanowires have a compositional asymmetry of $x=0.05$, therefore at opposite facets have Indium fraction $x=0.20$ and $x=0.30$. The thickness is also asymmetric, with a core displacement equal to 1/4 of the shell thickness. The results are shown in Fig.6.6a. In Fig.6.6b we report three curves for core-shell nanowires with three core diameters, from the data in Fig.6.6a. The colors are shown to facilitate the comparison between the two plots. We see that the curvature is highest for core-shell nanowires with thinner core. This is due to the fact that a thinner core is more easily bent by a shell, as it requires less elastic energy. We also notice that, given a fixed diameter, the curvature of the nanowire depends on the total shell thickness. For small thickness the bending is intuitively smaller, then it rises up to a maximum, to finally decrease with increasing thickness. This is due to the fact that the elastic energy needed to bend the nanowire increases with increasing total nanowire thickness, therefore a larger degree of asymmetry is needed to bend a thicker nanowire than a thinner one. Our aim is then to use this simulation method to develop a diagnostic tool for the shell asymmetry of nanowires which show bending. We do so by collecting the structural parameters of a number of nanowires using TEM, as shown in Fig.6.7a and reported in Table 6.2. We compare these data on the shell asymmetry with FEM simulations, obtaining the results displayed in Fig.6.7b-c. The experimental datapoints are reported as colored squares, where the sides represent the uncertainty, while the color represents the curvature, using the same scale as the graph. As we can see from both Fig.6.7 and Table 6.2, the simulation and the experimental data reach an excellent agreement, proving FEM calculations as a very accurate predicting tool for the degree of shell asymmetry in a lattice mismatched core-shell nanowire. As the simulations did not consider plastic relaxation, we can conclude that defectivity does not play an important role in these nanowires, with a contribution within the experimental uncertainty.

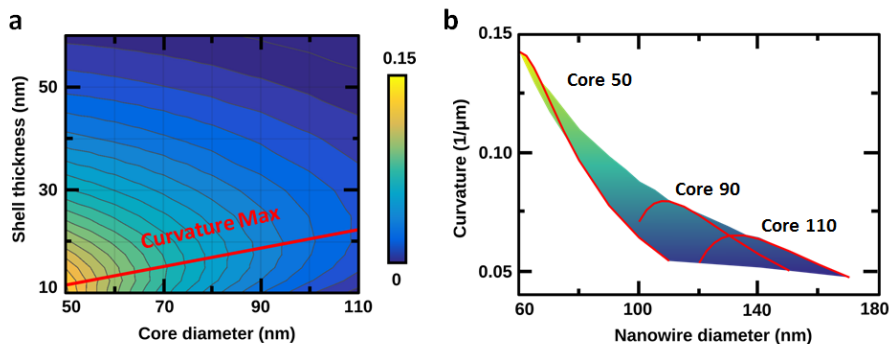


Figure 6.6: (a) Calculated curvature of a WZ GaP/In_xGa_{1-x}P core-shell nanowire as a function of the shell thickness and core diameter. The average composition is fixed to be equal to $x=0.25$, with a constant asymmetry of ± 0.05 . The core shift is equal to $1/4$ of the shell thickness. The scalebar indicates the nanowire curvature in $1/\mu\text{m}$ units. (b) Nanowire curvature as a function of the total nanowire diameter, based on the data from panel (a). The color coded area conserves the scale from (a) and is used only to facilitate the comparison. The trend does not depend only on the total nanowire diameter, but also on the core diameter. The plot of the curvature for three fixed core diameters is outlined by the red curves.

6.3 Conclusions

In this work we investigated the origin of bending in WZ GaP/In_xGa_{1-x}P core-shell nanowires and developed a predictive tool to estimate the asymmetry of a core-shell nanowire structure. By measuring the bending in a nanowire, for example with scanning electron microscopy (SEM), we cannot determine exactly the asymmetry in shell thickness and composition, but we can accurately determine an ensemble of possible cases, thus defining a certain "degree of asymmetry" as a combination of thickness and composition inhomogeneity which produces a certain curvature radius in the nanowire. As the curvature is due to inhomogeneity, such condition should be avoided in those applications, for example quantum wells, where homogeneity is required. An asymmetry in the composition of a quantum well in fact promotes the diffusion of carriers in the portion with lower band gap, changing the average emission energy of the quantum well in an undesired and uncontrolled way and promoting detrimental phenomena which happen at high carrier concentration, such as Auger non-radiative recombination. A thickness asymmetry leads to the obvious disadvantage of rendering the quantum well confinement effect non homogeneous, thus increasing the Full Width at Half Maximum (FWHM) of its emission. As we conclude that the

asymmetry is strain-driven, and in particular lattice mismatch-driven, the strategy we propose to avoid bending is to grow a graded buffer shell with composition changing from the same as the core to the desired final composition. In this way one can allow a gradual elastic strain relaxation due to the nanowire geometry, thus avoiding the strain-driven effects that lead to inhomogeneity. Due to this elastic relaxation in the buffer shell, it should be possible to avoid the nucleation of misfit dislocations, giving nanowires a definite advantage over planar geometry in hosting lattice-mismatched heterostructures. This work has been developed on WZ GaP/In_xGa_{1-x}P core-shell nanowires, but can in principle be extended to any kind of core-shell nanowire system, provided that the elastic constants of the materials are known, or realistic values can be assumed, like in our case. Core-shell nanowires are of great interest due to the possibility of fabricating heterostructures, such as quantum wells, which might be lattice mismatched^{81;91;92}. In such cases a diagnostic tool for quickly estimating the degree of asymmetry of nanowires, avoiding time and resource-consuming TEM studies, can be of great help. Recently, semiconductor nanowire-superconductor heterostructures have gained great attention due to applications in quantum computing and majorana physics. These systems often see the asymmetric integration of very dissimilar materials with different lattice constants, leading to systems subject to strain-driven bending^{93;94}.

Nanowire	Average Indium fraction	Shell thickness	Core shift	Composition asymmetry	Measured (predicted) curvature (1/ μm)
1	0.27 \pm 0.03	32 \pm 5nm	6 \pm 4nm	0.04 \pm 0.03	0.05 \pm 0.01 (0.05)
2	0.26 \pm 0.03	42 \pm 5nm	12 \pm 7nm	0.06 \pm 0.03	0.06 \pm 0.01 (0.06)
3	0.24 \pm 0.03	47 \pm 5nm	7 \pm 3nm	0.03 \pm 0.01	0.02 \pm 0.01 (0.02)
4	0.58 \pm 0.03	170 \pm 5nm	17 \pm 7nm	0.04 \pm 0.01	0.02 \pm 0.01 (0.02)
5	0.61 \pm 0.03	155 \pm 5nm	35 \pm 5nm	0.07 \pm 0.01	0.04 \pm 0.01 (0.06)

Table 6.2: Experimental data gathered with TEM from the WZ GaP/InGaP core-shell nanowires considered in this study. We also compare the measured curvature with the curvature predicted by the FEM simulations. These results are visualized in Fig.6.7.

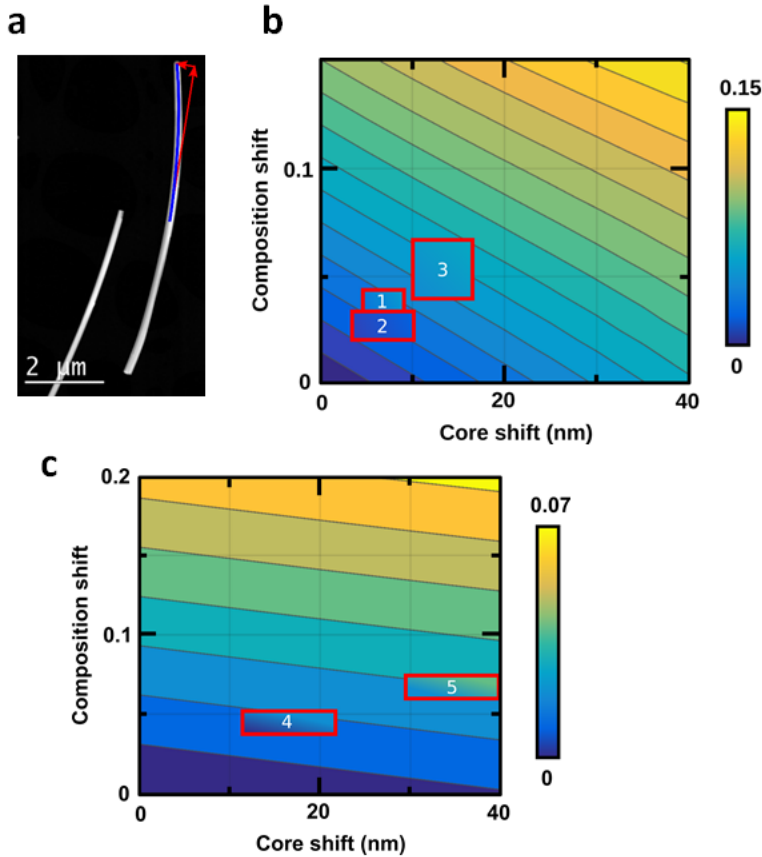


Figure 6.7: (a) HAADF image of two WZ GaP/In_xGa_{1-x}P nanowires grown under the same conditions, clearly showing bending. The curvature is measured by interpolating the nanowire geometry with a parabola (blue line) and by computing the second derivative of this function in the center of the nanowire. The red arrows are a guide to the eye to indicate the bending-induced displacement of the tip compared to the center of the nanowire. (b-c) Calculated curvature of WZ GaP/In_xGa_{1-x}P nanowires as a function of average shell thickness, with overlaid experimental data (red rectangles). The numbers refer to Table 6.2. The scale bar represents the curvature in 1/μm. The size of each red rectangle represents the experimental error on the two axis dimensions. The color gradient in the rectangle represents the error on the experimental curvature. Parameters: (b) Core 100nm, shell 50nm, average x=0.25. (c) Core 100nm, shell 160nm, average x=0.60. The comparison between calculated and experimental data yields very good agreement.

Chapter 7

Growth of atomically sharp homointerfaces in GaP nanowires

A major goal in the field of quantum photonics is to fabricate sources which can reliably emit identical photons⁹⁵. The growth of heterostructured quantum structures finds a challenge in the realization of sharp interfaces: variations between each quantum structure leads to a spread in emission wavelength⁹⁶. Nanowires have recently opened the way to homostructures, namely confinement structures realized with one single material: the confinement is obtained by exploiting a controlled phase switching between two crystal structures with a favorable band alignment, which can behave as single photon sources for quantum photonics^{97;98}. In the WZ/ZB GaP system, electrons and holes will be confined in WZ because of the type I band alignment with ZB²⁶. Large polarization fields are predicted for WZ²⁶, therefore by tuning the thickness of an embedded ZB segment one can tune the resulting polarization field across it, producing a controllable shift in the emitted photoluminescence, in analogy for what has been reported for GaN⁹⁹. Here we demonstrate controlled crystal phase switching between the zincblende and wurtzite phases of GaP nanowires, with a control extending almost to the monolayer (ML) level³. This system can be used in the future for crystal phase quantum well emission of entangled photons.

⁰Contributions to this work: Dr. S. Assali (TU/e) for epitaxy, Dr. M.A. Verheijen (Philips Innovation Services) performed the TEM analysis, Dr. L.-F. Feiner (TU/e) performed the theoretical modeling.

7.1 Growth of WZ/ZB homostructures

The patterned arrays of 100nm diameter GaP nanowires are defined by nanoimprint lithography. The final result is shown in the SEM image in Fig.7.1a. A scheme of the crystal phase homostructures is shown in Fig. 7.1b, with WZ in blue, ZB in red, the Au catalyst droplet in yellow, the ZB (111)B GaP substrate in orange.

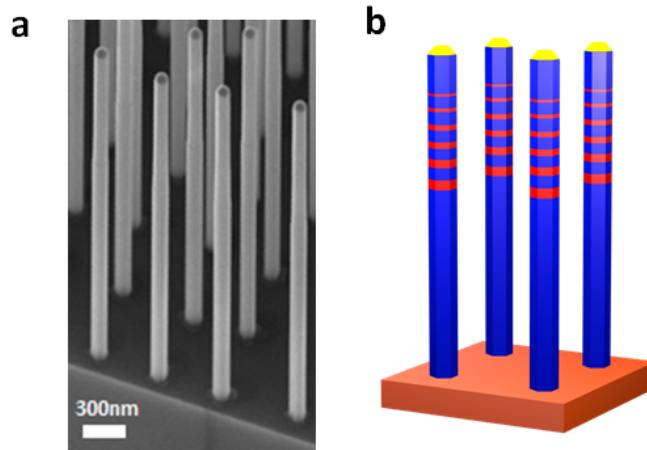


Figure 7.1: (a) SEM image of the GaP nanowire array grown on the nanoimprinted pattern. (b) Schematic of the crystal structure of the GaP nanowires. Blue: wurtzite. Red: ZB. Yellow: Au catalyst droplet. After growth of the WZ stem several ZB segments are grown along the nanowire, alternating with WZ segments.

The nanowires are grown using a multi-step protocol. First, a $2.5\mu\text{m}$ WZ stem is grown at 615°C using TMGa, PH_3 and HCl, with a V/III ratio of 23 as reported in Chapter 4 and Ref.⁵. The growth is then stopped by closing the TMGa and HCl flux, while still providing PH_3 to prevent the nanowires from melting or evaporating by losing phosphorous to the gas phase. The temperature is reduced to 490°C , while the PH_3 flow is increased to increase the V/III ratio. When the temperature becomes stable, the TMGa is opened for a short time (t_{ZB}) to allow growth using a V/III ratio of 67. HCl is not used during ZB growth. After t_{ZB} , the TMGa flux is closed again and the temperature is raised to the original 615°C , while the PH_3 flow is reduced to reach the previous V/III ratio of 23. A new WZ segment can now be grown by reopening the TMGa and HCl flux, allowing the repetition of the protocol.

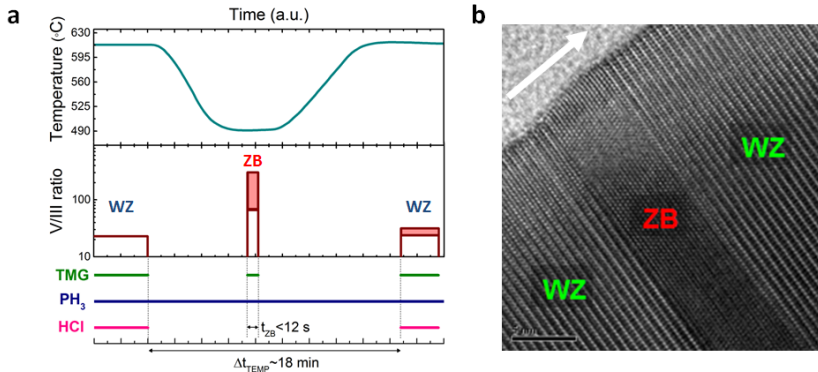


Figure 7.2: (a) In situ temperature profile, V/III ratio, and sketch of the supply of the precursor gases during growth. The dark red shaded area indicates the range of the V/III ratios used in this work. The time interval t_{ZB} has been enlarged for better comparison with t_{WZ} . (b) HR-STEM bright field image of a WZ GaP nanowire with a ZB segment. The arrow indicates the nanowire growth direction.

7.2 Zincblende growth control

The process is repeated several times with varying t_{ZB} , in order to grow ZB segments of different length, while maintaining a fixed WZ growth time ($t_{WZ} = 90\text{s}$). The final result of a t_{ZB} series from 3.1s to 0s is shown in the TEM bright field image of Fig. 7.3a. Notably, the only ZB inserts present have been introduced in a controlled way and the nanowire is devoid of stacking faults. In Fig. 7.3b-c we report STEM images of the ZB segment with $t_{ZB} = 3.1\text{s}$ and $t_{ZB} = 1.5\text{s}$, which demonstrate the crystal purity of the ZB segments. The side-walls of the ZB segments are tilted compared to the nanowire axis. As mentioned in Chapter 2, ZB develops $\{111\}$ A or B facets, which are tilted, opposed to the $\{10\bar{1}0\}$ facets of WZ, parallel to the nanowire axis¹⁰⁰. In order to observe the dependency from precursor flows, we varied TMGa and PH_3 during ZB growth: while the growth rate was found to be insensitive to the PH_3 flow, the growth rate varied considerably with the TMGa flow, indicating a Ga-limited growth regime. In Fig. 7.3d we show the length of the ZB segments as a function of t_{ZB} and TMGa flow (color-coded numbers, Unit: 10^{-5} molar fraction).

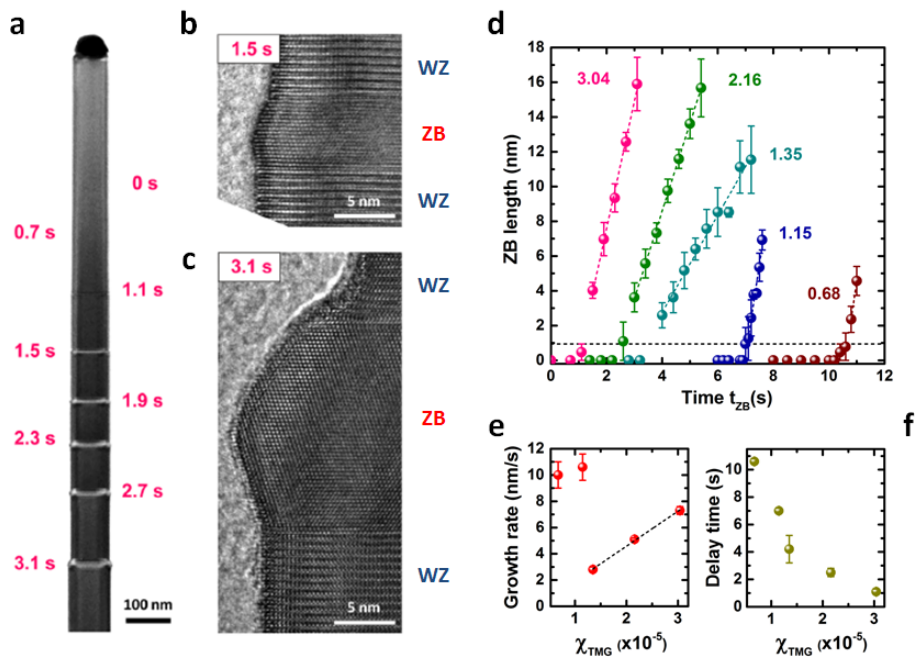


Figure 7.3: (a) TEM bright field image of a nanowire with ZB segments grown for a variable time t_{ZB} , separated by WZ segments grown for a fixed time $t_{WZ} = 90s$ ($\chi_{TMGa} = 3.04 \cdot 10^{-5}$). (b-c) HR-STEM images of the nanowire in (a) for ZB segments grown for $t_{ZB} = 3.1s$ (b) and $t_{ZB} = 1.5s$ (c), showing defect-free crystal phases with atomically sharp interfaces. (d) Length of ZB segments as a function of the Ga supply time t_{ZB} for different TMGa molar fractions χ_{TMGa} , indicated in units of $1 \cdot 10^{-5}$. The dashed horizontal line indicated the shortest stacking sequence for the ZB phase (ABC stacking), which is equal to 0.945nm. (e-f) ZB growth rate R_{ZB} (e) and delay time t_{DEL} (f) as a function of the Ga molar fraction χ_{TMGa} . The error bars in (d-f) refer to a set of four nanowires measured via HR-STEM.

From this figure we can draw two observations, which are in turn summarized in Fig. 7.3e-f. First (e), the ZB growth rate shows a decrease with TMGa molar fraction up to $\chi_{TMGa} = 1.35 \cdot 10^{-5}$ reaching about 3nm/s (7-9 ML/s), then increases to 10nm/s. The initial decrease can be explained simply by the lower Ga flow, which intuitively leads to slower growth. For the increase at very low molar fractions, we speculate that a lower Ga fraction might lead to a higher incorporation of P in the Au droplet, thus leading to an increase in supersaturation, with the effect of increasing the growth rate. Second (f), the ZB

segment starts growing only after a delay time which depends on the TMGa molar fraction, which hints to the necessity of filling the Au droplet with enough Ga, implying a supersaturation condition which needs to be met before the growth can start.

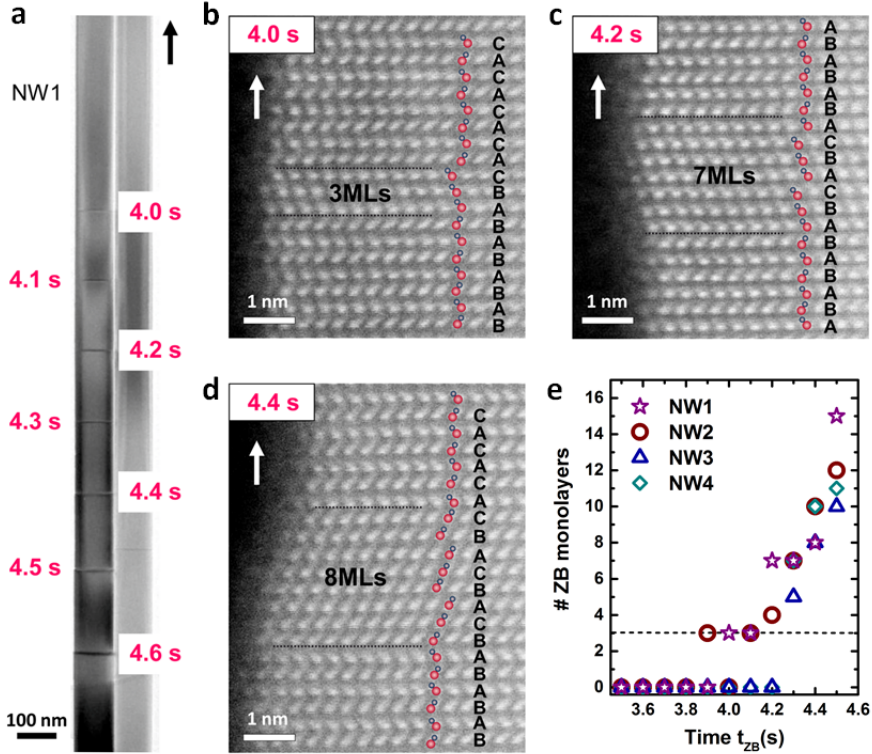


Figure 7.4: (a) TEM image of a nanowire grown using 0.1 s steps for the Ga supply time t_{ZB} and a TMG molar fraction $\chi_{TMGa} = 1.35 \cdot 10^{-5}$. (b-d) HR-STEM images showing controlled ZB segment lengths of 3, 7, and 8 MLs. The red and blue dots indicate the Ga and P atoms, respectively, while arrows indicate the growth direction. (e) Number of ZB monolayers as a function of the Ga supply time t_{ZB} for four different nanowires. The dashed line corresponds to the shortest stacking sequence for the ZB phase in a WZ wire, which has a length of 3 MLs (ABC stacking). The diameters of the four nanowires are in the range 96-106 nm.

We now explore the possibility of obtaining monolayer control on ZB growth in the nanowire: in order to achieve the maximum precision allowed, we use the

TMGa molar fraction that yielded the lowest growth rate, $\chi_{TMGa} = 1.35 \cdot 10^{-5}$. In the nanowire in Fig. 7.4a, we used $4.6s < t_{ZB} < 3.4s$ with 0.1s steps for the time series. In Fig. 7.4b-d we show STEM images of ZB segments of, respectively, 3MLs, 7MLs and 8MLs. We also highlight the stacking for better understanding, also noting that the group-V polar growth direction (B) is maintained when switching between WZ and ZB crystal structures. In Fig. 7.4e we report the thickness in ML of the ZB segments of 4 nanowires. We observe that several monolayers are grown during a 0.1s interval: as this is the resolution limit of our MOVPE reactor, more accurate control cannot be achieved. We predict however that a finer flow switching control, below 0.1s, would be able to achieve the monolayer control. We also observe that in 2 nanowires (NW3,4) the growth starts with 5-7MLs, instead of 3MLs observed for NW1,2. We suppose that wire-to-wire variations, due to fabrication imperfections, might influence the properties of the catalyst droplet, causing different supersaturation conditions, leading to different behavior between nanowires.

7.3 Wurtzite growth control

The formation of WZ has also been investigated, using the same method: fixed ZB segments (10nm) were grown as markers, while the WZ growth time (t_{WZ}) was varied, as shown in Fig. 7.5a. In Fig. 7.5b we show a STEM image demonstrating phase purity of both the ZB and WZ segments. The length of the WZ segments as a function of t_{WZ} are reported in Fig. 7.5c. When a TMGa molar fraction $\chi_{TMGa} = 7.42 \cdot 10^{-5}$ is used, a constant WZ length $L_{WZ} = 7 \pm 3nm$ is observed for all supply times below the offset time $t_{OFF} = 14 \pm 2s$, while beyond this time a linear increase in WZ segment length is observed. When a TMGa molar fraction $\chi_{TMGa} = 5.40 \cdot 10^{-5}$ is used, the offset time rises greatly to $t_{OFF} \approx 100s$. Below this time, WZ segments are present and show the same L_{WZ} as for the previous molar flow. In the inset we show the length of WZ segments as a function of t_{WZ} for a single nanowire, showing the linear increase of the WZ segments length when $t_{WZ} > t_{OFF}$, from which we can extrapolate a growth rate of $R_{WZ} = 2.4 \pm 0.2nm/s$. The variation between the WZ segments for a single nanowire is minimal, contrary to the comparison between different nanowires (the error bars in Fig. 7.5c are obtained by averaging between nanowires), demonstrating the critical role of the Au catalyst pattern uniformity in achieving uniform growth throughout a sample.

From these data we conclude that L_{WZ} is independent both of χ_{TMGa} and t_{WZ} (for $t_{WZ} < t_{OFF}$), and therefore the WZ segment is formed by unwanted WZ growth, that is, growth in the absence of Ga supply, either when the temperature is at 490°C or during a temperature change (increase or decrease) between 490°C and 610°C (see Fig. 7.2). The residual Ga in the Au droplet is able react with

the P still provided and cause growth of this WZ segment of constant length, while regular WZ growth happens only when $t_{WZ} > t_{OFF}$, with t_{OFF} dependent on χ_{TMGa} .

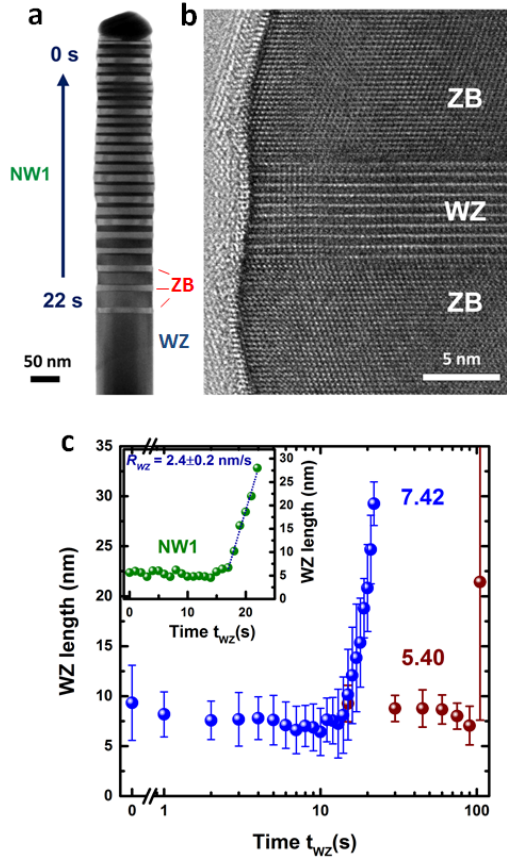


Figure 7.5: (a) TEM image of a nanowire with WZ segments grown for different supply times t_{WZ} using a TMGa molar fraction $\chi_{TMGa} = 7.42 \cdot 10^{-5}$. The ZB segments grown for a fixed time t_{ZB} are used as markers. (b) HR-STEM image showing unintentionally grown WZ in between two ZB segments. (c) WZ length as a function of t_{WZ} for two different TMGa molar fraction χ_{TMGa} , indicated in units of $1 \cdot 10^{-5}$. The error bars refer to a set of four nanowires measured via HR-STEM. Inset: WZ length as a function of t_{WZ} for the nanowire in (a).

7.4 Nucleation model of ZB and WZ

The model used for the understanding of this process is based on the work of Dr. L.F. Feiner and Dr. S. Breuer¹⁰¹. In Chapter 2 we have shown that nucleation in a nanowire grown with Au-assisted VLS method happens at the triple phase line (TPL), corresponding to the rim of the catalyst droplet. We have also shown that when the supersaturation is above a certain critical value $\Delta\mu > \Delta\mu_C$, WZ nucleates as its free energy of nucleation is lower than for ZB ($\Delta G_{WZ} < \Delta G_{ZB}$). In the experiments presented in this Chapter, we have seen that we can switch from pure WZ growth regime, to pure ZB growth regime by lowering the temperature, which is the main driving factor of this switch. However, by lowering the temperature we actually increase the supersaturation, therefore $\Delta\mu_{ZB} > \Delta\mu_{WZ}$, which apparently contradicts our conclusions above. However, when a nanowire is thick enough a new route for ZB nucleation opens: in fact, the number of nucleation centers at the TPL scales with the nanowire radius R , while the number of nucleation centers at the nanowire-catalyst interface scales with R^2 , favoring the latter when a nanowire is thick enough. As our nanowires are approximately 100nm thick, we have to take into account also the possibility of nucleation at the nanowire center (namely, the nanowire-catalyst interface) as a realistic possibility. In this case, only ZB would be nucleated, as this central nucleation equals the nucleation in the bulk case, where the energy of the atomic configuration favors the ZB case (see Chapter 2). Our understanding of crystal phase switch is therefore the following: when lowering the temperature, the supersaturation rises, thus crossing a certain critical supersaturation ($\Delta\mu_{TPL/C}(T)$) which allows us to change the nucleation region from the TPL to the catalyst-droplet interface, where only ZB can nucleate. In this way we can selectively and reproducibly nucleate WZ and ZB, realizing atomically sharp homointerfaces.

7.5 Conclusions

In this work we have developed a method to epitaxially growth atomically sharp crystal phase homointerfaces using WZ GaP nanowires. These systems are particularly promising for quantum optics applications, as the sharpness of typical quantum dots and quantum wells based on heterointerfaces is limited by interdiffusion between the quantum dots/wells and their cladding. One of the main challenges in quantum optics is the generation of identical photons from two separated sources, for example two quantum dots: as we have mentioned, heterostructures suffer from interdiffusion, which smears the confinement potential of the quantum structure and leads to small, but substantial differences from source to source. This challenge might be overcome by the use of crystal phase homointerfaces, which are atomically sharp and not subject to interdiffusion, as

the crystal structure is well defined and stable. The energy of the emission can be designed by selecting the thickness of the crystal phase quantum dot/well with an accuracy down to the single atomic monolayer. In our work we prove that this result is achievable, for example by using a reactor with a gas switching accuracy finer than 0.1s. Differences between the homostructured quantum dots/wells might still be present, for example due to differences in diameter between nanowires, therefore more work is needed in this field in order to realize a perfect emitter. On the other hand, the emission wavelength of a quantum dot can be tuned using electric fields, for example by fabricating gates around the nanowires¹⁰². Future work will be aimed to demonstrate light emission from crystal phase quantum dots/wells in WZ GaP with digital control, therefore controlling the emission by selecting the number of WZ monolayers in the crystal phase quantum dot/well.

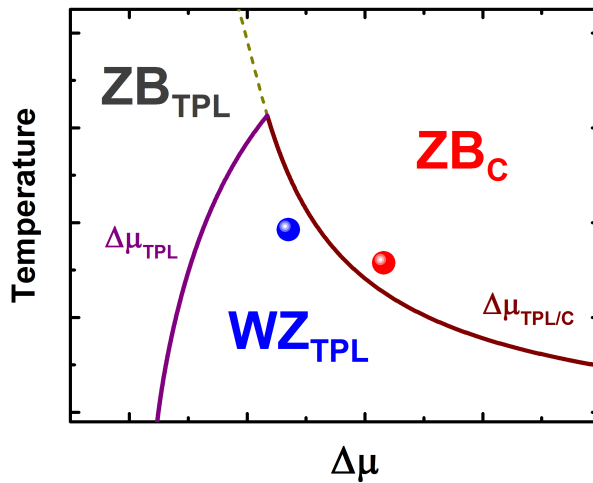


Figure 7.6: Phase diagram temperature- $\Delta\mu$ for nanowire growth according to the nucleation model, including the effect from nucleation sites, according to Ref.^{103;101}. The fields indicate different nucleation mechanisms: nucleation of wurtzite at the triple phase line (WZ_{TPL}), zincblende at the triple phase line (ZB_{TPL}) and zincblende in the center of the catalyst-nanowire interface (ZB_C). In our experiments, by manipulating temperature and supersaturation $\Delta\mu$ and reaching the conditions indicated by the two circles, we can alternate between WZ_{TPL} (WZ nucleated at the triple phase line) and ZB_C (ZB nucleated at the center of the top facet of the nanowire, at the nanowire-catalyst interface).

Chapter 8

Wurtzite GaP nanowires for thermal transport study

More than half of the energy produced at all times is wasted in the form of heat due to the inefficiency of a wide range of processes and devices. Thermal engines, electronics, but also poor thermal management in buildings are major sources of energy waste. Therefore, advances in the understanding of the thermal processes in materials can lead to better thermal management and, ultimately, to more efficient thermoelectric devices^{104;105}. Efficient thermal management is also necessary to maintain devices in the correct temperature range, for example using heat sinks to disperse excess heat, in order to maximize their efficiency^{106;107}. Ballistic phonon transport is the ideal phenomenon on which to base future heat sink technology, as it can provide heat transport without losses^{108;109}. Another important phenomenon for heat management is thermal rectification, which we will introduce further in the chapter. During this work, wurtzite GaP nanowires with a range of diameters from 100nm down to 20nm have been developed to study the thermal transport in this material for the first time. This led to indications of quasi-ballistic transport for diameters below 35nm. We also developed telescopic nanowires, with a variable diameter along their axis, as they are candidates for thermal rectification due to their asymmetric geometry.

⁰Contributions to this work: Dr. M. Swinkels and D. Vakulov (TU/e) performed the device fabrication and thermal transport measurements.

8.1 Thin wurtzite GaP nanowires

In order to achieve small diameters, electron beam lithography is used as described in Chapter 3, as nanoimprint cannot provide diameters below 50-70nm. In order to obtain nucleation of nanowires with diameters smaller than 40nm, the V/III ratio had to be increased by a factor of 5 during the nucleation step and by a factor of 2 during the WZ GaP growth, with respect to the V/III ratio used for nanowires with larger diameter. This might be due to the Gibbs-Thomson effect^{110;111}, where the small diameter of the catalyst droplet causes the supersaturation to be lower than in larger diameters, due to the high surface tension. By increasing the V/III ratio the supersaturation is brought again to an optimal level for nanowire growth. Therefore, we can obtain WZ GaP nanowires with diameter down to about 20nm, as shown in Fig.8.1, ideal to perform a diameter-dependent study of the thermal transport properties of WZ GaP for the first time.

Wire diameter	TMGa molar fraction	PH ₃ molar fraction	V/III ratio
100nm	$7.5 \cdot 10^{-5}$	$1.1 \cdot 10^{-2}$	147
25nm	$1.9 \cdot 10^{-5}$	$3.4 \cdot 10^{-2}$	1789

Table 8.1: Precursor flows and relative V/III ratio used in the nucleation step of WZ GaP nanowires with 100nm and 25nm of diameter.

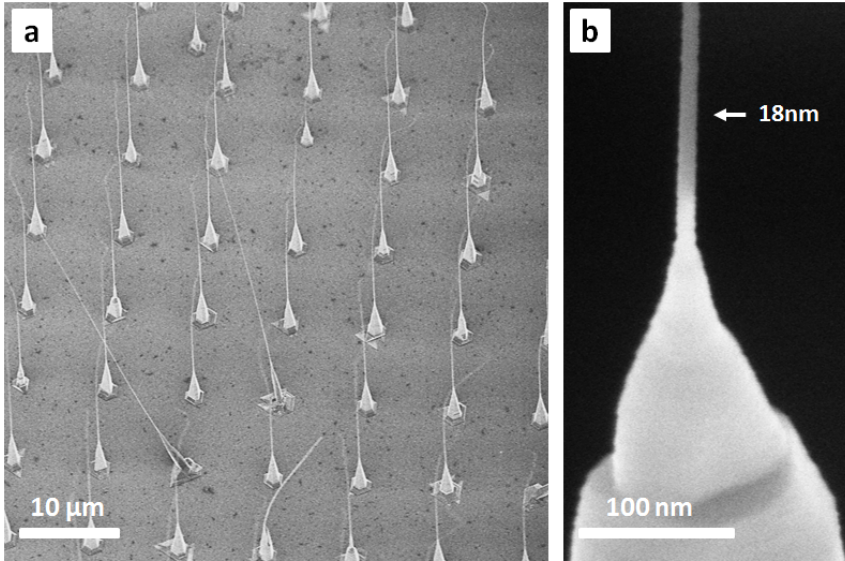


Figure 8.1: Array of WZ GaP nanowires grown on (111)B GaP substrate with VLS mechanism. The diameter of the nanowires is about 20nm, while the pitch of the array is $10\mu\text{m}$. The nanowires show a large pedestal due to accumulation of material during growth. During nanomanipulation, only the thin nanowire will be removed, leaving the pedestal behind.

8.1.1 Quasi-ballistic phonon transport

The aim of the study is to determine the thermal conductivity of WZ GaP nanowires as a function of their geometry, namely diameter and length. The thermal measurements were performed by Dr. M. Swinkels and D. Vakulov. To this purpose we used a thermal bridge microdevice¹¹², which is illustrated in Fig.8.2. The device is based on 0.5mm long suspended SiNx beams to ensure thermal isolation, supporting two membrane platforms with platinum meanders that act both as heaters and thermometers. The nanowire is placed between the two suspended membranes, which are kept at different temperatures. The nanowire acts as thermal contact on either side, bridging a hot area with a cold one and transferring heat through phonons. The temperature difference is measured from the resistance of the platinum meanders, using four point probe technique. In this way the temperature difference as a function of heating power is measured, which can be converted into thermal conductance and, through appropriate geometrical scaling, to the thermal conductivity of the nanowire¹¹².

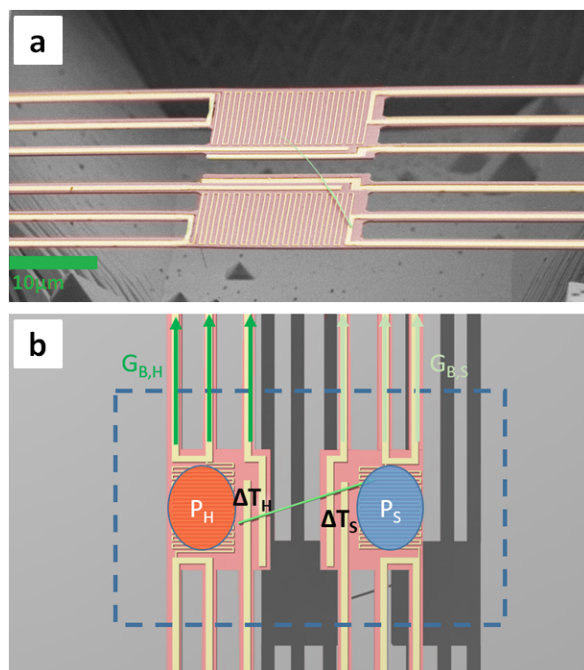


Figure 8.2: (a) False colour SEM image of the suspended bridge microdevice used for the thermal measurements, fabricated by Dr. M. Swinkels and D. Vakulov. Red corresponds to SiN_x, yellow to the platinum stripes and meanders used for thermal control. The nanowire, suspended between the two membranes, is colored in green. (b) Working scheme of the device. The two membranes are kept at two different temperatures, using the platinum stripes as both heaters and thermometers. P_X is the power dissipated, ΔT_H is the temperature difference, G_X is the conductance. The subscript H denotes the heating side, S the sensing side.

The nanowire length dependence of the thermal conductivity is investigated by fabricating a series of devices with different spacing between them. First, the diameter dependence of the thermal conductivity is investigated by measuring nanowires with diameter d in the range 25-140nm, around room temperature. The results are shown in Fig.8.3. The blue curve represents the expected thermal conductivity κ of the nanowires as a function of the diameter d , also taking into account the contact resistance, using the formula^{113;114}:

$$\kappa = \frac{4GL}{\pi d^2} = \kappa_{bulk} \cdot \left[1 - \exp\left(-\frac{d}{\Lambda_0}\right) \right] + C_{contact}d \quad (8.1)$$

where G is the conductance of the nanowire, L and d are respectively the

nanowire length and diameter, κ_{bulk} is the conductivity of bulk ZB GaP ($27 \text{ Wm}^{-1}\text{K}^{-1}$), Λ_0 is the phonon mean free path and $C_{contact}$ is a constant taking into account the interface phonon scattering between the nanowire and the suspended bridge, which causes contact resistance¹¹⁵. The term $\left[1 - \exp\left(-\frac{d}{\Lambda_0}\right)\right]$ accounts for the decrease in conductivity in a nanowire with respect to bulk, due to boundary scattering, namely the scattering of phonons at the nanowire sidewalls. The exponential term approximates the probability of such scattering event. We notice that it yields a good fit for nanowires with $d \geq 40 \text{ nm}$. From the fit of those datapoints the mean free path of phonons in WZ GaP can be extracted and is found to be $800 \pm 100 \text{ nm}$. However, nanowires with $d < 40 \text{ nm}$ do not follow the expected behavior of diffusive phonon transport described by the formula: instead of having a smaller thermal conductivity than nanowires with larger diameter, their conductivity increases by up to a factor of 5.

In order to obtain a better insight on the phenomenon, the dependence of the thermal conductivity on the nanowire length is investigated. The conductance normalized to the square of the diameter is plotted as a function of length in Fig.8.4, obtained by measuring a number of nanowires on thermal bridge microdevices with different spacing between the beams. The data shows that for nanowires with $d \geq 50 \text{ nm}$ the area-normalized conductance varies with nanowire length with a $1/L$ behavior, typical for diffusive transport (blue and black dashed lines are guides to the eye). The area-normalized conductance of the nanowires with $d < 50 \text{ nm}$ does not depend on the length up to $12 \mu\text{m}$. The data indicates therefore that the phonon mean free path Λ_0 in nanowires with $d < 40 \text{ nm}$ is equal or greater than $12 \mu\text{m}$. This is an indication that in thin wires diffusive boundary scattering is surprisingly absent. Our current hypothesis is that, when reducing the nanowire diameter, the properties of the facets become more relevant. It is possible that, under a certain diameter, vibrational modes associated with the facets might become dominant, leading to a new heat transport mechanism. In order to confirm this behavior, more data needs to be gathered in future experiments, in order to reduce the scattering in the data and to measure the phonon mean free path for thin wires. Theoretical modelling is also recommended, for example using molecular dynamics, in order to understand the nanoscopic mechanism of phonon transport and to properly quantify the influence of diameter on these phenomena.

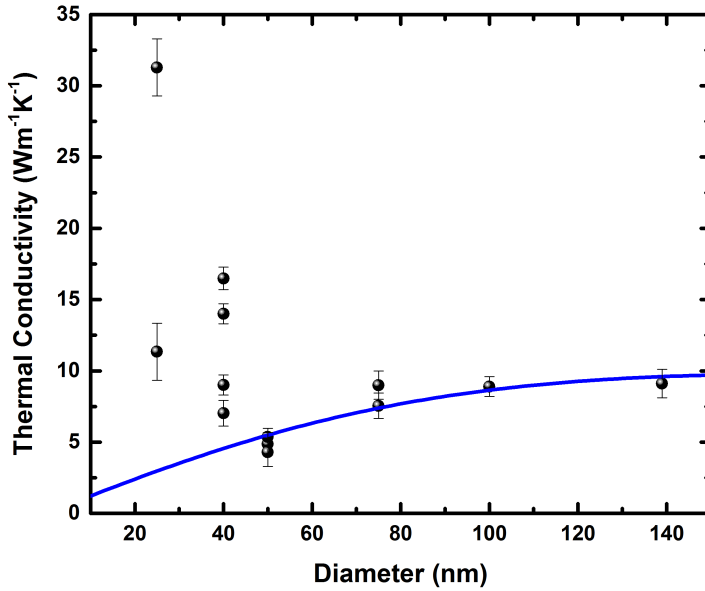


Figure 8.3: Conductivity of WZ GaP nanowires as a function of their diameter. The conductivity of nanowires with diameter larger than 50nm is well fit by the blue line, which describes the expected diffusive behavior, according to Equation 8.1. The nanowires with a smaller diameter show an unexpected increase in conductivity with decreasing diameter, which therefore cannot belong to the diffusive regime. Such a rising thermal conductivity suggests an increasing ballistic phonon transport behavior with decreasing diameter. With ballistic transport, phonons are not backscattered anymore and the total thermal conductivity of the nanowire increases.

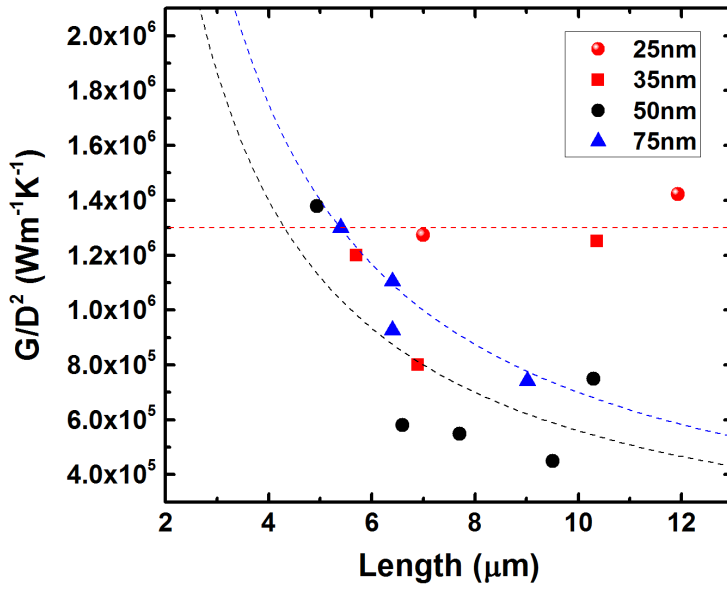


Figure 8.4: Thermal conductance of the WZ GaP nanowires, normalized with the square of the diameter, plotted as a function of length. The lines are guide to the eye, where the black and blue line follow a $1/L$ behavior, typical for diffusive transport. The red line is instead constant, as expected for ballistic transport, where the length of the nanowire does not influence the conductance. The red points, belonging to nanowires with diameter 25nm and 35nm, tend to follow the red line.

8.2 Telescopic GaP nanowires

In order to facilitate thermal management in a system, thermal rectification is desirable. Thermal rectification is realized when the conductivity of a system is dependent on the sign of the gradient of temperature, giving the system an asymmetric response to temperature gradients, as shown in Fig.8.5a. A thermal rectifier can be seen as the thermal equivalent of an electric diode, for example a p-n junction. A possible practical use of this phenomenon is in thermal coatings and heat sinks, where it is desirable to promote a certain direction of the heat flow over the other. In Fig.8.5b we show theoretical results from literature, where a thermal rectification up to 15% is predicted for telescopic nanowires with a 50% diameter difference¹¹⁶. Interestingly, in Fig.8.5b we notice that the rectification does not depend directly on the diameter ratio between the two sections. In fact it depends on the difference in thermal conductivity κ between the sections of the telescopic nanowire, which might have a non-trivial dependence with the diameter, as lateral confinement modifies the phonon density of states¹¹⁶. Therefore, in order to maximize the thermal rectification, an accurate design of the nanowire structure has to be performed during the epitaxial growth. Telescopic nanowires have been realized in Si, through a combination of modulated doping and selective wet etching¹¹⁷, and in GaAs, by partially consuming a Ga catalyst droplet and resuming the growth afterwards¹¹⁸. The diameter of a nanowire can also be tuned by changing the volume of the catalyst particle, for example by depletion of by providing a higher precursor flow¹¹⁹. Here we develop telescopic WZ GaP nanowires in order to investigate in the future a possible thermal rectification effect.

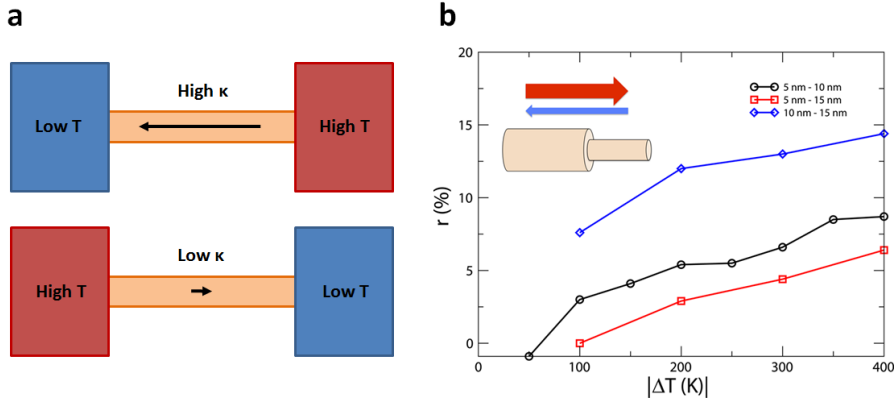


Figure 8.5: (a) Scheme of the thermal rectification phenomenon. Depending on the sign of the thermal gradient, the thermal conductivity κ changes. (b) Calculated thermal rectification as a function of temperature difference ΔT for three different telescopic nanowires with different diameters. The thermal rectification r is the difference of thermal conductivity κ of the nanowire obtained by changing direction of the thermal gradient cross it. The two diameters refer to the two different sections of the nanowire. Adapted from Ref. ¹¹⁶.

In order to obtain telescopic WZ GaP nanowires, we used two methods. In the first method we fabricate patterns of gold catalyst arrays on (111)B GaP through a SiN_x mask, using EBL. We grow the nanowires in the same conditions as the nanowires shown in Fig.8.1. Due to the presence of the SiN_x mask, the material accumulates at the base of the nanowire does not form a pyramidal pedestal like in Fig.8.1 as it tends to be confined within the hole. It forms instead a tapered shell for about half of the total nanowire length. In this way we are able to grow telescopic nanowires with a very large diameter difference between the two sections, as shown in Fig.8.6, where the bottom section has 235nm of diameter, while the top section has a ten times smaller diameter of 27nm. Remarkably, this is the highest ratio observed in a telescopic nanowire so far, to the best of our knowledge. However, this method does not allow to tune accurately the diameter of the larger section, as the accumulation of material on the sidewalls is a side effect of an unoptimized process, rather than a phenomenon directly and elementarily dependent from a variable we can control during the growth.

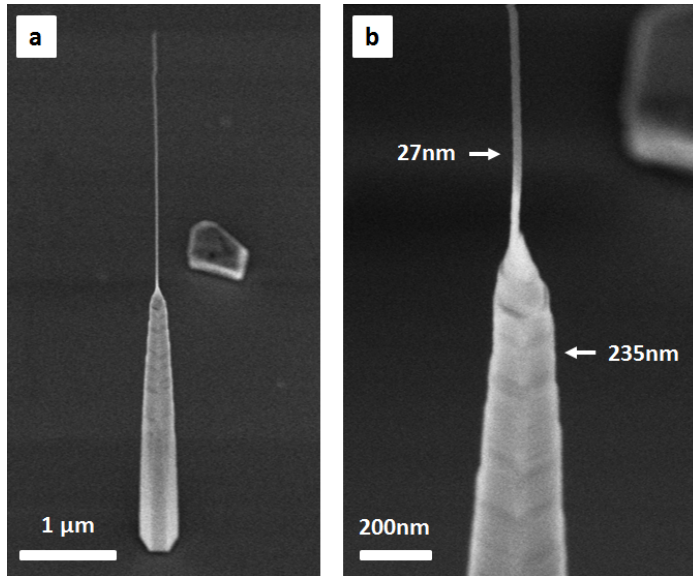


Figure 8.6: WZ GaP nanowire grown on (111)B GaP substrate with SiNx mask. Due to material accumulation at its base, the nanowire develops a partial shell which grows from the bottom up, slower than the nanowire itself. This shell can have a large diameter, in this case 235nm, while the nanowire has a ten times smaller diameter of 27nm.

In order to achieve accurate control over the diameter of both sections of the telescopic nanowires, we grow WZ GaP nanowires with VLS method on (111)B GaP substrate without a SiNx mask. This time we perform the growth in three steps as illustrated schematically in Fig.8.7a. We first grow the core of the first section of the nanowire at 615°C, then we stop the growth by closing the TMGa flow and lower the temperature to 550°C. At this temperature we grow a WZ GaP shell. By tuning the growth time of the shell, we can select the final diameter, with a growth rate of about 10nm/min. We then raise the temperature again to 615°C and perform a short droplet refill step (1.5s) to increase the Gallium concentration in the catalyst. This is needed due to the shell growth step, which tends to deplete the droplet of Gallium. The optimization of the refilling time is critical, as an incorrect time will lead to kinked nanowires as shown in Fig.8.7b. It is known in fact that kinked geometries can be grown by tuning the supersaturation in the catalyst particle¹²⁰. After the refilling step, we resume the growth of the second section of the WZ GaP nanowire.

By following these steps, we obtain telescopic nanowires as shown in Fig.8.7c-d, where the nanowire possesses two sections with respectively 22nm and 94nm of diameter. In Fig.8.8 we demonstrate the purity of the wurtzite crystal phase,

except only at the junction between the two sections of the nanowire, where a few stacking faults can be seen (red arrows). These defects are generated during the shell growth, which happens at different growth conditions than the axial growth of pure wurtzite GaP. Some axial growth happens also during the shell growth and, as the conditions are non-optimal for WZ growth, some ZB planes are nucleated. The yield is close to 100% for diameters above 40nm, but becomes very low for smaller diameters. This might be due to the fact that the success of the protocol depends on the optimization of the growth parameters for a certain diameter. When a Au droplet possesses large volume, eventual droplet to droplet variations, due for example to the fabrication procedure, are relatively small. With very small ($< 40nm$) diameters however fluctuations in the catalyst volume will greatly affect the outcome of the growth procedure. Our conclusion is that with the due optimization of the fabrication procedure, 100% yield can be achieved.

8.3 Conclusions

In this work we have demonstrated the realization of telescopic nanowires with controlled diameter in both sections, opening the way for testing the hypothesis of thermal rectification in this type of nanostructures. As we have shown in Fig.8.5, the rectifying behavior depends on the diameter of the two sections of the nanowires, due to the different thermal conductivity κ of the two segments. Our growth method allows for the tuning of both diameters, therefore being promising for fabricating nanowires with potentially strong rectification behavior. Future studies will be performed using the previously shown bridge microdevices, by measuring the conductivity of the nanowires for both directions of the temperature gradient across the nanowire, in order to find an eventual rectifying behavior. An added value of our nanowires is the indication of ballistic transport at low diameters, which might play a role also in thermal rectification, for example by having two sections of the nanowire with different dominant transport mechanism, one ballistic and one diffusive. Such design might also help in clarifying the underlying mechanism behind the indications of ballistic transport we observed in WZ GaP nanowires.

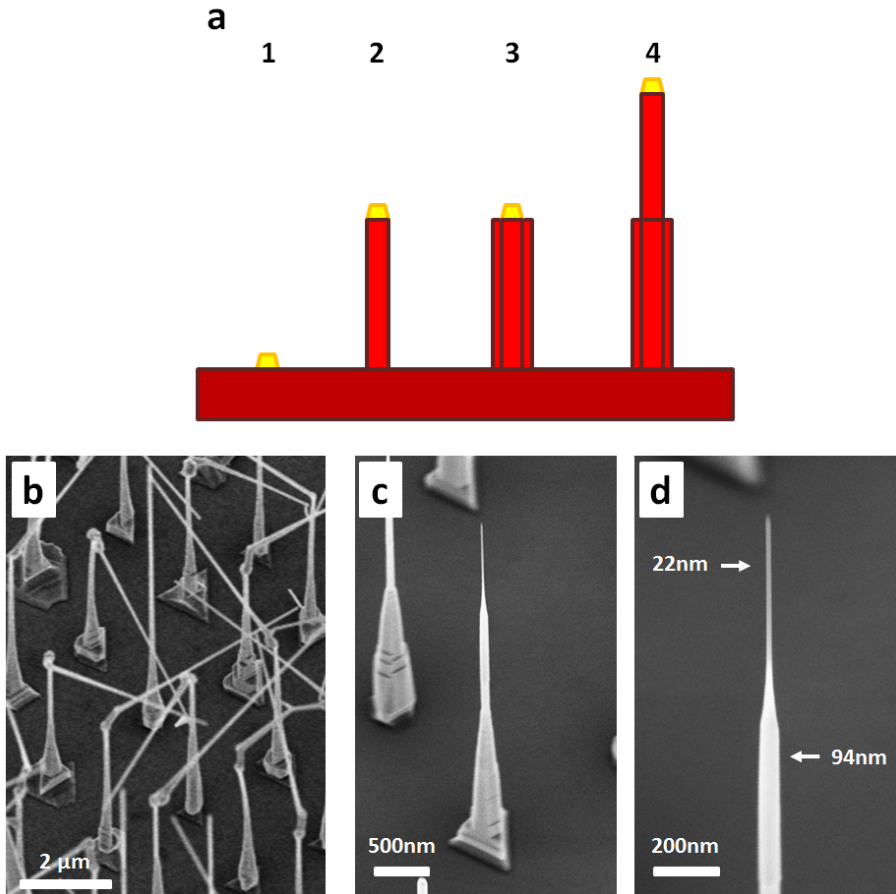


Figure 8.7: (a) Growth scheme of a telescopic nanowire using the step method on (111)B GaP substrate without a SiN_x mask. We start from a Au catalyst droplet (1), then (2) grow a WZ GaP thin nanowire (about 25nm diameter). We then stop the growth and lower the temperature to 550°C to grow a WZ GaP shell (3), then increase the temperature again to 615°C and grow the final section of the nanowire (4). (b-d) WZ GaP nanowires grown using the protocol described in (a). (b) The second section of the nanowires results kinked, as the droplet refilling step is unoptimized. (c-d) Nanowire grown with optimized recipe. Droplet refilling time: 1.5s for a Au particle diameter of about 20nm. The overall morphology is controllable and the diameter of both sections can be tuned. Tapering can be observed at the junction between the two sections, probably due to unwanted axial growth during the shell growth.

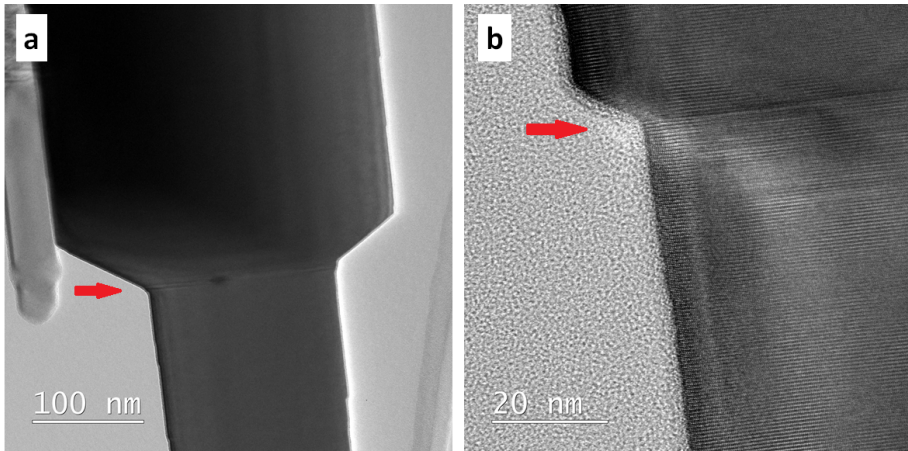


Figure 8.8: (a) TEM bright field and (b) STEM images of two different telescopic nanowires grown with the controlled mechanism in Fig.8.7, with different section diameters. The crystal structure is pure wurtzite for both, except at the junction between the two sections of the nanowire, where a few stacking faults can be seen. These are due to axial growth during the shell growth step.

Chapter 9

Wurtzite III-phosphide nanowires for solid state lighting

The LED market has been steadily growing for the last decades and is predicted to keep growing at a 3% yearly rate. Lower costs, high efficiency and high colour rendering are sensibly decreasing the customer adoption resistance and LED market is predicted to constitute 90% of the global lighting market by 2025. Nanostructured LEDs (NanoLEDs) are predicted to further increase LED efficiency and therefore decrease the cost of the final products, further promoting the use of LEDs and increasing the market volume. In the present work we propose a novel NanoLED system, based on scientific work performed at Eindhoven University of Technology, which can be realistically translated into a commercial gamma of LEDs emitting between the infrared and green regions of the visible spectrum. Based on our current knowledge, we propose a roadmap of activities needed to further study the NanoLED system and develop a working prototype. As a solution, we propose to implement the technology into the portfolio of an existing, well-established company operating in the LED market by performing a technology transfer. Our preliminary conclusion is that the biggest challenge is the development of the technology itself and the scientific and technological questions should be addressed first.

9.1 Market Analysis

LEDs are widely recognized as the future standard of general lighting, due to their high efficiency and high brightness. The LED market volume has been steadily rising in the last decades, is still rising today by about 5% per year and is expected to reach between 20 and 50 billion dollars by 2020. LED market is predicted to reach over 90% of the entire lighting market by 2025. To make a notable example, Philips Lighting has seen a decrease of their overall sales between Q1 2016 - Q1 2017 (-1.3%) but the LED-based sales grew by 17%, now representing roughly 60% of their total sales¹²¹.

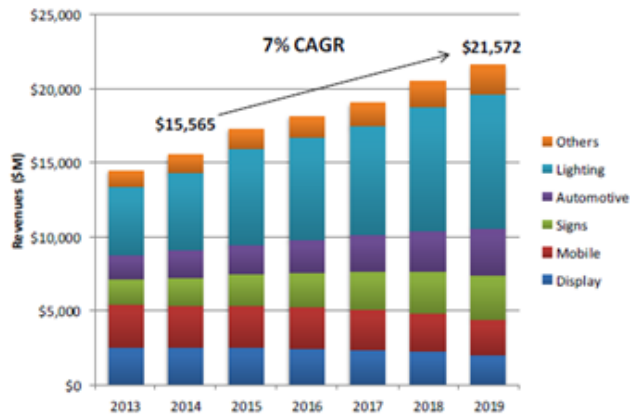


Figure 9.1: Global LED sales between 2013-2019, mixing historical and projected data in a 2016 report. The general lighting market is expected to account for almost 50% of the global LED market. CAGR: Compound Annual Growth Rate. Adapted from Ref. ¹²².

The players on the LED market can be roughly divided in two categories, namely the companies manufacturing the LED chips (the physical light emitter) and the companies selling the final packaged solution. In this discussion, we want to focus on the LED chip manufacturers due to the nature of our invention. The main LED chip manufacturers, namely the companies manufacturing the highest quality LED chips, are:

- Cree, based in Durham, NC, US
- Nichia, based in Anan, Japan
- Osram, based in Munich, Germany

- Lumileds, based in Netherlands and US
- Toyoda Gosei, based in Japan
- Showa Denko K.K., based in Japan

These major players compete mostly on efficiency, as this is the key parameter needed to cut the cost by maintaining performance, therefore determining the competitiveness of a product. Innovation is therefore developed through scientific research, often in partnership with universities (e.g. Santa Barbara Univ., Nagoya Univ.). All these companies employ LED research scientists and possess research-dedicated infrastructure where semiconductor R&D is performed.

Historically, LED white lamps have faced customer adoption resistance due to high cost. Constant decrease in manufacturing prices, increased customer awareness of the high efficiency and continuous improvements in the quality of lighting (e.g. color rendering index CRI>90) are leading to less resistance¹²³. Due to competition pressure, costs are decreasing even faster than expected. Major manufacturers now offer LED lamps with payback time of less than 1 year¹²⁴.

Year	2012	2016	2020	2025	2030
lm/W	58	93	118	142	169
Price (€)	18.0	10.0	7.5	5.0	2.5

Table 9.1: Price and performance forecast for a 10W LED light bulb from the CLASP 2013 review study¹²⁴. The efficiency is expected to rise by a factor of 2 between 2016-2030, while the price is expected to decrease by a factor of 4, leading to an increase in cost-effectiveness of 8 times.

The efficiency of LEDs is of great importance, as a higher efficiency allows cutting costs of the final device (e.g. a white lamp) and reduces the payback time, making the product more competitive. Recent innovations such as laser lighting for automotive applications and microLED displays are opening new market applications for LEDs with high added value. Additional applications are also healthcare and security, especially for infrared-emitting LEDs. The possibility to add 'smart' functions like dynamic dimming and colour mixing to create custom 'scenes', plus the integration with wireless connection systems are promoting the use of LED lights beyond the traditional applications.

Current LEDs still have some fundamental limits which need to be overcome in order to further improve their performance and reduce their cost. First of all, substrate cost is still high, as most LEDs are grown on sapphire (GaN LEDs) or GaAs/GaP (AlInGaP LEDs). This limit is due to the intrinsic need of planar

LEDs to be grown on high quality substrates with compatible properties (especially lattice parameter) in order to avoid excessive defectivity in the active region, which would deteriorate their brightness and lifetime. Efforts are underway to grow GaN/InGaN LEDs on silicon, a very cheap substrate, where a viable method is to grow three-dimensional nanowire structures due to the high lattice mismatch (about 17%) between GaN and Si. GaN/InGaN nanowires are considered the state of the art in LED technology and major players such as Samsung and Osram are strongly investing in this direction. Many innovative startups such as Glo (Sweden), Aledia (France) and Cryonano (Norway) are currently exploring nanowire solutions to achieve high efficiency at a reduced cost. Besides the potential cost cut regarding substrates, nanowire structures offer the possibility of increasing the active emitting area in comparison to planar systems, as the total surface area of a three-dimensional pillar structure is higher than the simple planar counterpart. This increase in junction area allows the lowering of the current density while maintaining the same total current, thus reducing the droop phenomenon, namely the loss of efficiency at high operating current. A typical challenge in planar devices is the extraction of light from the emitting device. Internal reflection happens due to the contrast in refractive index between the semiconductor crystal and its surroundings (capping resin and air). Nanowires, due to their geometry, have shown very high light outcoupling and are therefore suitable for light emitting devices with very low losses due to internal reflection. One additional limit of LEDs is the poor performance of direct emitters in the green-amber region¹. The GaN/InGaN system is affected by poor material quality, due to lattice mismatch and low miscibility of Indium, causing alloy fluctuations. AlGaInP alloys instead become indirect semiconductors in the green-amber region and are no longer able to emit efficiently.



Figure 9.2: Examples of innovative LED systems. (a) A matrix of LEDs embedded in a flexible polymer for flexible LED displays. (b) Apple watch with microLED display. (c) Headlight of an Audi car, mounting a laser lighting system based on semiconductor diodes. (d) Color-tunable LED lamp, with dedicated mobile application.

9.2 Our proposed invention

In this thesis we have started developing a new solution for NanoLEDs, emitting in the infrared to green range, using wurtzite (WZ) Al(Ga)InP nanowires. These nanowires are grown with Metalorganic Vapour Phase Epitaxy, show strong light emission properties and are a novelty, as WZ AlInP has never been grown using catalyst-free selective area epitaxy before, making the invention suitable for patenting, in order to protect the intellectual property. Wurtzite material also emits polarized light, therefore a possible patent might protect a polarized light emitter. We judge that our nanowires possess several advantages if used as emitting material in LEDs as also described in Chapter 1, in terms of efficiency increase, light outcoupling and potential cost reduction. The ideal device would be fabricated on Silicon, the cheapest epitaxy substrate available so far. Thanks to the nanowire geometry, such integration will lead to defect-free nanowires, capable of efficient light emission. In order to contact the nanowires collectively, a transparent conductive oxide such as ITO or ZnO can be used. The final LED can be packaged by using standard techniques used for existing commercial LEDs. We show a concept of the WZ AlInGaP nanowire LED in Fig.9.3.

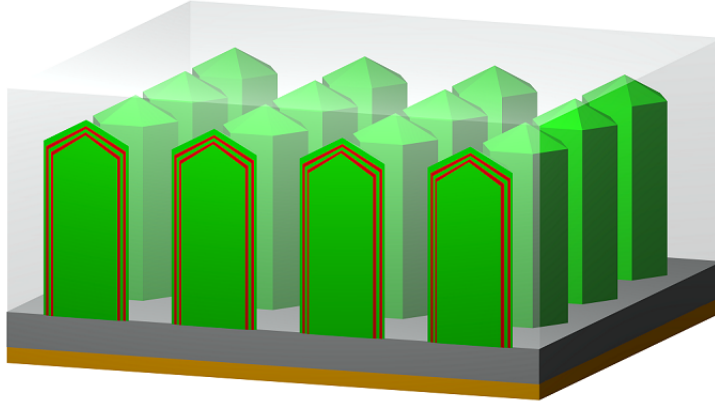


Figure 9.3: Concept of AlInGaP NanoLED. Green/red: AlInGaP nanowires, with radial multi-quantum well structures (red). Grey: substrate (e.g. silicon). Yellow: metallic back contact. Transparent: conductive oxide front contact, transparent to visible light.

9.3 Business Model

Two different approaches could be adopted towards this new technology: a new venture can be created, based on a patent portfolio, or the technology can be implemented into an existing company operating in the sector, through a technology transfer. The choice has to be made by comparing the requirements and the potential of the two approaches, and especially by considering the total market size available to a product based on the invention, which is possibly the most important factor determining the potential of a new venture. In the case of a new venture, the necessary infrastructure and equipment have to be made available or built anew. Due to the nature of the venture the necessary equipment is particularly expensive and is estimated as:

- Metalorganic vapour phase epitaxy (MOVPE) reactor
- Photoluminescence optical setup with cryogenic equipment
- Cleanroom fabrication equipment to produce experimental LEDs

Special solutions could be arranged, by obtaining access to already existing infrastructure, which is however rare and anyway expensive. It is also possible to place the venture in a particular point of the value chain, for example the fabrication of only the basic LED chip, without any packaging. The LED chip

can be then sold to a company specialized in packaging and lighting solutions. This is a solution adopted by some startups (e.g. Cryonano, Norway). In the case of the implementation of the knowledge into an existing company, for example by licensing the intellectual property, the infrastructure and equipment requirements are met by definition. Additionally, the expertise available in a competitive company can only be beneficial to the success of the operation.

An even more important aspect is the market segment. In LED applications, lighting based on white lamps consists in almost the totality of the market. The possibility to fabricate efficient white lamps is key to the success of a LED venture. This is unfortunately not possible with the AlInGaP alloy, due to previously mentioned intrinsic physical limits which cannot be overcome, making it impossible to fabricate blue LEDs. A venture based solely on infrared to green emitting material cannot access the main customer segments of the general lighting. Strong and well established competitors constitute an additional risk factor. Major players also possess a large wealth of intellectual property, which is very likely to block the operations of a newcomer. All these limitations can be overcome through a strategic partnership, by transferring the technology to a well established company operating in the LED market. In this case the invention can be integrated into existing products and solutions already existing in the partner company can be used, all leading to a much lower time to market and increased probability of success. In light of these considerations, we now want to delineate an effective business model based on our AlInGaP NanoLEDs. We do this using the Business Model Canvas framework¹²⁵. Within this framework, we define a series of areas necessary to define a solid business model, which are listed and discussed below.

9.3.1 Value proposition

The added value of our invention is the potential to reach higher external quantum efficiency than current infrared to green LEDs based on planar technology, with the mechanisms explained in the previous sections. Efficiency is of great importance in lighting as higher efficiency leads to lower cost of the final product, thus increasing market competitiveness. The projected increase in efficiency therefore makes our technology highly desirable. Being our material a direct light emitter, phosphors are no longer necessary to produce efficient emission, leading to reduced costs and a more monochromatic emission, interesting for display technology where sharp monochromatic emission is desirable to obtain a larger gamma of colors.

9.3.2 Key partnerships

As our decision is to perform a technology transfer to an existing LED company, partnership is of fundamental importance in our plan. The PhD project was co-funded by Philips, which owns the patent filed so far. Philips operates in the lighting market and is therefore interested in securing a supply of superior LED lights for their own applications. Philips is therefore our first ally in the plan. As Philips does not manufacture LEDs, a second partnership is necessary. LED manufacturers such as Lumileds, Cree and Osram are ideal to receive our technology and innovate further.

9.3.3 Customer segments

Two levels of customers can be defined: receivers of the technology transfer, customers buying LEDs based on our invention. The receiver needs to be a well established company operating in the LED sector. Lumileds, Cree, Osram are excellent candidates. The customer segments of the final LED products are already defined and a relationship with them is already established, greatly increasing the chances of success for this plan. As our NanoLEDs can emit between the infrared and green range, the target market should be a niche market, as white lights require a blue component in order to be built. A suitable market is in high-power LEDs for projection and outdoor signs and displays, where bright and monochromatic emission is required.

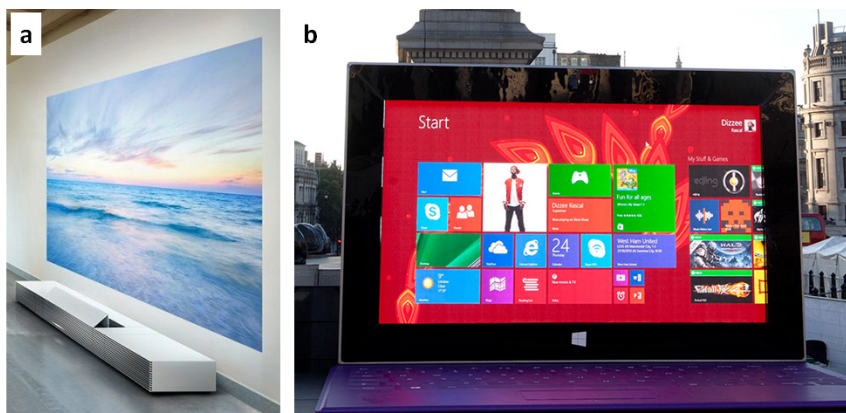


Figure 9.4: (a) Sony 4K Ultra Short Throw Projector. (b) Outdoor LED screen with high brightness, necessary to provide with sufficient contrast in natural illumination condition. Source: YSLV.

9.3.4 Key activities and resources

The most important activity at the beginning will be the actual technology transfer, therefore the development of the necessary methods and processes in the receiving company. The company will have to allocate the resources necessary to the epitaxial growth of the active material, its optical study, LED fabrication and their electrical characterization. A dedicated reactor for research on III-phosphides has to be used. Specialized personnel, expert in LED growth and fabrication is preferable. All these resources are already present in LED manufacturing companies as well as TU/e. Additional resource is the intellectual property, in the form of patents.

9.3.5 Cost structure

R&D activities concerning semiconductor epitaxy are expensive and pre-existing equipment should preferably be used. Specialized personnel is already available both in university and receiving company. Patenting is also a necessary investment to protect the intellectual property from competitors. The final advantages on cost reduction given by the adoption of NanoLEDs are on all the aspects shown in Fig.9.5. The use of cheap substrates such as silicon, reduced epitaxy time due to high growth rate and less material use, reduced wafer processing due to higher outcoupling of light, no phosphors and higher efficiency, which reduces the complexity of packaging.

9.3.6 Channels and revenue streams

A well established LED company already possesses all the necessary distribution and marketing channels needed to monetize on the invention. The revenue stream is constituted by the sales of LEDs containing our technology.

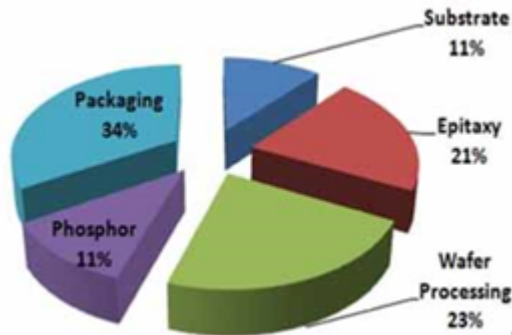


Figure 9.5: Cost breakdown of an LED device. NanoLEDs can cut the costs on all aspects of the LED manufacturing.

9.4 Activity roadmap

Here we discuss the courses of action to undertake in order to perform the technology transfer and develop a NanoLED prototype. Such a prototype can be considered as a minimum viable product which should be benchmarked and eventually further developed.

9.4.1 Scientific developments

Once an industrial partner has been found, additional scientific development can start. In order to develop a prototype of an AlInGaP NanoLED, additional fundamental knowledge needs to be gathered. First of all, the AlInGaP alloy can be grown in two crystal structures, zincblende (ZB) and wurtzite (WZ) with different optical properties. ZB is the commonly used crystal structure for conventional AlInGaP LEDs, while WZ is the novelty. The experimental data gathered so far suggests that WZ might be more efficient than ZB up to the yellow range. Conclusive data on the efficiency in the green range also has to be obtained. For most purposes, ZB or WZ AlInGaP might be substantially equivalent in internal quantum efficiency. However, nanowire geometry is anyway essential in order to maximize the external quantum efficiency through high light outcoupling. The best course of action is to continue the scientific study of AlInGaP nanowires, in-house at the receiving company or possibly through university collaborations. The same TU/e could carry out a follow-up of the original PhD project which generated the present invention.

The personnel necessary to initially carry out the project can vary between one or more, depending on the size of the project and the experience of the available

personnel. The original project was carried out by one single PhD candidate in 4 years. In order to accelerate the development time, a higher number of people assigned to the project is desirable.

9.4.2 Technological nodes

In order to evaluate the opportunity of the technology transfer, we need to examine the main technological nodes influencing its potential success as a commercial product. The most critical element is the efficiency of AlInGaP NanoLEDs, as the improvement of the LED external quantum efficiency is the main purpose of the research. The critical node is the potential to obtain a higher external quantum efficiency than currently available infrared to green emitting LEDs. This main driving factor can be broken down in more specific driving factors, specifying the main challenges that need to be overcome. In order to succeed in developing a future complete product, all these factors need to be addressed by developing appropriate solutions. Material quality is necessary to obtain homogeneous material with high internal quantum efficiency. The possibility to tailor composition, in order to obtain quantum wells, and nanowire structure, in order to control the aspect ratio, are important for the final outcome. At the current stage, our NanoLED candidates are grown on InP wafers, which are expensive and absorb the emitted light. The possibility to grow on (semi)transparent substrates such as GaP or a very cheap substrate like Si would be optimal. Additionally, due to the three-dimensional geometry of our nanowires, a solution for the top contact has to be developed. The top contact needs to be ohmic with WZ AlGaInP, be highly conductive in order to spread the current evenly throughout the device with minimal losses and most importantly needs to be fully transparent to the emitted light.

9.4.3 Substrate development

As the substrate is one of the main cost factors in LED manufacturing, the possibility to grow AlInGaP nanowires on silicon would be optimal to guarantee a high cost-efficiency of the final devices. Nanowire growth on silicon has been demonstrated and is already of major interest for the GaN/InGaN system. Also AlInGaP nanowires can be epitaxially grown on Silicon, thus offering a large cost reduction. The cost reduction is also associated on the availability of Silicon wafers which have a larger diameter than III-V based wafers, which are usually limited to 4-inch, while Silicon wafers can reach 8 or 12 inch. In Table 9.2 we list our estimation of the price of common 2-inch semiconductor wafers for LED epitaxy.

Wafer	Price(€)
GaN-Sapphire	150-500
GaP	150-400
InP	150-400
GaAs	150-300
SiC	100-300
Si	< 25

Table 9.2: Estimated commercial price of 2-inch semiconductor wafers for epitaxy. Prices vary between different suppliers and as a function of quality and doping.

9.4.4 Electrical top contact

Due to the three-dimensional geometry of our nanowires, a solution for the top contact has to be developed. The top contact needs to be ohmic with WZ AlGaInP, be highly conductive in order to spread the current evenly throughout the device with minimal losses and most importantly needs to be fully transparent to the emitted light. A high-band gap conductive oxide should be an optimal choice for a NanoLED. For this purpose, ITO is commonly used but other materials such as ZnO are emerging^{126;127}. Both should be investigated during the development of the NanoLED, possibly in collaboration with a university. In TU/e transparent conductive oxides are developed and a joint project could be started to evaluate their use. Here, the main challenges are the contact resistance of the oxide with AlGaInP and the morphology of the oxide layer (e.g. conformality, voids, etc.).

9.4.5 Estimated time of development

In light of our results and our present knowledge, the amount of time needed to translate the present scientific findings into a viable product is estimated between 2 and 5 years if a partnership with an established company is established. Notably, most of the knowledge and expertise needed can be provided by the company receiving the technology (e.g. Lumileds), thus shortening considerably the time to market. A suggested approach is also to fund PhD projects at Eindhoven University of Technology working on the previously listed technological nodes, so to speed up the process and obtain in-depth knowledge on the material.

9.5 Conclusions

Based on our current knowledge, we judge wurtzite AlGaInP nanowires as a realistic candidate for NanoLEDs in the infrared to green region. They offer a potential increase in efficiency and, most importantly, a strong reduction in production costs, which would make them very competitive on the LED market, especially in the field of projection and outdoor displays. We strongly suggest to continue the scientific research on the subject, possibly in collaboration with Eindhoven University where this NanoLED candidate was first developed. Through a university-company partnership, the time to market can be considerably shortened, due to the technological solutions and knowledge already present in a well-established LED manufacturer.

Bibliography

- [1] Asif Khan. Laser diodes go green. *Nature Publishing Group*, 3(8):432–434, 2009.
- [2] Maaïke Bouwes Bavinck, Klaus D. Jöns, Michał Zieliński, Gilles Patriarche, Jean Christophe Harmand, Nika Akopian, and Val Zwiller. Photon Cascade from a Single Crystal Phase Nanowire Quantum Dot. *Nano Letters*, 16(2):1081–1085, 2016.
- [3] S. Assali, L. Gagliano, D. S. Oliveira, M. A. Verheijen, S. R. Plissard, L. F. Feiner, and E. P. A. M. Bakkers. Exploring Crystal Phase Switching in GaP Nanowires. *Nano Letters*, 15(12):8062–8069, 2015.
- [4] Frank Glas, Jean-Christophe Harmand, and Gilles Patriarche. Why Does Wurtzite Form in Nanowires of III-V Zinc Blende Semiconductors? *Physical Review Letters*, 99(14):146101, oct 2007.
- [5] S Assali, I Zardo, S Plissard, D Kriegner, M a Verheijen, G Bauer, a Meijerink, a Belabbes, F Bechstedt, J E M Haverkort, and E P a M Bakkers. Direct band gap wurtzite gallium phosphide nanowires. *Nano letters*, 13(4):1559–63, apr 2013.
- [6] Abderrezak Belabbes, Christian Panse, Jürgen Furthmüller, and Friedhelm Bechstedt. Electronic bands of III-V semiconductor polytypes and their alignment. *Physical Review B*, 86(7):075208, aug 2012.
- [7] Anthony Standing, Simone Assali, Lu Gao, Marcel A Verheijen, Dick van Dam, Yingchao Cui, Peter H L Notten, Jos E M Haverkort, and Erik P A M Bakkers. Efficient water reduction with gallium phosphide nanowires. *Nature communications*, 6(May):7824, 2015.
- [8] Q Dai, M. F Schubert, M. H. Kim, J K Kim, E F Schubert, D D Koleske, M H Crawford, S R Lee, A J Fischer, G Thaler, and M A Banas. Internal quantum efficiency and nonradiative recombination coefficient of

- GaNN/GaN multiple quantum wells with different dislocation densities. *Applied Physics Letters*, 94(11):5–7, 2009.
- [9] Grzegorz Grzela, Ramón Paniagua-Domínguez, Tommy Barten, Yannik Fontana, José a Sánchez-Gil, and Jaime Gómez Rivas. Nanowire antenna emission. *Nano letters*, 12(11):5481–6, nov 2012.
- [10] Linyou Cao, Pengyu Fan, Alok P Vasudev, Justin S White, Zongfu Yu, Wenshan Cai, Jon a Schuller, Shanhui Fan, and Mark L Brongersma. Semiconductor nanowire optical antenna solar absorbers. *Nano letters*, 10(2):439–45, feb 2010.
- [11] Dick van Dam, Diego R. Abujetas, Ramón Paniagua-Domínguez, José a. Sánchez-Gil, Erik P. a. M. Bakkers, Jos E. M. Haverkort, and Jaime Gómez Rivas. Directional and Polarized Emission from Nanowire Arrays. *Nano letters*, ASAP:150608160137007, 2015.
- [12] Siddha Pimputkar, James S Speck, Steven P. DenBaars, and Shuji Nakamura. Prospects for LED lighting. *Nature Photonics*, 3(4):180–182, 2009.
- [13] Matthias Auf Der Maur, Alessandro Pecchia, Gabriele Penazzi, Walter Rodrigues, and Aldo Di Carlo. Efficiency Drop in Green InGaN/GaN Light Emitting Diodes: The Role of Random Alloy Fluctuations. *Physical Review Letters*, 116(2):1–5, 2016.
- [14] Michael R. Krames, Oleg B. Shchekin, Regina Mueller-Mach, Gerd O. Mueller, Ling Zhou, Gerard Harbers, and M. George Craford. Status and Future of High-Power Light-Emitting Diodes for Solid-State Lighting. *Journal of Display Technology*, 3(2):160–175, jun 2007.
- [15] D. J. Mowbray, O. P. Kowalski, M. Hopkinson, M. S. Skolnick, and J. P R David. Electronic band structure of AlGaInP grown by solid-source molecular-beam epitaxy. *Applied Physics Letters*, 65(2):213–215, 1994.
- [16] Lingrong Jiang, Jianping Liu, Aiqin Tian, Yang Cheng, Zengcheng Li, Liqun Zhang, Shuming Zhang, Deyao Li, M. Ikeda, and Hui Yang. GaN-based green laser diodes. *Journal of Semiconductors*, 37(11):111001, 2016.
- [17] Hon-Way Lin, Yu-Jung Lu, Hung-Ying Chen, Hong-Mao Lee, and Shangjr Gwo. InGaN/GaN nanorod array white light-emitting diode. *Applied Physics Letters*, 97(7):073101, 2010.
- [18] Fang Qian, Yat Li, Silvija Gradecak, Hong-Gyu Park, Yajie Dong, Yong Ding, Zhong Lin Wang, and Charles M Lieber. Multi-quantum-well nanowire heterostructures for wavelength-controlled lasers. *Nature materials*, 7(9):701–6, sep 2008.

-
- [19] Shunfeng Li and Andreas Waag. GaN based nanorods for solid state lighting. *Journal of Applied Physics*, 111(7):071101, 2012.
- [20] Young-Ho Ko, Je-Hyung Kim, Su-Hyun Gong, Joosung Kim, Taek Kim, and Yong-Hoon Cho. Red Emission of InGaN/GaN Double Heterostructures on GaN Nanopyramid Structures. *ACS Photonics*, page 150213130931004, feb 2015.
- [21] Robert Colby, Zhiwen Liang, Isaac H. Wildeson, David A. Ewoldt, Timothy D. Sands, R. Edwin Garcia, and Eric A. Stach. Dislocation filtering in GaN nanostructures. *Nano Letters*, 10(5):1568–1573, 2010.
- [22] Christopher Kölper, Matthias Sabathil, Friedhard Römer, Martin Mandl, Martin Strassburg, and Bernd Witzigmann. Core-shell InGaN nanorod light emitting diodes: Electronic and optical device properties. *Physica Status Solidi (a)*, 209(11):2304–2312, nov 2012.
- [23] Hiroto Sekiguchi, Katsumi Kishino, and Akihiko Kikuchi. Emission color control from blue to red with nanocolumn diameter of InGaN/GaN nanocolumn arrays grown on same substrate. *Applied Physics Letters*, 96(23):96–99, 2010.
- [24] Christoph J M Stark, Theeradetch Detchprohm, S. C. Lee, Y. B. Jiang, S. R J Brueck, and Christian Wetzel. Green cubic GaInN/GaN light-emitting diode on microstructured silicon (100). *Applied Physics Letters*, 103(23), 2013.
- [25] I. E. Orozco Hinojosa, M. Avalos-Borja, V. D. Compeán García, C. Cuelar Zamora, A. G. Rodríguez, E. López Luna, and M. A. Vidal. Tuning emission in violet, blue, green and red in cubic GaN/InGaN/GaN quantum wells. *Journal of Crystal Growth*, 435:110–113, 2016.
- [26] Friedhelm Bechstedt and Abderrezak Belabbes. Structure, energetics, and electronic states of III-V compound polytypes. *Journal of physics. Condensed matter : an Institute of Physics journal*, 25(27):273201, jul 2013.
- [27] Themistoklis P. H. Sidiropoulos, Robert Roder, Sebastian Geburt, Ortwin Hess, Stefan a. Maier, Carsten Ronning, Rupert F. Oulton, Robert Röder, Sebastian Geburt, Ortwin Hess, Stefan a. Maier, Carsten Ronning, Rupert F. Oulton, Robert Roder, Sebastian Geburt, Ortwin Hess, Stefan a. Maier, Carsten Ronning, Rupert F. Oulton, Robert Röder, Sebastian Geburt, Ortwin Hess, Stefan a. Maier, Carsten Ronning, and Rupert F. Oulton. Ultrafast plasmonic nanowire lasers near the surface plasmon frequency. *Nature Physics*, 10(11):870–876, 2014.

- [28] Changyi Li, Jeremy B. Wright, Sheng Liu, Ping Lu, Jeffrey J. Figiel, Benjamin Leung, Weng W. Chow, Igal Brener, Daniel D. Koleske, Ting-Shan Luk, Daniel F. Fezell, S. R. J. Brueck, and George T. Wang. Nonpolar InGaN/GaN Core-Shell Single Nanowire Lasers. *Nano Letters*, page acs.nanolett.6b04483, 2017.
- [29] Qian Gao, Dhruv Saxena, Fan Wang, Lan Fu, Sudha Mokkalapati, Yanan Guo, Li Li, Jennifer Wong-Leung, Philippe Caroff, Hark Hoe Tan, and Chennupati Jagadish. Selective-area epitaxy of pure wurtzite InP nanowires: High quantum efficiency and room-temperature lasing. *Nano Letters*, 14(9):5206–5211, 2014.
- [30] B. Mayer, L. Janker, B. Loitsch, J. Treu, T. Kostenbader, S. Lichtmannecker, T. Reichert, S. Morkötter, M. Kaniber, G. Abstreiter, C. Gies, G. Koblmüller, and J. J. Finley. Monolithically Integrated High-?? Nanowire Lasers on Silicon. *Nano Letters*, 16(1):152–156, 2016.
- [31] Hsinhan Tsai, Wanyi Nie, Jean-Christophe Blancon, Constantinos C. Stoumpos, Reza Asadpour, Boris Harutyunyan, Amanda J. Neukirch, Rafael Verduzco, Jared J. Crochet, Sergei Tretiak, Laurent Pedesseau, Jacky Even, Muhammad A. Alam, Gautam Gupta, Jun Lou, Pulickel M. Ajayan, Michael J. Bedzyk, Mercouri G. Kanatzidis, and Aditya D. Mohite. High-efficiency two-dimensional Ruddlesden-Popper perovskite solar cells. *Nature*, 536(7616):312–316, 2016.
- [32] Matt Law, Lori E. Greene, Justin C. Johnson, Richard Saykally, and Peidong Yang. Nanowire dye-sensitized solar cells. *Nature Materials*, 4(6):455–459, 2005.
- [33] Magnus T. Borgström, Jesper Wallentin, Nicklas Anttu, Damir Asoli, Maria Huffman, Ingvar Åberg, Martin H. Magnusson, Gerald Siefer, Peter Fuss-Kailuweit, Frank Dimroth, Bernd Witzigmann, H. Q. Xu, Lars Samuelson, Knut Deppert. InP nanowire array solar cells achieving 13.8% efficiency by exceeding the ray optics limit. *Science (New York, N.Y.)*, 339(6123):1057–60, 2013.
- [34] Dick van Dam, Niels J. J. van Hoof, Yingchao Cui, Peter J. van Veldhoven, Erik P. A. M. Bakkers, Jaime Gómez Rivas, and Jos E. M. Haverkort. High-Efficiency Nanowire Solar Cells with Omnidirectionally Enhanced Absorption Due to Self-Aligned Indium-Tin-Oxide Mie Scatterers. *ACS Nano*, page acsnano.6b06874, 2016.
- [35] Barry P. Rand, Jan Genoe, Paul Heremans, and Jef Poortmans. Solar Cells Efficiency Tables. *Prog. Photovolt: Res. Appl.*, 15(February 2013):659–676, 2007.

- [36] R. R. King, D. C. Law, K. M. Edmondson, C. M. Fetzer, G. S. Kinsey, H. Yoon, R. A. Sherif, and N. H. Karam. 40% efficient metamorphic GaInPGaInAsGe multijunction solar cells. *Applied Physics Letters*, 90(18):90–93, 2007.
- [37] Nicklas Anttu, Alireza Abrand, Damir Asoli, Magnus Heurlin, Ingvar Åberg, Lars Samuelson, and Magnus Borgström. Absorption of light in InP nanowire arrays. *Nano Research*, 7(6):816–823, 2014.
- [38] Y. Cui, D. Van Dam, S. A. Mann, N. J J Van Hoof, P. J. Van Veldhoven, E. C. Garnett, E. P A M Bakkers, and J. E M Haverkort. Boosting Solar Cell Photovoltage via Nanophotonic Engineering. *Nano Letters*, 16(10):6467–6471, 2016.
- [39] Avigail Landman, Hen Dotan, Gennady E. Shter, Michael Wullenkord, Anis Houaijia, Artjom Maljusch, Gideon S. Grader, and Avner Rothschild. Photoelectrochemical water splitting in separate oxygen and hydrogen cells. *Nature Materials*, (March):1–7, 2017.
- [40] I. Garcia, I. Rey-Stolle, C. Algora, W. Stolz, K. Volz, Stephanie Essig, Scott Ward, Myles A. Steiner, Daniel J. Friedman, John F. Geisz, Paul Stradins, David L. Young, Jieyang Jia, Linsey C. Seitz, Jesse D. Benck, Yijie Huo, Yusi Chen, Jia Wei Desmond Ng, Taner Bilir, James S. Harris, and Thomas F. Jaramillo. Solar water splitting by photovoltaic-electrolysis with a solar-to-hydrogen efficiency over 30%. *Energy Procedia*, 77(23):13237, 2016.
- [41] Jia Wang, Sebastien R Plissard, Marcel a Verheijen, Lou-Fe Feiner, Alessandro Cavalli, and Erik P a M Bakkers. Reversible switching of InP nanowire growth direction by catalyst engineering. *Nano letters*, 13(8):3802–6, aug 2013.
- [42] Yunyan Zhang, Ana M. Sanchez, Yue Sun, Jiang Wu, Martin Aagesen, Suguo Huo, Dongyoung Kim, Pamela Jurczak, Xiulai Xu, and Huiyun Liu. Influence of Droplet Size on the Growth of Self-Catalyzed Ternary GaAsP Nanowires. *Nano Letters*, 16(2):1237–1243, 2016.
- [43] Magnus T Borgström, George Immink, Bas Ketelaars, Rienk Algra, and Erik P a M Bakkers. Synergetic nanowire growth. *Nature nanotechnology*, 2(9):541–4, sep 2007.
- [44] Fumiya Ishizaka, Yoshihiro Hiraya, Katsuhiko Tomioka, Junichi Motohisa, and Takashi Fukui. Growth of All-Wurtzite InP/AlInP Core-Multishell Nanowire Array. *Nano Letters*, page acs.nanolett.6b03727, 2017.

- [45] Marta De Luca, Attilio Zilli, H. Aruni Fonseka, Sudha Mokkapati, Antonio Miriametro, Hark Hoe Tan, Leigh Morris Smith, Chennupati Jagadish, Mario Capizzi, and Antonio Polimeni. Polarized light absorption in wurtzite InP nanowire ensembles. *Nano Letters*, 15(2):998–1005, 2015.
- [46] Simone Assali, Johannes Greil, Ilaria Zardo, Abderrezak Belabbes, Michiel de Moor, S. Koelling, Paul M. Koenraad, Friedhelm Bechstedt, Erik P. A. M. Bakkers, and Jos E. M. Haverkort. Optical study of the band structure of wurtzite GaP nanowires. *Journal of Applied Physics*, 044304(120):0–10, 2016.
- [47] Peter Y. Yu and Manuel Cardona. *Fundamentals of Semiconductors*. Graduate Texts in Physics. Springer Berlin Heidelberg, Berlin, Heidelberg, 2010.
- [48] Attilio Zilli, Marta De Luca, Davide Tedeschi, H Aruni Fonseka, Antonio Miriametro, Hark Hoe Tan, Chennupati Jagadish, Mario Capizzi, and Antonio Polimeni. Temperature dependence of interband transitions in wurtzite InP nanowires. *ACS Nano*, 9(4):4277–4287, 2015.
- [49] Daniel Jacobsson, Federico Panciera, Jerry Tersoff, Mark C Reuter, Sebastian Lehmann, Stephan Hofmann, Kimberly A Dick, and Frances M Ross. Interface dynamics and crystal phase switching in GaAs nanowires. *Nature*, 531(7594):accepted, 2016.
- [50] Rienk E Algra, Vedran Vonk, Didier Wermeille, Wiesiek J Szweryn, Marcel a Verheijen, Willem J P van Enkevort, Arno a C Bode, Wim L Noorduyn, Erik Tancini, Aryan E F de Jong, Erik P a M Bakkers, and Elias Vlieg. Formation of wurtzite InP nanowires explained by liquid-ordering. *Nano letters*, 11(1):44–8, jan 2011.
- [51] Kun Li, Kar Wei Ng, Thai Truong D Tran, Hao Sun, Fanglu Lu, and Connie J. Chang-Hasnain. Wurtzite-Phased InP Micropillars Grown on Silicon with Low Surface Recombination Velocity. *Nano Letters*, 15(11):7189–7198, 2015.
- [52] G Signorello, E Lörtscher, P a Khomyakov, S Karg, D L Dheeraj, B Gotsmann, H Weman, and H Riel. Inducing a direct-to-pseudodirect bandgap transition in wurtzite GaAs nanowires with uniaxial stress. *Nature communications*, 5(7491):3655, jan 2014.
- [53] H??kon Ikaros T Hauge, Marcel A. Verheijen, Sonia Conesa-Boj, Tanja Etzelstorfer, Marc Watzinger, Dominik Kriegner, Ilaria Zardo, Claudia Fasolato, Francesco Capitani, Paolo Postorino, Sebastian K??lling, Ang Li, Simone Assali, Julian Stangl, and Erik P A M Bakkers. Hexagonal Silicon Realized. *Nano Letters*, 15(9):5855–5860, 2015.

- [54] Magnus T. Borgström, Jesper Wallentin, Kenichi Kawaguchi, Lars Samuelson, and Knut Deppert. Dynamics of extremely anisotropic etching of InP nanowires by HCl. *Chemical Physics Letters*, 502(4-6):222–224, 2011.
- [55] Fumiya Ishizaka, Yoshihiro Hiraya, Katsuhiko Tomioka, and Takashi Fukui. Growth of wurtzite GaP in InP/GaP core-shell nanowires by selective-area MOVPE. *Journal of Crystal Growth*, 411:71–75, 2015.
- [56] D Jacobsson, J M Persson, D Kriegner, T Etzelstorfer, J Wallentin, J B Wagner, J Stangl, L Samuelson, K Deppert, and M T Borgström. Particle-assisted Ga(x)In(1-x)P nanowire growth for designed bandgap structures. *Nanotechnology*, 23(24):245601, jun 2012.
- [57] John P. Perdew and Yue Wang. Accurate and simple analytic representation of the electron-gas correlation energy, 1992.
- [58] G Kresse and J Furthmüller. Efficient iterative schemes for ab initio total-energy calculations using a plane-wave basis set. *Physical review. B, Condensed matter*, 54(16):11169–11186, oct 1996.
- [59] Jian Rong Dong, Soo Jin Chua, Yan Jun Wang, and Hai Rong Yuan. Substrate orientation dependence of In composition of AlGaInP epilayers grown by MOCVD. *Journal of Crystal Growth*, 269(2-4):408–412, 2004.
- [60] Xin Yin and Xudong Wang. Kinetics-Driven Crystal Facets Evolution at the Tip of Nanowires: A New Implementation of the Ostwald-Lussac Law. *Nano Letters*, 16(11):7078–7084, 2016.
- [61] Kunal Mukherjee, Andrew G. Norman, Austin J. Akey, Tonio Buonassisi, and Eugene A. Fitzgerald. Spontaneous lateral phase separation of AlInP during thin film growth and its effect on luminescence. *Journal of Applied Physics*, 118(11), 2015.
- [62] I Pavesi, F Piazza, Institut De Micro, F Carlin, and M Ilegems. Temperature dependence of the InP band gap from a photoluminescence. *Phys. Rev. B*, 44(16):9052–9055, 1991.
- [63] T. Schmidt, K. Lischka, and W. Zulehner. Excitation-power dependence of the near-band-edge photoluminescence of semiconductors. *Physical Review B*, 45(16):8989–8994, 1992.
- [64] Kuranananda Pemasiri, Mohammad Montazeri, Richard Gass, Leigh M Smith, Howard E Jackson, Jan Yarrison-Rice, Suriati Paiman, Qiang Gao, H Hoe Tan, Chennupati Jagadish, Xin Zhang, and Jin Zou. Carrier dynamics and quantum confinement in type II ZB-WZ InP nanowire homostructures. *Nano Letters*, 9(2):648–654, 2009.

- [65] Y.P. Varshni. Temperature dependence of the energy gap in semiconductors. *Physica*, 34(1):149–154, 1967.
- [66] Yutao Fang, Lu Wang, Qingling Sun, Taiping Lu, Zhen Deng, Ziguang Ma, Yang Jiang, Haiqiang Jia, Wenxin Wang, Junming Zhou, and Hong Chen. Investigation of temperature-dependent photoluminescence in multi-quantum wells. *Scientific Reports*, 5(1):12718, 2015.
- [67] M. Boroditsky, I. Gontijo, M. Jackson, R. Vrijen, E. Yablonovitch, T. Krauss, Chuan-Cheng Cheng, A. Scherer, R. Bhat, and M. Krames. Surface recombination measurements on III-V candidate materials for nanostructure light-emitting diodes. *Journal of Applied Physics*, 87(7):3497, 2000.
- [68] R. J. Nelson, J. S. Williams, H. J. Leamy, B. Miller, H. C. Casey, B. A. Parkinson, and A. Heller. Reduction of GaAs surface recombination velocity by chemical treatment. *Applied Physics Letters*, 36(1):76–79, 1980.
- [69] H. H. Lee, R. J. Racicot, and S. H. Lee. Surface passivation of GaAs. *Applied Physics Letters*, 54(8):724–726, 1989.
- [70] C C Chang, C Y Chi, M Yao, N Huang, C C Chen, J Theiss, A W Bushmaker, S Lalumondiere, T W Yeh, M L Povinelli, C Zhou, P D Dapkus, and S B Cronin. Electrical and optical characterization of surface passivation in GaAs nanowires. *Nano Letters*, 12(9):4484–4489, 2012.
- [71] Makoto Kondo, Naoko Okada, Kay Domen, Katsumi Sugiura, Chikashi Anayama, and Toshiyuki Tanahashi. Origin of nonradiative recombination centers in AlGaInP grown by metalorganic vapor phase epitaxy. *Journal of Electronic Materials*, 23(3):355–358, 2013.
- [72] L. M. Smith, S. A. Rushworth, A. C. Jones, J. S. Roberts, A. Chew, and D. E. Sykes. Oxygen incorporation in aluminium-based semiconductors grown by metalorganic vapour phase epitaxy. *Journal of Crystal Growth*, 134(1-2):140–146, 1993.
- [73] D. Patel, J. M. Pikal, C. S. Menoni, K. J. Thomas, F. a. Kish, and M. R. Hueschen. Effect of indirect minima carrier population on the output characteristics of AlGaInP light-emitting diodes. *Applied Physics Letters*, 75(20):3201, 1999.
- [74] L. Gagliano, A. Belabbes, M. Albani, S. Assali, M. A. Verheijen, L. Miglio, F. Bechstedt, J. E. M. Haverkort, and E. P. A. M. Bakkers. Pseudodirect to Direct Compositional Crossover in Wurtzite GaP/In_xGa_{1-x}P Core-Shell Nanowires. *Nano Letters*, page acs.nanolett.6b04242, 2016.

- [75] Jinghua Zhao, Xiaohong Tang, Jinghua Teng, and Anna Marie Yong. Atomic ordering of AlInP grown by MOVPE using TBP with different V/III ratios in pure ambient N₂. *Journal of Crystal Growth*, 312(9):1505–1509, 2010.
- [76] Theresa M. Christian, Daniel A. Beaton, Kunal Mukherjee, Kirstin Alberi, Eugene A. Fitzgerald, and Angelo Mascarenhas. Amber-green light-emitting diodes using order-disorder Al_xIn_{1-x}P heterostructures. *Journal of Applied Physics*, 114(7):074505, 2013.
- [77] Kunal Mukherjee, Parag B. Deotare, and Eugene A. Fitzgerald. Improved photoluminescence characteristics of order-disorder AlGaInP quantum wells at room and elevated temperatures. *Applied Physics Letters*, 106(14), 2015.
- [78] Y. Calahorra, O. Shtempluck, V. Kotchetkov, and Y. E. Yaish. Young’s modulus, residual stress, and crystal orientation of doubly clamped silicon nanowire beams. *Nano Letters*, 15(5):2945–2950, 2015.
- [79] Johan Grönqvist, Niels Søndergaard, Fredrik Boxberg, Thomas Guhr, Sven Åberg, and H. Q. Xu. Strain in semiconductor core-shell nanowires. *Journal of Applied Physics*, 106(5), 2009.
- [80] Albert Davydov. Ultimate Bending Strength of Si Nanowires. (April), 2017.
- [81] Jesper Wallentin, Daniel Jacobsson, Markus Osterhoff, Magnus T. Borgström, and Tim Salditt. Bending and Twisting Lattice Tilt in Strained Core-Shell Nanowires Revealed by Nanofocused X-ray Diffraction. *Nano Letters*, page acs.nanolett.7b00918, 2017.
- [82] Samuel Hoffmann, Ivo Utke, Benedikt Moser, Johann Michler, Silke H Christiansen, Volker Schmidt, Stephan Senz, and Peter Werner. Measurement of the Bending Strength of Vapor - Liquid - Solid Grown Silicon Nanowires. (Figure 1):1–4, 2006.
- [83] C. Chen, M.C. Plante, C. Fradin, and R.R. LaPierre. Layer-by-layer and step-flow growth mechanisms in GaAsP/GaP nanowire heterostructures. *Journal of Materials Research*, 21(11):2801–2809, 2006.
- [84] Alexander Berg, Sebastian Lehmann, Neimantas Vainorius, Anders Gustafsson, Mats-Erik Pistol, L. Reine Wallenberg, Lars Samuelson, and Magnus T. Borgström. Growth and characterization of wurtzite GaP nanowires with control over axial and radial growth by use of HCl in-situ etching. *Journal of Crystal Growth*, 386:47–51, jan 2014.

- [85] Alexander Berg, Kilian Mergenthaler, Martin Ek, Mats-Erik Pistol, L Reine Wallenberg, and Magnus T Borgström. In situ etching for control over axial and radial III-V nanowire growth rates using HBr. *Nanotechnology*, 25(50):505601, 2014.
- [86] Dominik Kriegner, Simone Assali, Abderrezak Belabbes, Tanja Etzelstorfer, Václav Holý, Tobias Schüllli, Friedhelm Bechstedt, Erik P A M Bakkers, Günther Bauer, and Julian Stangl. Unit cell structure of the wurtzite phase of GaP nanowires: X-ray diffraction studies and density functional theory calculations. *Physical Review B - Condensed Matter and Materials Physics*, 88(11):1–7, 2013.
- [87] D Kriegner, E Wintersberger, K Kawaguchi, J Wallentin, M T Borgström, and J Stangl. Unit cell parameters of wurtzite InP nanowires determined by x-ray diffraction. *Nanotechnology*, 22(42):425704, oct 2011.
- [88] A. R. Denton and N. W. Ashcroft. Vegards law. *Physical Review A*, 43(6):3161–3164, 1991.
- [89] S. Q. Wang and H. Q. Ye. First-principles study on elastic properties and phase stability of III - V compounds. *Physica Status Solidi (B) Basic Research*, 240(1):45–54, 2003.
- [90] Fredrik Boxberg, Niels Sondergaard, and H. Q. Xu. Elastic and piezoelectric properties of zincblende and wurtzite crystalline nanowire heterostructures. *Advanced Materials*, 24(34):4692–4706, 2012.
- [91] Fabian Schuster, Jonas Kapraun, Gilliard N Malheiros, Saniya Deshpande, and Connie J Chang-hasnain. Site-Controlled Growth of Monolithic In-GaAs / InP Quantum Well Nanopillar Lasers on Silicon. 2017.
- [92] Lisa S Karlsson, Magnus W Larsson, Mats-erik Pistol, Werner Seifert, and Johanna Tra. Growth and Optical Properties of Strained GaAs - Ga x In 1 - x P Core - Shell Nanowires. pages 1–5, 2005.
- [93] P. Krogstrup, N. L. B. Ziino, W. Chang, S. M. Albrecht, M. H. Madsen, E. Johnson, J. Nygård, C. M. Marcus, and T. S. Jespersen. Epitaxy of semiconductor-superconductor nanowires. *Nature Materials*, 14(4):400–406, 2015.
- [94] M. Taupin, E. Mannila, P. Krogstrup, V. F. Maisi, H. Nguyen, S. M. Albrecht, J. Nygård, C. M. Marcus, and J. P. Pekola. InAs Nanowire with Epitaxial Aluminum as a Single-Electron Transistor with Fixed Tunnel Barriers. *Physical Review Applied*, 6(5), 2016.

- [95] Marijn A M Versteegh, Michael E Reimer, Klaus D Jöns, Dan Dalacu, Philip J Poole, Angelo Gulinatti, Andrea Giudice, and Val Zwiller. Observation of strongly entangled photon pairs from a nanowire quantum dot. *Nature Communications*, 5:5298, 2014.
- [96] Gediminas Juska, Valeria Dimastrodonato, Lorenzo O. Mereni, Agnieszka Gocalinska, and Emanuele Pelucchi. Towards quantum-dot arrays of entangled photon emitters. *Nature Photonics*, 7(7):527–531, 2013.
- [97] Neimantas Vainorius, Sebastian Lehmann, Daniel Jacobsson, Lars Samuelson, Kimberly A. Dick, and Mats Erik Pistol. Confinement in Thickness-Controlled GaAs Polytype Nanodots. *Nano Letters*, 15(4):2652–2656, 2015.
- [98] N Akopian, G Patriarche, L Liu, J-C Harmand, and V Zwiller. Crystal phase quantum dots. *Nano letters*, 10(4):1198–201, apr 2010.
- [99] Jonas Lähnemann, Oliver Brandt, Uwe Jahn, Carsten Pfüller, Claudia Roder, Pinar Dogan, Frank Grosse, Abderrezak Belabbes, Friedhelm Bechstedt, Achim Trampert, and Lutz Geelhaar. Direct experimental determination of the spontaneous polarization of GaN. *Physical Review B*, 86(8):081302, aug 2012.
- [100] Rienk E Algra, Moïra Hocevar, Marcel a Verheijen, Ilaria Zardo, George G W Immink, Willem J P van Enckevort, Gerhard Abstreiter, Leo P Kouwenhoven, Elias Vlieg, and Erik P a M Bakkers. Crystal structure transfer in core/shell nanowires. *Nano letters*, 11(4):1690–4, apr 2011.
- [101] L. Geelhaar S. Breuer, L.-F. Feiner, A. Trampert. *Book of Abstracts 6th Nanowire Growth Workshop*. St. Petersburg, Russia, 2012 edition, 2012.
- [102] Katsuhiko Tomioka, Masatoshi Yoshimura, and Takashi Fukui. A III-V nanowire channel on silicon for high-performance vertical transistors. *Nature*, 488(7410):189–92, aug 2012.
- [103] Frank Glas. Chemical potentials for Au-assisted vapor-liquid-solid growth of III-V nanowires. *Journal of Applied Physics*, 108(7), 2010.
- [104] Oleksiy Roslyak and Andrei Piryatinski. Thermoelectric properties of semiconductor nanowire networks. *Journal of Applied Physics*, 119(12), 2016.
- [105] Akram I. Boukai, Yuri Bunimovich, Jamil Tahir-Kheli, Jen-Kan Yu, William A. Goddard III, and James R. Heath. Silicon nanowires as efficient thermoelectric materials. *Nature*, 451(7175):168–171, 2008.

- [106] Gang Meng, Fuwei Zhuge, Kazuki Nagashima, Atsuo Nakao, Masaki Kanai, Yong He, Mickael Boudot, Tsunaki Takahashi, Ken Uchida, and Takeshi Yanagida. Nanoscale Thermal Management of Single SnO₂ Nanowire: pico-Joule Energy Consumed Molecule Sensor. *ACS Sensors*, 1(8):997–1002, 2016.
- [107] Po-Chun Hsu, Xiaoge Liu, Chong Liu, Xing Xie, Hye Ryoung Lee, Alex J Welch, Tom Zhao, and Yi Cui. Personal Thermal Management by Metallic Nanowire-Coated Textile. 2015.
- [108] Roman Anufriev, Aymeric Ramiere, Jeremie Maire, and Masahiro Nomura. Heat guiding and focusing using ballistic phonon transport in phononic nanostructures. *Nature Communications*, 8(May):1–19, 2016.
- [109] Jaeho Lee, Jongwoo Lim, and Peidong Yang. Ballistic phonon transport in holey silicon. *Nano Letters*, 15(5):3273–3279, 2015.
- [110] Martin Ek, B. Mattias Borg, Jonas Johansson, and Kimberly A. Dick. Diameter limitation in growth of III-Sb-containing nanowire heterostructures. *ACS Nano*, 7(4):3668–3675, 2013.
- [111] V. G. Dubrovskii, N. V. Sibirev, G. E. Cirlin, I. P. Soshnikov, W. H. Chen, R. Larde, E. Cadel, P. Pareige, T. Xu, B. Grandidier, J. P. Nys, D. Stievenard, M. Moewe, L. C. Chuang, and C. Chang-Hasnain. Gibbs-Thomson and diffusion-induced contributions to the growth rate of Si, InP, and GaAs nanowires. *Physical Review B - Condensed Matter and Materials Physics*, 79(20):1–7, 2009.
- [112] P. Kim, L. Shi, A. Majumdar, and P. L. McEuen. Thermal transport measurements of individual multiwalled nanotubes. pages 19–22, 2001.
- [113] R.B. Dingle. The electrical conductivity of thin wires. *Proceedings of the Royal Society A: Mathematical, Physical and Engineering Sciences*, 201:545–560, 1950.
- [114] R. Dimmich and F. Warkusz. Electrical Conductivity of Thin Wires. *Active and Passive Electronic Components*, 12(2):103–109, 1986.
- [115] M Y Swinkels, M R van Delft, D S Oliveira, A Cavalli, I Zardo, R W van der Heijden, and E P A M Bakkers. Diameter dependence of the thermal conductivity of InAs nanowires. *Nanotechnology*, 26(38):385401, 2015.
- [116] Xavier Cartoixa, Luciano Colombo, and Riccardo Rurali. Thermal Rectification by Design in Telescopic Si Nanowires. *Nano Letters*, 15(12):8255–8259, 2015.

- [117] Joseph D Christesen, Christopher W Pinion, Erik M Grumstrup, John Michael Papanikolas, and James F Cahoon. Synthetically Encoding 10-nm Morphology in Silicon Nanowires. *Nano letters*, 13(12):6281–6286, 2013.
- [118] G. Priante, S. Ambrosini, V. G. Dubrovskii, A. Franciosi, and S. Rubini. Stopping and resuming at will the growth of GaAs nanowires. *Crystal Growth and Design*, 13(9):3976–3984, 2013.
- [119] Samuel Crawford, Sung Keun Lim, and Silvija Gradecak. Fundamental insights into nanowire diameter modulation and the liquid / solid interface. *Nano Letters*, 13(1):226–232, 2012.
- [120] Jia Wang, S??bastien R. Plissard, Marcel A. Verheijen, Lou F?? Feiner, Alessandro Cavalli, and Erik P A M Bakkers. Reversible switching of InP nanowire growth direction by catalyst engineering. *Nano Letters*, 13(8):3802–3806, 2013.
- [121] Philips Lighting. Philips Lighting reports improvement in comparable sales growth, continued increase in profitability and free cash flow. 2017.
- [122] Philip Smallwood. Lighting , LEDs and smart lighting market overview. *DOE SSL R&D Workshop*, 2016.
- [123] María Laura T Cossio, Laura F Giesen, Gabriela Araya, María Luisa S Pérez-Cotapos, RICARDO LÓPEZ VERGARA, Maura Manca, R. A. Tohme, S. D. Holmberg, Tim Bressmann, Daniel Rodrigues Lirio, Jelitza Soto Román, Rodrigo Ganter Solís, Sanjay Thakur, SVD Nageswara Rao, E L Modelado, Artificial D E La, Cabeza Durante, U N A Tradición, Maya En, E L Espejo, D E L A S Fuentes, Universidad Autónoma De Yucatán, Cruz Moreno Lenin, Laura Franco Cian, M Joanne Douglas, La Plata, and Françoise Héritier. Lighting the way: Perspectives on the global lighting market. *Mc Kinsey & Company*, 2011.
- [124] Danish Energy Agency and Energy Piano. European LED Market Evolution and Policy Impacts. Technical Report 244, 2015.
- [125] M.J. Schmidt. *Business case essentials: a guide to structure and content*. Number April. 2003.
- [126] G. G. Untila, T. N. Kost, and A. B. Chebotareva. Multi-wire metallization for solar cells: Contact resistivity of the interface between the wires and In₂O₃:Sn, In₂O₃:F, and ZnO:Al layers. *Solar Energy*, 142:330–339, 2017.

- [127] Jinsu Yoo, Jeonghul Lee, Seokki Kim, Kyunghoon Yoon, I. Jun Park, S. K. Dhungel, B. Karunagaran, D. Mangalaraj, and Junsin Yi. High transmittance and low resistive ZnO:Al films for thin film solar cells. *Thin Solid Films*, 480-481:213–217, 2005.

Summary

Semiconductor materials play a key role in technologies such as solid state lighting, photovoltaics and solar fuels production due to their unique properties, first of all the presence of an energy gap in their electronic structure. Conventional band gap engineering is performed by changing their chemical composition, but such approach sometimes encounters severe limitations such as alloy miscibility, strain at heterointerfaces and in general intrinsic limits which cannot be overcome with known methods. Recently, a new degree of freedom in band gap engineering has been unlocked. By changing the crystal symmetry of a semiconductor, one can induce a change in its electronic properties. For example, gallium phosphide (GaP) is a known indirect semiconductor in the zincblende (ZB, cubic) symmetry, but its band gap becomes direct in the wurtzite (WZ, hexagonal) symmetry. However, the resulting selection rules make WZ GaP a pseudo-direct semiconductor, where the band gap is direct, and the main optical transition is forbidden. In order to obtain light emission, alloying is necessary.

In this thesis, we explored new materials for efficient light emitting diodes (LEDs) by developing novel hexagonal III-phosphide alloys. Such materials were grown in the form of nanowires with metalorganic vapor phase epitaxy (MOVPE) growth, both using gold catalyst assisted vapor-liquid-solid (VLS) and selective area epitaxy (SAE) techniques.

We realized WZ GaP/ $\text{In}_x\text{Ga}_{1-x}\text{P}$ core-shell nanowires with tunable composition in the range $0 < x < 0.75$ and we investigated their optical properties with photoluminescence (PL). Band gap tunability was achieved between 750nm (1.6eV) and 590nm (2.1eV). By studying the time and temperature dependency of the PL, a pseudo-direct to direct band gap crossover was identified, thus defining the limits of application of WZ $\text{In}_x\text{Ga}_{1-x}\text{P}$ as emitting material in LEDs.

We developed WZ $\text{Al}_x\text{In}_{1-x}\text{P}$ nanowires with tunable composition, using selective area epitaxy. These nanowires were found to provide tunable emission between 875nm (1.42eV) and 550nm (2.25eV) in the green region and constitute a possible candidate for future practical application in LEDs.

We studied the structure of WZ GaP/ $\text{In}_x\text{Ga}_{1-x}\text{P}$ core-shell nanowires, which

were found to be inhomogeneous and affected by strain due to lattice mismatch. We performed an in-depth analysis of both crystal structure and composition of the nanowires, using transmission electron microscopy (TEM) and finite element method simulations (FEM). This work provided with improved understanding of lattice-mismatched heterostructured core-shell nanowires by providing direct insight in their growth mechanism and structural properties.

Alloying is not the only method to achieve band gap engineering: crystal symmetry control in nanowires allows the realization of atomically sharp homostructures which can in the future be used for the emission of single entangled photons. We developed WZ/ZB crystal phase homointerface, approaching the monolayer control and improving the understanding in crystal phase switching in VLS-grown nanowires by controlling the growth of both phases.

We developed thin WZ GaP nanowires, down to 25nm in diameter and show their quasi-ballistic phonon transport at room temperature. We also develop telescopic nanowires, with controllable variable diameter for future use as thermal rectifier. In the final chapter we discuss the practical application of WZ $\text{Al}_x\text{In}_{1-x}\text{P}$ for solid state lighting and illustrate a possible business plan for the employment of nanowires in current light emitting diodes technology.

Curriculum Vitae

Luca Gagliano was born on 28-07-1987 in Milano, Italy. After finishing Scientific High School G. Marconi in Milano, in 2006, he studied Materials Science at Università di Milano-Bicocca. In 2013 he graduated cum Laude, obtaining the Master Degree in Materials Science, supervised by Dr. E. Bonera in the group of Prof. M. Guzzi, with a thesis on Raman spectroscopy of SiGe nanostructures. He won the Cerofolini Prize of his faculty for being one of the two best students. In 2011 he worked at the European Space Agency for 6 months on a research internship, studying the X-ray absorption properties of the interstellar medium. In 2013 he started a PhD project at TU/e in Eindhoven, Netherlands, the results of which are presented in this dissertation. In 2017 he attended the executive training course New Business Development at the Rotterdam School of Management, Erasmus University. In September 2017 he became Postdoctoral Researcher at TU/e in Eindhoven.

List of Publications

- Pseudodirect to direct compositional crossover in Wurtzite GaP/ $\text{In}_x\text{Ga}_{1-x}$ P core-shell nanowires - L. Gagliano, A. Belabbes, M. Albani, S. Assali, M.A. Verheijen, L. Miglio, F. Bechstedt, J.E.M. Haverkort, E.P.A.M. Bakkers - Nano Lett. (2016)
- US Patent (2016): "Nano-light source emitting polarized light" - L. Gagliano, D. deBoer, H. Cornelissen, J.E.M. Haverkort, E.P.A.M. Bakkers
- Infrared to green emitting pure Wurtzite $\text{Al}_x\text{In}_{1-x}$ P nanowires - L. Gagliano, A. Belabbes, M.A. Verheijen, F. Bechstedt, J.E.M. Haverkort, E.P.A.M. Bakkers - In preparation
- Understanding the origin of bending in heterostructured core-shell nanowires - L. Gagliano, M. Albani, M. A. Verheijen, L. Miglio, E.P.A.M. Bakkers - In preparation
- Growth and optical properties of direct band gap Ge/ $\text{Ge}_{0.87}\text{Sn}_{0.13}$ core/shell nanowire arrays - S. Assali, A. Dijkstra, A. Li, S. Koelling, M.A. Verheijen, L. Gagliano, N. von den Driesch, D. Buca, P.M. Koenraad, J.E.M. Haverkort, E.P.A.M. Bakkers - Nano Lett. (2017)
- Anisotropic extended misfit dislocations in overcritical SiGe films by local substrate patterning - M. Bollani, D. Chrastina, R. Ruggeri, G. Nicotra, L. Gagliano, E. Bonera, V. Mondiali, A. Marzegalli, F. Montalenti, C. Spinella and L. Miglio - Nanotechnology (2016)
- Exploring crystal phase switching in GaP nanowires - S. Assali, L. Gagliano, D. S. Oliveira, M. A. Verheijen, S. R. Plissard, L. F. Feiner and E. P. A. M. Bakkers - Nano Lett. (2015)
- Local uniaxial tensile strain in germanium up to 4% by epitaxial nanostructures - M. Bollani, D. Chrastina, L. Gagliano, L. Rossetto, D. Scopece,

- M. Barget, V. Mondiali, J. Frigerio, M. Lodari, F. Pezzoli, F. Montalenti and E. Bonera - *Appl. Phys. Lett.* (2015)
- Strain release management in SiGe/Si films by substrate patterning - V. Mondiali, M. Bollani, D. Chrastina, R. Rubert, G. Chahine, M. I. Richard, S. Cecchi, L. Gagliano, E. Bonera, T. Schulli, and L. Miglio - *Appl. Phys. Lett.* (2014)
 - Lithographically-defined low dimensional SiGe nanostripes as silicon stressors - M. Bollani, D. Chrastina, M. Fiocco, V. Mondiali, J. Frigerio, L. Gagliano, and E. Bonera - *J. Appl. Phys.* (2012)

